Review

Catalyst Design for Photocatalytic CO_2 Reduction: Recent Advances, Challenges, and Future Perspectives

Wandercleiton Cardoso , Simge Naz Degerli , Somayeh Taghavi , Federica Menegazzo , Michela Signoretto , Gianguido Ramis , Ilenia Rossetti *

Posted Date: 22 April 2026

doi: 10.20944/preprints202604.1590.v1

Keywords: photoreduction of CO_2; artificial photosynthesis; titania; graphitic carbon nitride; heterojunctions; S-scheme photocatalysts; Z-scheme photocatalysts

 doi:10.20944/preprints202604.1590.v1

Review

Catalyst Design for Photocatalytic CO_2 Reduction: Recent Advances, Challenges, and Future Perspectives

Wandercleiton Cardoso [1], Simge Naz Degerli [2], Somayeh Taghavi [2,3,4], Federica Menegazzo [2,4], Michela Signoretto [2,4], Gianguido Ramis [2,5] and Ilenia Rossetti [1,2,*]

[1] Chemical Plants and Industrial Chemistry Group, Department of Chemistry, University of Milan and CNR-SCITEC, Via Camillo Golgi 19, CAP 20133, Milan, Italy

[2] INSTM: National Interuniversity Consortium for Materials Science and Technology, Via Giuseppe Giusti 9, 50121 Florence, Italy

[3] Department of Applied Chemistry, Faculty of Chemistry, University of Mazandaran, Babolsar, 47416-95447, Iran

[4] CATMAT Laboratory, Department of Molecular Sciences and Nanosystems, Ca' Foscari University of Venice, Via Torino 155, CAP 30172, Venezia Mestre, Italy

[5] Department of Chemical, Civil and Environmental Engineering, University of Genoa, Via all'Opera Pia 15A, CAP 16145, Genoa, Italy

* Correspondence: ilenia.rossetti@unimi.it

Abstract

The photoreduction of CO_2 is a growingly interesting research topic due to the intriguing possibility of producing solar fuels through a concerning pollutant. TiO_2 photocatalysts were the first materials used for this application, but since then, various strategies have been developed to optimise the catalytic performance and operating conditions to obtain competitive yield. This review presents the findings of the last decade of research on different semiconductors, TiO_2 and g-C_3N_4 and their composites. The main features of the reaction and its key issues are first overviewed, focusing on the effect of different reaction conditions on the performance and recalling the mechanism of the reaction. The strategies developed to overcome the challenges of this demanding reaction are described in the following paragraphs, including the use of dopants or co-catalysts, of heterojunctions between different semiconductors and the use of electron transfer mediators. Finally, some unifying concepts are summarised, suggesting the calculation of the stored energy amount and the relative efficiency to allow a safer comparison between literature data collected under widely variable conditions and leading to different products.

Keywords: photoreduction of CO_2; artificial photosynthesis; titania; graphitic carbon nitride; heterojunctions; S-scheme photocatalysts; Z-scheme photocatalysts

1. Introduction

The global energy crisis and air pollution have worsened due to population growth, higher living standards, increased fuel consumption, and rapid industrialisation. Consequently, carbon dioxide (CO_2) emissions have risen significantly in recent decades, reaching approximately 37 Gt in 2023 compared with about 22 Gt in 1990. Projections indicate that global energy demand may increase by mid-century. CO_2 is the most abundant anthropogenic greenhouse gas in the atmosphere, with around 65% originating from direct human activities such as fuel combustion and industrial processes, and an additional share associated with land-use changes and forestry[1-6].

In December 2015, 195 nations signed a historic agreement in Paris to limit climate change and move towards a low-carbon, resilient, and sustainable future. The agreement aims to keep the global

 doi:10.20944/preprints202604.1590.v1

temperature increase well below 2 °C this century and to pursue efforts to limit it to 1.5 °C above pre-industrial levels[1, 6, 7].

Global average temperatures rose by approximately 0.6 °C during the 20th century, with a clear acceleration in recent decades. The continued increase in CO_2 emissions from fossil fuel combustion has raised concerns about climate change, prompting a global shift towards greater reliance on renewable energy sources to meet current and future energy demands[1, 6, 7].

Solar energy is the most prevalent renewable energy resource, but its main limitation is its intermittency and lack of full stability due to atmospheric interference. Therefore, energy storage solutions must be implemented to ensure a continuous supply, which increases the cost and complexity of the technologies developed. Considerable attention is given to the production of regenerated fuels from CO_2, an endoergic process regardless of the reduced product. The advantage of coupling these two concepts is clear: using CO_2 reduction to chemicals as a means of energy storage for solar power[8-13].

Photocatalytic production of fuels from CO_2 is a technology currently at the early demonstration stage at laboratory scale, with strong potential for emissions mitigation and future energy security. Various semiconductor materials have been used as photocatalysts in the CO_2 photoreduction process, including TiO_2, Cu_2O, ZnO, ZnS, CdTe, CdS, CdSe, WO_3, $BiWO_6$ and, more recently, g-C_3N_4 [14-19]. The attention has been recently focused also on photoreactors design[20-24].

Despite the considerable potential of this reaction, many issues remain regarding the sensitivity of materials to visible light, as well as their stability, productivity and selectivity. Scale-up and reproducibility should also be considered. Therefore, in this review, we summarise recent progress in the photoreduction of CO_2, with particular emphasis on the development of materials.

Accordingly, the work begins with an introductory overview of the main features of the reaction and its remaining unsolved issues, followed by a classification of the main material groups most frequently discussed in the literature. The survey includes discoveries from the last decade, except for a few earlier fundamental studies.

2. Photoreduction of CO2, Main Features and Open Challenges

Photocatalytic CO_2 reduction aims to convert the products of hydrocarbon combustion, namely water and carbon dioxide, back into energy carriers, regenerating fuels through a process often referred to as artificial photosynthesis. Photocatalytic CO_2 conversion uses solid semiconductors that serve two main functions: acting as catalysts to accelerate reactions under light irradiation and providing the energy required to drive a thermodynamically endergonic process[16, 25].

As shown in Figure 1, the overall mechanism consists of three main steps. First, the semiconductor absorbs photons with sufficient energy, generating charge carriers as electron–hole pairs. Next, these charge carriers are separated and transported through the structure of the photocatalytic material. Finally, electrons and holes participate in redox reactions with species adsorbed on the catalyst surface, in particular promoting the conversion of CO_2[15].

Photocatalytic CO_2 conversion involves photophysical and photochemical processes initiated by the absorption of photons with energy equal to or greater than the band gap of the semiconductor. This photoexcitation promotes electrons from the valence band (VB) to the conduction band (CB), generating electron (e^-)–hole (h^+) pairs[15].

After photoexcitation, the charge carriers migrate through the material, as shown in Figure 2. The photocatalytic process involves the following steps: (a) light harvesting, corresponding to the absorption of light by the semiconductor with energy higher than the semiconductor band gap; (b) charge excitation, which generates electron–hole pairs; and (c) charge separation and transfer, involving the separation and transport of these charge carriers[8, 14, 19].

During this process, (d) bulk charge recombination may occur within the semiconductor, or (e) surface charge recombination may take place at the material surface. When recombination is minimised, charge carriers reach the catalyst surface and participate in redox reactions with adsorbed

 doi:10.20944/preprints202604.1590.v1

species, resulting in (f) surface reduction reactions driven by electrons and (g) surface oxidation reactions driven by holes[8, 14, 19].

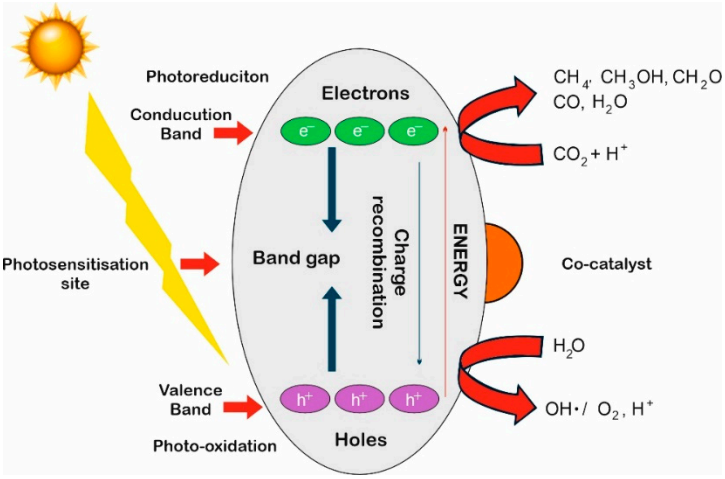

Figure 1. Illustration of photocatalytic CO_2 reduction over a semiconductor photocatalyst. Readapted from[15].

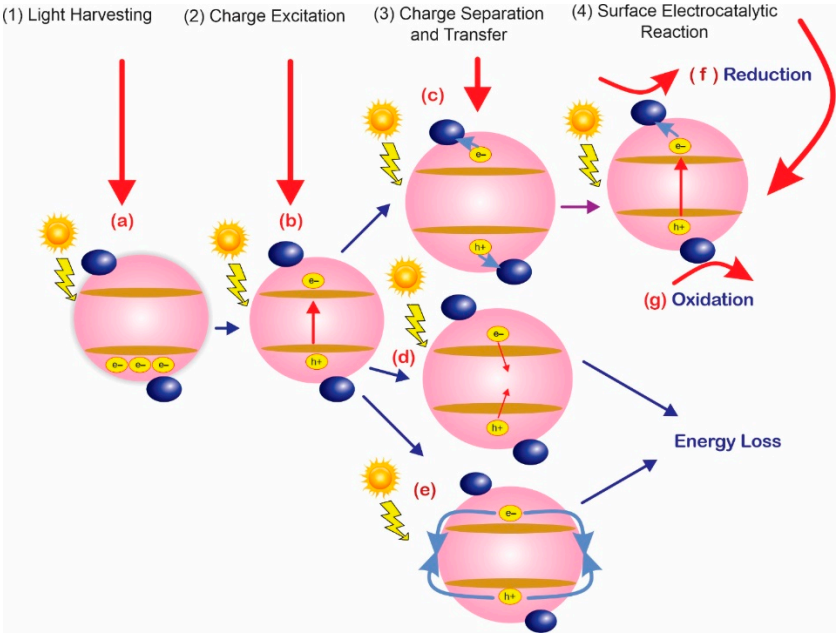

Figure 2. Fundamental principles of photocatalysis. Readapted from[26].

In this context, not every electron reaching the catalyst surface can reduce CO_2, a thermodynamically stable and chemically inert molecule[26, 27]. Unlike most conventional reduction methods, which typically require high energy input such as elevated temperature or pressure, photocatalytic processes rely primarily on solar irradiation as the energy source[18, 28]. Photogenerated electrons with sufficiently negative reduction potentials provide the driving force for the desired chemical reactions, although an additional kinetic overpotential is often required[29].

The reduction potential indicates the tendency of a chemical species to accept electrons. This parameter determines whether a species will be reduced by gaining electrons or oxidised by losing them. Species with more positive reduction potentials exhibit a greater affinity for electrons. Therefore, to reduce CO_2 to carbon monoxide or hydrocarbons, electrons in the semiconductor must have a sufficiently negative potential. Conversely, for water oxidation, the holes must have a more positive potential[29]. At pH 7, Table 1 [29, 30] presents the reaction pathways for the formation of some of the most relevant solar fuels, along with their corresponding reduction potentials.

 doi:10.20944/preprints202604.1590.v1

Table 1. Standard Reduction Potentials for CO_2 Electrochemical Conversion [30].

Reaction	E° (V, pH=7)
$CO_2 + e^- \rightarrow \bullet CO_2^-$	-1.90
$CO_2 + 2H^+ + 2e^- \rightarrow HCOOH$	-0.61
$CO_2 + 2H^+ + 2e^- \rightarrow CO + H_2O$	-0.53
$CO_2 + 4H^+ + 4e^- \rightarrow HCHO + H_2O$	-0.48
$CO_2 + 6H^+ + 6e^- \rightarrow CH_3OH + H_2O$	-0.38
$CO_2 + 8H^+ + 8e^- \rightarrow CH_4 + 2H_2O$	-0.24
$2H_2O + 4h^+ \rightarrow O_2 + 4H^+$	+0.81
$2H^+ + 2e^- \rightarrow H_2$	-0.42

Methane and methanol synthesis are more attractive for CO_2 reduction from a thermodynamic perspective, as these reactions occur at lower potentials and produce compounds with much higher calorific value as fuels. In other words, driving these reactions enables the storage of a greater amount of solar energy. However, kinetic limitations make the production of methane and methanol more challenging than that of carbon monoxide, formaldehyde, and formic acid, because the former reactions require more electrons to be supplied simultaneously, which implies a low sticking coefficient[30].

The interaction between the photocatalyst and adsorbed species may involve a series of one-electron processes rather than a multi-electron step, due to the complex nature of the inorganic photocatalyst surface. Therefore, the reaction pathway determines the actual redox potential required. For example, the potential is approximately 1.9 V vs NHE if CO_2 reduction begins with the single-electron reduction of CO_2 to $CO_2^{\bullet-}$. With this in mind, it is essential to increase reaction efficiency by enabling the simultaneous transfer of multiple electrons with protons. Consequently, generating sufficient electron-hole pairs, efficiently separating charges, and providing effective catalytic active sites are the most important factors for CO_2 photoreduction[31-33].

Despite the high potential of this reaction, one of the main challenges is the low conversion efficiency, especially under solar irradiation, which may be explained by these issues.

- A mismatch between the semiconductor's absorption capacity and the solar spectrum limits solar light harvesting[29, 31].
- Poor charge carrier separation efficiency: recombination events usually occur much faster than reactive events; therefore, physical separation of the photogenerated charges is necessary.
- A low solubility of CO_2 molecules in water (approximately 33 mmol in 1 L of water at 100 kPa and ambient temperature)[34].
- Reversible reactions that compete with CO_2 reduction can oxidatively decompose the photoreduction products back to CO_2. As holes are responsible for the oxidation half-reactions, suitable hole scavengers must be provided that do not interfere with the main reaction[35].
- The competing reaction of water reduction to hydrogen[27].

Almost 5% of the solar spectrum is ultraviolet radiation, while 43% of solar energy lies within the visible light spectrum. Therefore, identifying a photocatalyst that can absorb visible light and still possess a suitable conduction band potential is a key objective. As charge carrier movement and reactions require an overpotential as a driving force, the actual energy required for CO_2 conversion is typically higher than the theoretical energy needed to thermodynamically synthesise the desired products[18].

Although it is difficult to directly match the band gap of a semiconductor to the solar spectrum, several techniques have been employed to increase the capacity of inorganic photocatalysts to absorb the visible part of the spectrum. For example, to make photocatalysts with a broad band gap more sensitive to visible light absorption, doping with hetero-elements has been pursued, using metal ions (Fe^{3+}, Zn^{2+}, W^{6+}) and non-metal ions (C, N, S, B). This strategy is commonly adopted to produce visible-sensitive catalysts based on TiO_2, which has a band gap of approximately 3.2 eV and therefore natively absorbs only UV light[36-40].

 doi:10.20944/preprints202604.1590.v1

Doping introduces defect states (inter-band states or mid-gap levels) that enable electrons to be promoted with lower energy uptake, thereby improving visible light sensitivity. In addition, this may inhibit charge recombination. For example, it was shown that mixing the p states of the dopants with the O 2p states of the semiconductor produces a new valence band state, which is responsible for the reduced band gap of the semiconductor after doping with non-metal ions (such as N or C)[41].

Another effective method to enhance light absorption and charge separation is the formation of semiconductor heterostructures. Band bending creates a built-in field due to band alignment, causing photogenerated electrons and holes to move in opposite directions, thereby improving charge separation[42-46].

As an alternative, semiconductor quantum dots (QDs) can be considered an ideal option for the coupled component in heterostructures. When QDs are present, the visible light response of the photocatalysts is easily adjustable. QDs can also use hot electrons to generate multiple charge carriers when excited by a single high-energy photon, resulting in an increased number of charge carriers[47].

Similarly, organic dyes are often used as sensitisers to enhance a semiconductor's ability to absorb visible light. Dye molecules can inject photoexcited electrons into the semiconductor's conduction band when exposed to radiation. Under irradiation, dyes can transfer photoexcited electrons to the conduction band of the semiconductor. However, many factors affect the efficiency of electron transfer between the dye sensitiser and the semiconductor, such as the alignment of the Lowest Unoccupied Molecular Orbital (LUMO) level of the dye with the conduction band edge of the semiconductor. The stability of the organic sensitiser is also a critical consideration for practical applications[48, 49].

Utilisation of an equivalent amount of photogenerated holes should be considered when CO_2 is reduced by photogenerated electrons. Otherwise, accumulation of holes in the photocatalyst increases the likelihood of charge recombination and reduces electron lifetime. Additionally, if holes are not utilised effectively, they may negatively affect the photocatalytic reaction, such as causing photocorrosion of the photocatalyst. The most common solution is to use an artificial electron donor to scavenge the holes (hole scavenger, HS)[35, 50-54].

However, the process and energy required to synthesise the artificial electron donor should also be considered to assess the overall sustainability of the process (economic, energetic, environmental). Water is considered an ideal electron donor, but its high oxidation potential is the main disadvantage. Additionally, oxygen evolution requires a four-electron transfer, making this step kinetically limiting. Only a few photocatalysts can reduce CO_2 and simultaneously oxidise water[52, 53, 55, 56].

When water is used as an electron donor, competition from the water reduction process initiated by photogenerated electrons can also occur. Compared to most CO_2 reduction pathways, water reduction is a more facile process from both kinetic and thermodynamic perspectives. Thermodynamically, the reduction potential of water is 0.0 eV (at pH 0), which is more positive than that of CO_2 reduction to CO, formic acid, or formaldehyde. Kinetically, water reduction requires two electrons, making it faster than most CO_2 reduction reactions, which require two to eight electrons. However, CO_2 reduction is further limited by its low solubility in water, whereas water reduction does not face this issue. In fact, water is the most abundant reactant in the photoreactor when operating in the aqueous phase. This problem could be addressed by controlling reaction selectivity: modifying the morphology of the photocatalyst, altering the exposed facets, and introducing new reaction sites or selective co-catalysts. To achieve this, it is believed that a specific atomic arrangement to facilitate the adsorption of CO_2 molecules rather than water molecules on the surface[30, 57, 58].

3. Factors Influencing Photocatalytic Activity

3.1. Pressure and temperature

The low solubility of CO_2 in water is one of the factors limiting CO_2 photoreduction in the liquid phase. To address this issue, a pressurised photoreactor capable of operating up to 20 bar was designed. Both liquid-phase products (formic acid, formaldehyde) and gas-phase products (H_2, CO,

 doi:10.20944/preprints202604.1590.v1

CH_4) were successfully produced under various reaction conditions. The complex spectrum of compounds generated by these reactions cannot be easily described. It is predicted that organic compounds formed in the liquid phase during the initial hours on stream would undergo photoreforming, leading to also to H_2 production .

The low solubility of CO_2 in water (0.033 M at 25 °C, 1 atm CO_2), particularly at higher temperatures that could enhance reaction kinetics, has consistently resulted in extremely low productivity. Tests with various solvents, such as acetonitrile or methanol (CO_2 solubility 0.2 M and 0.3 M, respectively), increased the CO_2 concentration in the liquid phase but did not offer a practically viable solution. In addition, no substantial increase in CO_2 conversion was observed compared to using pure water as the solvent[20, 23, 34, 59-66].

The solubility of CO_2 in water increases significantly with rising pressure. Additionally, increasing the temperature can cause a notable rise in activity, which is likely to accelerate the dark phases of the reaction. However, as temperature increases, the concentration of dissolved CO_2 decreases, although the effect of pressure is much more significant. Thus, operation at 7 bar and 80 °C results in approximately 0.1 mol% CO_2 in the liquid phase, whereas under ambient conditions the value is more than five times lower[52, 60, 67].

Consequently, the productivity of liquid-phase products (HCOOH, HCHO, and CH_3OH, depending on catalyst composition and conditions) increased with raising pressure, while the production of gas-phase products decreased. For example, two sets of tests were performed at 8 and 18 bar CO_2. High-pressure operation increased the productivity of liquid-phase products such as HCOOH, HCHO, and CH_3OH, whereas at intermediate pressure, gas evolution may occur, including H_2, CO, and CH_4, depending on the reaction pathways[35, 60, 67, 68].

Overall, as pressure increased, formic acid productivity rose, while H_2 productivity decreased. For example, a TiO_2-based photocatalyst achieved formic acid productivity above 7.0 mol/h kg_{cat} at 8 bar, which increased by 64% at 18 bar. Another titania-based sample prepared by flame spray pyrolysis benefited most from increased pressure, with productivity rising by 240% at 18 bar compared to 8 bar. The benchmark bare TiO_2 P25 (Evonik) showed a 91% increase in HCOOH productivity, from 3.2 to 6.2 mol/h kg_{cat} at 8 and 18 bar, respectively. Similar behaviour was observed for composite materials[60].

3.2. Effect of the hole scavenger (HS)

In photocatalytic CO_2 reduction, rapid recombination of photogenerated electron–hole pairs is a main factor limiting conversion efficiency. To address this, hole scavengers, often called sacrificial agents (SCRs), are added to the reaction system, as recently discussed[35, 52, 69-71]. By preferentially reacting with photogenerated holes, these sacrificial agents suppress charge recombination, prolong electron lifetimes, and increase the probability of CO_2 reduction at the catalyst surface[72-74]. Figure 3 shows the variation in productivity as a function of HS concentration, adapted from Bahadori et al.[51].

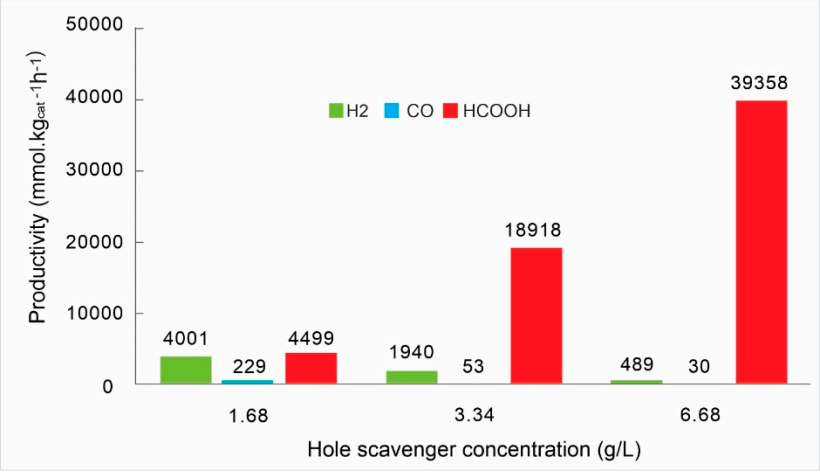

 doi:10.20944/preprints202604.1590.v1

Figure 3. Effect of HS concentration on productivity. Reproduced under the Creative Commons Licence from[51].

Several classes of hole scavengers have been investigated, each with distinct effects on product selectivity and overall activity. Alcohols such as methanol, ethanol, and isopropanol are among the most commonly used, as they are readily oxidised by photogenerated holes and effectively improve electron availability for CO_2 reduction. Isopropanol, in particular, has shown favourable performance due to its efficient hole-trapping ability, while methanol often enhances product generation because of its small molecular size and high diffusivity in aqueous solution. Ethanol typically exhibits intermediate behaviour, with lower product generation than methanol and isopropanol[53]. Water, although sometimes acting as a hole scavenger, is less effective due to its lower nucleophilicity and limited ability to sustain high CO_2 solubility under reaction conditions. Recent kinetic analyses further support these distinctions. Studies employing fractional-order reaction modelling have shown that methanol provides the highest overall photoactivity in CO_2 reduction, consistent with its superior diffusivity (2.27×10^{-9} m^2 s^{-1} at 298 K, 1 bar), which enables more efficient mass transport of reactive intermediates. In contrast, ethanol and isopropanol, with lower diffusivities, depend more on their electron-donating abilities to maintain hole scavenging efficiency. Among these, isopropanol exhibited higher product generation rates than ethanol, consistent with its stronger nucleophilic character (higher pKa). These findings demonstrate that both molecular diffusivity and nucleophilicity determine scavenging effectiveness, with methanol excelling through transport properties and isopropanol through stronger electron donation[75].

The mechanistic role of sacrificial agents, however, remains not fully clarified. Beyond suppressing electron–hole recombination, they can generate new reaction pathways or favour those that are thermodynamically advantageous. For example, water is a natural electron donor but suffers from slow oxidation kinetics, limiting its efficiency in driving CO_2 photoreduction. Ethanol, by contrast, is often used to improve catalytic performance because it acts as a hole scavenger and actively participates in the reaction pathway. Under illumination, ethanol can be oxidised by photogenerated holes on TiO_2 to form acetaldehyde (C_2H_4O), thereby freeing photogenerated electrons for CO_2 reduction at catalytic sites. This dual role, serving as an electron donor and generating value-added oxidation products, highlights ethanol's contribution compared to water alone[70, 72].

Additional photocatalytic studies with Cu–P25 further demonstrate the role of ethanol as a sacrificial agent under realistic reaction conditions. Experiments with a CO_2 flow saturated with water vapour revealed that varying the ethanol feed strongly influenced CO_2 reduction performance. Control experiments without CO_2, using He as the carrier gas, confirmed the specific contribution of ethanol in modulating the photocatalytic process. These results highlight the importance of optimising sacrificial agent concentration, as both insufficient and excessive ethanol can affect charge separation efficiency and product distribution[72].

Figure 4 shows the relationship between hole scavenger concentration, product distribution, and productivity in the photocatalytic system.

Beyond organic compounds, inorganic hole scavengers such as sodium sulphite (Na_2SO_3) have shown outstanding performance in photocatalytic CO_2 reduction. Systematic comparisons with amines, alcohols, and polyalcohols revealed that Na_2SO_3 resulted in a progressive accumulation of reduction products over time, with HCOOH as the dominant product under basic conditions, and HCHO and CH_3OH forming at neutral pH, although with lower productivity[35, 52]. Figure 5 shows the relationship between sulphite concentration and sulphite conversion after 24 hours of reaction, adapted from Bahadori et al.[51].

 doi:10.20944/preprints202604.1590.v1

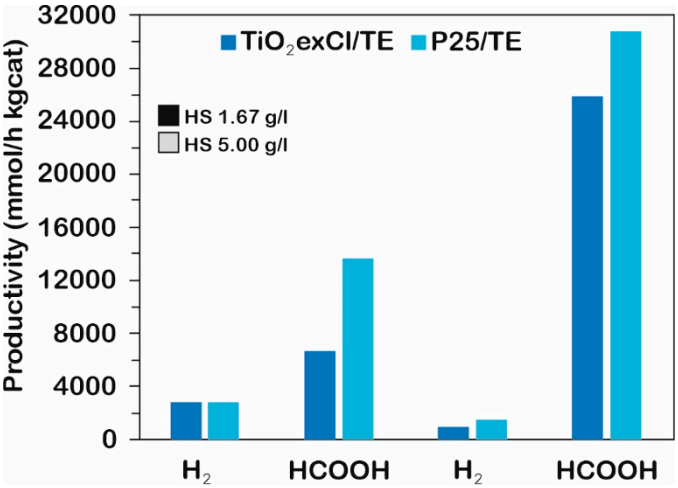

Figure 4. The effect of hole scavenger concentration on products distribution and productivity. Reproduced under the Creative Commons licence from[60].

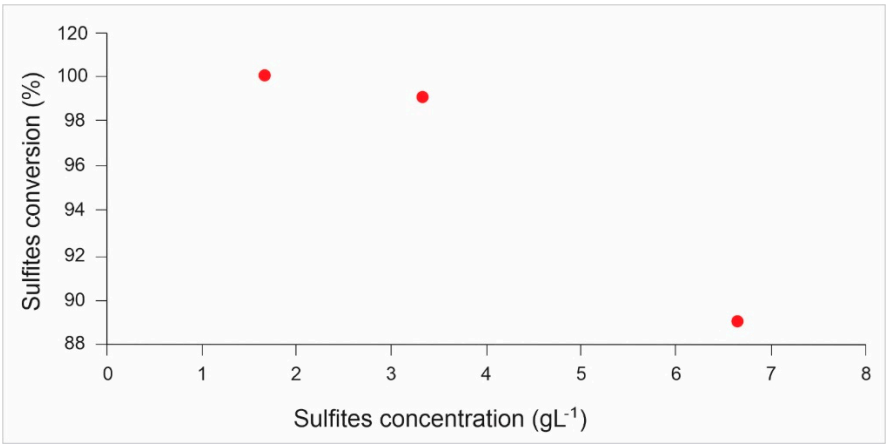

Figure 5. Sulphite conversion vs. Sulphite concentration. Readapted from [51].

Remarkably, negligible H_2 evolution was observed during Na_2SO_3 consumption, suggesting a faster CO_2 reduction rate compared to competing water reduction. Once the hole scavenger was fully depleted, accumulated organic intermediates acted as secondary hole scavengers, leading to increased H_2 generation. At pH 14, formic acid productivity increased sharply with Na_2SO_3 concentration, reaching 26–31 mol/h kg_{cat} compared to 6–14 mol/h kg_{cat} at lower concentrations[35, 51, 68].

Further tests confirmed that increasing the Na_2SO_3 concentration (from 1.66 to 6.68 g L^{-1}) enhanced HCOOH formation ninefold, while suppressing gas-phase products (H_2, CO, CH_4) until the scavenger was depleted. These results highlight the unique advantage of Na_2SO_3 as a cost-effective, non-competing hole scavenger with high selectivity for liquid-phase products[35, 51, 68].

The choice of hole scavenger influences both the reaction rate and product distribution. Systems employing alcohol-based scavengers tend to favour the formation of CO and CH_4, while amine-based scavengers (e.g., triethanolamine, TEOA) may alter product selectivity. More complex organic molecules, such as EDTA, can offer strong hole-scavenging activity but complicate mechanistic interpretation due to multiple oxidation pathways[76]. Table 2 presents an overview of the reported effects of hole scavengers on CO_2 photoreduction.

 doi:10.20944/preprints202604.1590.v1

Table 2. Summary of the effect of hole scavengers on the photoreduction of CO_2.

Hole Scavenger	Examples	Main Role	Effect on Products	Advantages	Limitations
Alcohols (organic)	Methanol, Ethanol, Isopropanol	Donate electrons, trap holes	Favor CO and CH_4 formation; ethanol can yield acetaldehyde (C_2H_4O) as oxidation product	Abundant, easy to handle, tune selectivity, dual role (electron donor + oxidation pathway)	Susceptible to side reactions; selectivity depends on diffusivity & nucleophilicity; may generate competing intermediates
Amines (organic)	Triethanolamine (TEOA), EDTA	Hole scavenger	Often enhance H_2 evolution; multiple oxidation routes	Strong scavenging efficiency, enhance charge separation	Can complicate mechanistic interpretation, undesired H_2 production
Inorganic sulphites	Na_2SO_3, Na_2SO_4	Non-competing hole scavenger	Promote HCOOH at high pH; suppress H_2, CO, CH_4 until scavenger depletion	Low cost, industrially relevant, high selectivity for liquid-phase products	Performance strongly pH-dependent; productivity declines once consumed
Water	H_2O	Natural electron donor	Limited activity; sluggish oxidation kinetics → O_2 evolution slow	Environmentally benign, no additives required	Inefficient scavenger, poor CO_2 solubility, low selectivity

3.3. Effect of pH

The reaction mechanism can be altered by modifying the pH[68, 77]. The productivity of the primary products, HCOOH and H_2, is significantly enhanced under basic pH conditions. Increasing the pH promotes CO_2 solubility by forming CO_3^{2-} or HCO_3^-, which are further reduced to HCOOH or HCHO through subsequent reactions. The following photo-reforming step may also cause the produced liquid products to evolve into gas phase products (H_2 and CO). According to the literature, the back-oxidation of HCHO to HCOOH is more likely under basic pH conditions[68, 78].

P25 is a photocatalyst that tends to generate CO or HCOOH rather than highly reduced hydrocarbons. However, for methane formation, CO can serve as a precursor via an alternative hydrogenation route[79-81]. According to Bahadori and co-authors[51], Figure 6 illustrates the consecutive pathways involved in CO_2 photoreduction and photoreforming under basic pH conditions.

The photocatalytic performance of CO_2 reduction in H_2O using a Co-doped TiO_2 photocatalyst supported on graphene (rGO) was investigated at different pH values (6.5–7.5)[82]. Methanol yield was higher at pH 7.5 than at pH 6.5 or 7, due to increased CO_2 dissolution. Under alkaline conditions, photo-induced holes were scavenged by hydroxyl ions, which were converted into hydroxyl radicals, thereby accelerating the rate of methanol formation.

In another study[83], the effect of the basic properties of MgO on the photoactivity of MgO/TiO_2 nanocomposites was investigated. The photocatalytic efficiency of pure TiO_2 and TiO_2/MgO nanocomposites was tested in both water and 0.1 M NaOH solution. Methane production was higher in the NaOH solution than in water, as CO_2 is more soluble in NaOH than in pure water. Before the photoreaction, the NaOH solution stabilised at a pH of 6.74 after 20 minutes of CO_2 bubbling, while the aqueous system reached a pH of 4.18. This suggests that, in the NaOH system, the reaction primarily involved HCO_3^-, then, ions rather than dissolved CO_2. The changes in acidity also indicated

 doi:10.20944/preprints202604.1590.v1

CO_2 consumption: after 6 hours, the pH in the aqueous medium increased to 4.61, while in the NaOH solution it rose to 7.24. These pH changes reflected the effective CO_2 concentration in the solutions, with higher pH indicating more extensive CO_2 photoconversion[83].

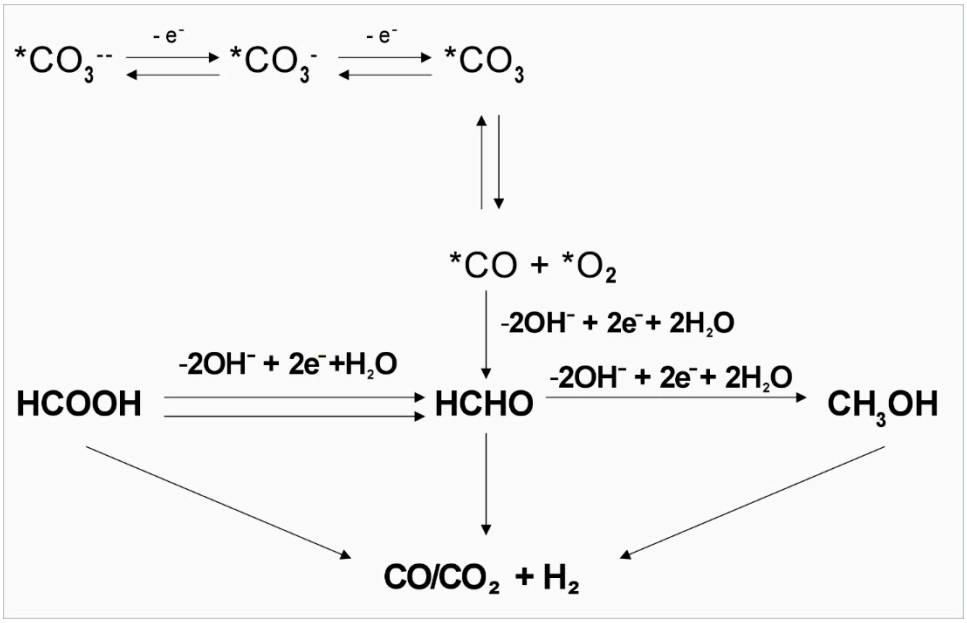

Figure 6. Consecutive pathways for the photoreduction of CO_2. Reproduced from [51] under the Creative Commons Licence.

A study investigated the influence of different reaction conditions on CO_2 photoreduction and water splitting using a TiO_2–Cu catalyst. The results showed that adding various electrolytes, which acted as pH modifiers or electron donors, promoted the selective formation of specific products and significantly affected the reaction kinetics. The effect of acidic conditions on photoreduction depended strongly on the reaction medium. For example, the presence of acetic acid favoured methane production, whereas sodium oxalate enhanced hydrogen generation[79]. During the reaction, the metallic copper in the TiO_2-Cu catalyst transformed into various CuO and Cu_2O phases, causing fluctuations in the results but also extending the lifespan of photogenerated charge carriers and the catalyst. The study suggested that catalyst efficiency can be improved by making minor adjustments to the reaction medium, thereby increasing its ability to produce valuable C1 and C2+ molecules and renewable fuels such as hydrogen.

Table 3 summarises the reported effects of pH on the photocatalytic reduction of CO_2, adapted from the above reported references.

Table 3. Effect of pH on the photoreduction of CO_2.

Catalyst/System	pH / Medium	Main Products	Key Observations
General (various catalysts)	Basic pH	HCOOH, H_2	Enhanced productivity; CO_2 solubility promoted via HCO_3^- and CO_3^{2-} formation; HCHO may back-oxidise to HCOOH.
P25 TiO_2	Neutral / Basic	CO, HCOOH; CH_4 (via CO hydrogenation)	Tends to generate CO or HCOOH; methane may form via alternative hydrogenation route.

 doi:10.20944/preprints202604.1590.v1

Co-doped TiO_2/rGO	pH 6.5–7.5	CH_3OH	Higher methanol yield at pH 7.5 due to increased CO_2 dissolution and scavenging of h^+ by OH^-.
MgO/TiO_2 nanocomposites	Water (pH 4.18) vs 0.1 M NaOH (pH 6.74)	CH_4	Higher methane production in NaOH solution; CO_2 converted as HCO_3^-; pH increase confirmed CO_2 consumption.
TiO_2-Cu	Various electrolytes / acidic-basic conditions	CH_4, H_2, C1–C2+ products	Electrolytes acted as pH adjusters/electron donors; acetic acid enhanced CH_4, sodium oxalate boosted H_2. Catalyst phases evolved (Cu, CuO, Cu_2O).

3.4. Effect of reaction medium

The effect of the reaction medium was investigated using TiO_2 as a photocatalyst. Vapour and liquid phase tests were compared under specifically optimised conditions for each. It was evident that the reaction medium controls the selectivity and activity of the process[77, 84, 85]. Considering the experimental results as a whole, it can be inferred that reduction processes associated with the valence band of titanium dioxide may proceed through two distinct pathways, as illustrated in Figure 7.

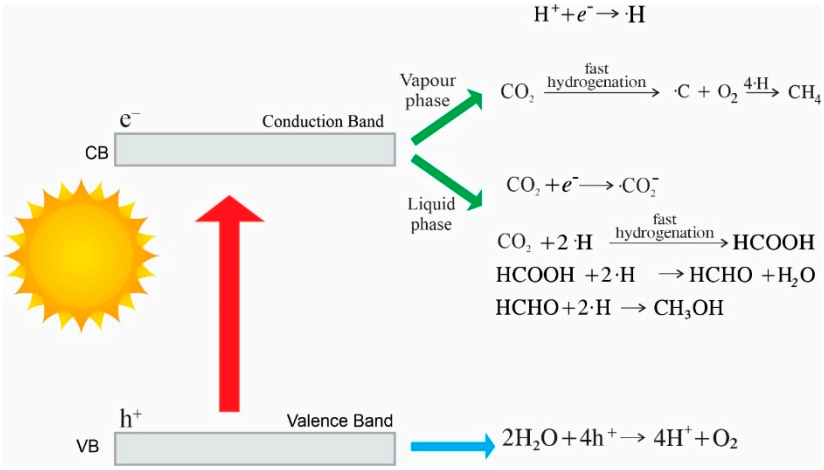

Figure 7. Different reaction mechanisms in vapor and liquid phases. Reproduced under the Creative Commons Licence from[77].

In the first case, rapid deoxygenation leads to C species that are subsequently reduced, whereas in the liquid phase, hydroperoxo species can undergo hydrogenation, resulting in possible intermediate products. Accordingly, the product distribution in the liquid phase was 74% formic acid, 18% formaldehyde and 8% methanol.

Direct production of methane was also observed in the gas phase, while intermediate reduction products formed with H_2 in the liquid phase. For tests conducted in the liquid phase, it should be noted that achieving substantial productivity depends on creating sufficiently high CO_2 solubility in water, which can be accomplished by using high pressure or a basic pH. Table 4 summarises the reported effects of the reaction phase on CO_2 photoreduction.

Furthermore, the effect of different solvents in liquid phase reaction has been effectively discussed in[86]. The paper further discusses the possibility of photolysis of solvents different from water and possible hole scavengers under different irradiation wavelength from UVC to visible light. The effect of different solvents is particularly relevant in case of homogeneous photocatalysts, since the solvent induced field may affect the organometal complex structure[87].

 doi:10.20944/preprints202604.1590.v1

Table 4. Summary of the effect of reaction phase for the photoreduction of CO_2.

Catalyst	Reaction Medium	Conditions	Products / Selectivity	Notes
TiO_2	Vapor phase	Optimised conditions	Direct methane production observed	Fast deoxygenation leads to C species reduction
TiO_2	Liquid phase	High CO_2 solubility required (pressure or basic pH)	74% HCOOH, 18% HCHO, 8% CH_3OH; H_2 also produced	Hydroperoxo species undergo hydrogenation → intermediates

3.5. Effect of Catalyst amount

The influence of catalyst concentration on CO_2 photoreduction was investigated under strongly basic conditions (pH 14) in the presence of sodium sulphite (1.66 g L^{-1}) as a hole scavenger. Catalyst loading was progressively decreased in the photoreactor to evaluate its effect on products distribution. Lower catalyst concentrations enhanced productivity, due to improved light distribution throughout the reactor. At higher concentrations, increased particle density promoted light scattering, which limited photon penetration and reduced overall efficiency[51].

The productivity of the gas-phase products (H_2 and CO) and HCOOH was evaluated both normalised per catalyst mass and as absolute values. When normalised, the highest yields of H_2 and HCOOH were obtained at 0.031 g L^{-1} of P25, indicating that this concentration maximises catalytic efficiency per unit mass. However, in the absolute data, the highest yield of HCOOH was observed at the largest catalyst concentration tested, while its production progressively decreased as the catalyst was diluted. In contrast, hydrogen and CO yields decreased steadily as catalyst loading increased, consistently with light-scattering limitations. To further assess the role of catalyst amount, the chemical energy stored in the products was calculated based on the enthalpies of combustion of HCOOH, H_2 and CO. For the two extreme catalyst concentrations tested (0.031 and 0.5 g L^{-1}), the results showed that the total stored energy increased with higher catalyst loading. However, the distribution of products and, consequently, the form of energy storage varied significantly. At lower catalyst concentration, the process favoured the generation of gaseous products (H_2 and CO), which are easier to separate and use for energy conversion. In contrast, at higher catalyst concentrations, liquid-phase HCOOH was the predominant product, although its separation and utilisation were less straightforward due to its high dilution in the aqueous phase [51] .

According to the literature, the continuous photocatalytic conversion of CO_2 into methanol was evaluated using Cu nanoparticles synthesised in the hydrophilic 3-methyl-n-butylimidazolium tetrafluoroborate (BMIm·BF_4) ionic liquid and embedded in TiO_2 (P25) within an optofluidic microreactor[88, 89]. The amount of photocatalyst used can influence the efficiency with which CO_2, OH^-, and photons move through the active layer, and can also alter the available surface area for converting CO_2 into CH_3OH. Consequently, the production of CH_3OH per gram of Cu increased significantly as the loading rose from 0.5 to 2 mg cm^{-2}, rising from r = 73.4 μmol g^{-1} h^{-1} to r = 167.5 μmol g^{-1} h^{-1} under UV light, and from r = 22.3 μmol g^{-1} h^{-1} to r = 36.1 μmol g^{-1} h^{-1} under visible light irradiation. Similar trends were observed for the yields of C_2H_5OH.

At lower catalyst loadings (below 2 mg cm^{-2}), fewer electron-hole pairs were generated due to the limited photoactive exposed area, resulting in lower yields. As the photocatalyst loading increased from 2 to 3 mg cm^{-2}, the performance of a planar optofluidic microreactor-based system decreased[88]. This was due not only to particle agglomeration, which reduced the available photoactive surface and created shadowing effects, but also to an increase in the thickness of the photocatalyst layer. A thicker layer can also increase mass transfer resistance, potentially due to the formation of boundary layers, making it more difficult for the reactants to access the active sites. These effects together resulted in a 65% reduction in CH_3OH yield.

 doi:10.20944/preprints202604.1590.v1

The efficiency of CO_2 reduction in H_2O over Co-doped TiO_2 supported on reduced graphene oxide (rGO) photocatalyst was studied using different catalyst amounts (0.1 to 0.7 mg)[82]. Methanol production decreased as the catalyst amount increased at pH 7.5. This reduction was attributed to increased generation of carbonate radicals at higher catalyst amounts. Catalyst amounts from 0.3 to 0.7 mg showed greater capability in activating H_2O, leading to faster CH_3OH formation. However, these loadings resulted in slightly lower CH_3OH production compared to the 0.1 mg catalyst dosage. The formation rate of intermediates, such as formate, was faster with catalyst amounts from 0.3 to 0.7 mg than their consumption rate. This imbalance led to catalyst deactivation, defined as "adsorbed formate poisoning".

The hierarchical yolk-shell structure of $CuCo_2S_4$ (CCS) thiospinel was incorporated into Bi-modified TiO_2 nanoparticles using an innovative calcination method based on the isoelectric point. This process introduced a strong electron donor to counteract the self-oxidation of holes within a Z-scheme mechanism. Catalyst loading control in the photoreduction process was examined through multiple experiments, varying the amount of CCS@3B-TiO_2 from 0.1 to 0.5 g/L. Increasing the catalyst loading from 0.1 to 0.3 g/L significantly enhanced CO_2 reduction activity, resulting in CH_4 and CO yields of 42.2 and 25.5 μmol/g, respectively. This increase in productivity was likely due to a notable rise in active sites and improved light absorption from the higher specific surface area. However, further increasing the catalyst loading from 0.3 to 0.5 g/L reduced the yields to 32.4 μmol/g for CH_4 and 21.2 μmol/g for CO. The decline in reaction performance can be attributed to increased solution opacity caused by excessive catalyst dosage, which limited light absorption and reduced accessibility to surface sites due to catalyst agglomeration[90]. Table 5 summarises the reported effects of catalyst dosage on photocatalytic performance.

Table 5. Effect of catalyst dosage on the photocatalytic performance.

Catalyst / System	Catalyst Amount / Loading	Conditions	Main Products	Key Observations
TiO_2 P25	0.031 – 0.5 g L^{-1}	pH 14, Na_2SO_4 1.66 g L^{-1}, liquid phase	HCOOH, H_2, CO	Low loading (0.031 g L^{-1}) maximises H_2 and CO per mass; high loading favours HCOOH; light scattering limits efficiency at high concentration
Cu nanoparticles in BMIm·BF4 ionic liquid / TiO_2 P25	0.5 – 3 mg cm^{-2}	Optofluidic microreactor, UV and Vis light	CH_3OH, C_2H_5OH	Increasing loading improves yield up to 2 mg cm^{-2}; above 2–3 mg cm^{-2}, shadowing, agglomeration, and mass transfer resistance reduce yields
Co-doped TiO_2/rGO	0.1 – 0.7 mg	pH 7.5, aqueous	CH_3OH, formate intermediates	Methanol production drops with increasing catalyst amount due to carbonate radicals; intermediate formation faster at 0.3–0.7 mg, causing slight deactivation
CCS@3B-TiO_2 ($CuCo_2S_4$/Bi-TiO_2)	0.1 – 0.5 g L^{-1}	Liquid phase, controlled loading	CH_4, CO	Activity increases from 0.1→0.3 g L^{-1}; further increase to 0.5 g L^{-1} reduces yields due to light opacity and surface site agglomeration

3.6. Effect of catalyst size

 doi:10.20944/preprints202604.1590.v1

The photocatalytic activity of a catalyst is strongly influenced by its particle size and shape, as a smaller particle size provides more accessible surface active sites and increases the likelihood of interfacial charge separation due to the shorter pathway for charges generated in the bulk to react with surface reactants, compared to larger particles. In turn, the synthesis of photocatalysts has a crucial effect on their morphology and size[91].

It is widely recognised that many factors can significantly affect the photocatalytic performance of TiO_2, including particle size, specific surface area, porous structure, crystalline phase, and exposed surface facets. Extensive research has shown that morphology plays a crucial role in determining TiO_2's photocatalytic activity. Consequently, recent studies have focused on enhancing TiO_2 photocatalytic properties by tailoring its morphology[92].

One-dimensional (1D) TiO_2 nanostructures, such as nanofibers, nanotubes, nanorods, and nanowires, exhibit advantages for photocatalytic applications due to their 1D geometry. These structures typically provide a larger surface area than bulk TiO_2, increasing the number of reactive sites and reducing electron–hole recombination. Additionally, their elongated geometry enables rapid interfacial charge carrier transport by shortening diffusion distances, thus enhancing photocatalytic efficiency[92].

Various methods have been developed for synthesising 1D TiO_2 nanomaterials, including chemical vapour deposition (CVD), template-assisted approaches, anodic oxidation, solvothermal and hydrothermal synthesis. Among these, the hydrothermal method is particularly attractive due to its simplicity, cost-effectiveness and ability to control both shape and size. This method has become a widely adopted protocol for producing 1D TiO_2 nanostructures. The resulting morphologies can be tuned by adjusting synthesis parameters such as reaction temperature and duration, alkaline concentration, TiO_2/NaOH ratio, post-synthesis washing procedures and the crystalline phase of the TiO_2 precursor. However, studies have shown that the crystalline phase of the starting material does not affect nanotube formation. Therefore, precise control of synthesis conditions is essential to obtain the desired 1D morphology[93].

One-dimensional TiO_2 nanostructures with different shapes exhibit distinct photocatalytic performance also in degrading organic pollutants, underscoring the significant influence of morphology on activity[94]. For example, the impact of morphology on the photocatalytic degradation of dyes was studied using various one-dimensional TiO_2 nanostructures, such as nanotubes, nanofibres and nanowires. The results indicated that nanotubular TiO_2 exhibited the highest photocatalytic efficiency, attributed to its tubular geometry and high hydroxylation, which provide more active sites through oxygen vacancies (V_O).

In addition, increasing the specific surface area is another useful strategy to enhance photocatalytic activity, although there is no universal agreement on this point. The porosity and particle size of nanoparticles determine their surface area. In particular, compared to other nanostructures, one-dimensional TiO_2 nanostructures have a larger specific surface area and a higher rate of photocatalytic CO_2 reduction. Nevertheless, other factors, such as impurities, defects and charge recombination rate may be predominant over surface area.

3.7. Effect of the calcination temperature

Calcination significantly influences the morphology, crystallinity, surface area, pore volume, and phase structure of photocatalysts, which in turn influence photocatalytic performance. Pd-decorated black TiO_2 nanoparticles were synthesised using a sol-gel method followed by calcination in an argon atmosphere. Among the conditions tested, the sample calcined at 400 °C (Pd-BTN-400) showed the highest performance, achieving photocatalytic hydrogen production rates of approximately 5200 μmol H_2 g^{-1} h^{-1} under UV-A and 9300 μmol H_2 g^{-1} h^{-1} under UV-B irradiation, demonstrating its potential for clean energy applications[95].

As reported in the literature, the effects of calcination temperature on the structural and photocatalytic properties of TiO_2 nanoparticles have been extensively investigated. The material can be synthesised by the sol–gel method and then calcined at temperatures typically ranging from about

 doi:10.20944/preprints202604.1590.v1

300 °C to 700 °C. Studies indicate that within the temperature range of 300 °C to 600 °C, phase transition and crystallite size of TiO_2 play a decisive role in determining photocatalytic performance. At higher temperatures, particularly between 600 °C and 700 °C, particle size becomes the main factor influencing photocatalytic activity. These findings show that simultaneous control of crystallite size and particle size is a critical parameter for optimising the photocatalytic properties of TiO_2 nanoparticles[96, 97].

The effect of calcination temperature on TiO_2/reduced graphene oxide (rGO) composites for CO_2 photoreduction has been widely studied in the literature. Reduced graphene oxide (rGO) is a chemically reduced form of graphene oxide that partially restores the electrical conductivity and high surface area characteristic of graphene, making it an effective support material for improving charge separation and enhancing photocatalytic activity. Experimental observations indicate that calcination temperatures above 500 °C can cause a significant decrease in both the band gap energy and the BET surface area of the composite, while also promoting aggregation of TiO_2 particles within the TiO_2/rGO structure. These structural and electronic changes directly influence the photocatalytic performance of the composite material[98].

The highest yields of methane (CH_4) and carbon monoxide (CO) were obtained for the TiO_2/rGO sample without calcination, followed by the sample reduced in hydrogen at 1000 °C, demonstrating the strong influence of rGO and calcination conditions on photocatalytic performance. Table 6 shows the effect of calcination temperature on the properties of the photocatalysts, while Figure 8 presents the product yields obtained with the tested photocatalysts during CO_2 photoreduction using H_2O, adapted from the literature[98].

Table 6. Effect of calcination temperature on textural and optical properties of TiO_2/rGO catalysts. Readapted from[98].

Photocatalyst Name	S_{BET} (m^2/g)	Carbon cont. (wt.%)	E_g (eV)
TiO_2	312	0	3.28
TiO_2/rGO-10	156	8.0	3.26
TiO_2/rGO-10-500	126	6.7	3.28
TiO_2/rGO-10-800	39	5.4	2.98
TiO_2-800	6	-	3.02
TiO_2/rGO-10-1000	25	6.4	2.90
TiO_2-1000	2	-	3.01

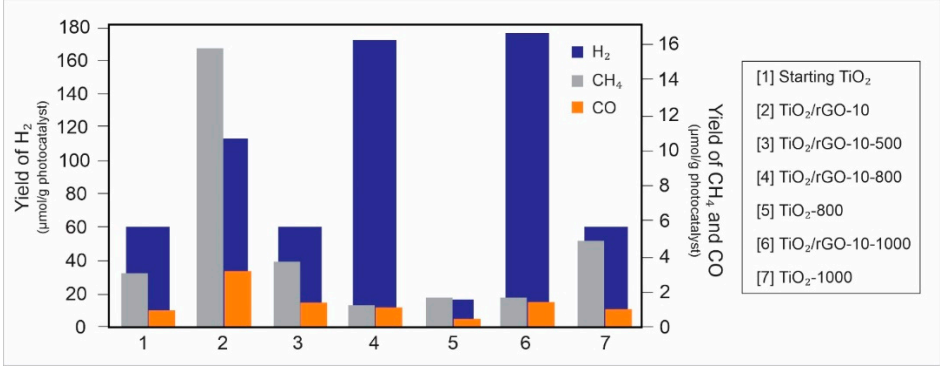

Figure 8. Product yield of tested photocatalysts during CO_2 photoreduction with H_2O. Readapted from[98].

The (x)TNPs-CN/y composites were synthesised using a wet chemical method. The materials contained varying amounts of titania nanoparticles (TNP, 15–30 mg per 25 mg of g-C_3N_4, CN) and were prepared at calcination temperatures between 300°C and 500°C and were evaluated for the photoreduction of CO_2 in the presence of CH_4 at room temperature. During annealing, bulk g-C_3N_4

 doi:10.20944/preprints202604.1590.v1

exfoliated into nanosheets, increasing the exposed surface area and the number of terminal amine groups as the calcination temperature rose. Consequently, the turnover frequency (TOF) showed a clear dependence on the calcination temperature[99].

Figure 9, adapted from the paper by Chen and co-authors[99], shows the performance of the (x)TNPs-CN/y catalyst for CO production at calcination temperatures of 400, 450, and 500 °C. The experiments were conducted at an absolute pressure of 30 kPa with a CH_4:CO_2 ratio of 1:2, using 50 mg of catalyst and a TNPs loading of 20 mg. The results illustrate the effect of calcination temperature on the catalytic activity for CO formation under the reaction conditions investigated.

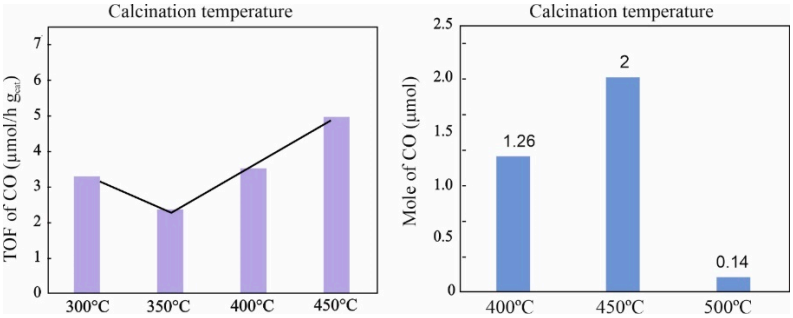

Figure 9. The effect of calcination temperature of the (x)TNPs-CN/y catalysts on the production of CO. Readapted from[99].

However, no optimal calcination temperature was identified for CO production, prompting investigation of a broader temperature range. The results showed that the catalyst displayed limited activity for CO formation when calcined at 500°C. This behaviour is due to partial decomposition of g-C_3N_4 at this temperature, which reduces the efficiency of electron transfer from g-C_3N_4 to the TNPs[99].

4. Case Studies for Different Photocatalysts

Different materials may, in principle, be suitable for the photoreduction of CO_2. Semiconductor photocatalysts with Eg > 3.0 eV are active only under UV light, while those with Eg < 3.0 eV are also effective under visible light. The band positions of common semiconductors (such as TiO_2, Cu_2O, CdSe, ZnO, CdS, WO_3 and Bi_2WO_6) and the redox potential versus the Normal Hydrogen Electrode (NHE) for CO_2 reduction at pH 7 are important considerations. The relationship between band energy and redox potential for product selectivity determines the types of compounds that can be formed. The interaction between redox potential and band gap also applies to the reduction of CO_2 to various hydrocarbon fuels, such as CH_3COOH, HCOOH, and CH_4.

Examples are described in the following paragraphs.

4.1. TiO_2 based photocatalysts

Titanium dioxide (TiO_2) is one of the most studied semiconductor photocatalysts, used in the anatase or rutile crystal phases, two of the most common and stable polymorphs, or as a mixture of these, as in the well-known P25 photocatalyst. Its widespread use is attributed to its broad availability, chemical inertness, low cost and low toxicity. However, recent investigations classify TiO_2 as possibly genotoxic when used as a food additive, depending on its particle size. Other applications raise fewer concerns[100, 101].

Its use in photocatalysis is highly specialised in environmental remediation and energy generation. Almost two-thirds of recent publications on photocatalysis use TiO_2 as the photocatalyst. Depending on the specific electronic pathway followed by a given species, the potential of photogenerated electrons and holes can be identified upon their generation by photon absorption[102].

 doi:10.20944/preprints202604.1590.v1

TiO_2 is characterised by a large band gap, which enables photocatalysed reactions to occur only in the UV range, with radiation below 365 nm[103]. This limits the applicability of titanium dioxide for exploiting sunlight, as UV radiation accounts for only about 5% of the total solar spectrum[104]. In addition, the photogenerated charges in solid photocatalytic processes must survive long enough to reach the surface of the photocatalyst and interact with the adsorbed species. This further restricts the activity of titania, since the rate of charge recombination is high, with survival times on the nanosecond scale[65, 105-108]. One of the main obstacles to the practical application of TiO_2 as a photocatalyst is charge recombination at deep-level defects, which reduces the performance of TiO_2[109-111].

To address both these points, the photocatalytic performance of TiO_2 has mostly been enhanced by surface modification, using either transition metals such as Pt, Au, and Ag, or non-metallic elements. The deposition of metallic nanoparticles (NPs) is a common method to extend the lifetime of the electron-hole pair, as they act as electron sinks (for example, Pt). Metals can also exploit the surface plasmon resonance (SPR) effect and, consequently, supply "hot electrons" to boost activity at visible wavelengths, for example with Au[59, 61, 64, 66, 67, 112-119].

The photocatalytic reduction of CO_2 at high pressure using TiO_2 powders in the presence of a hole scavenger has previously been reported. In this system, TiO_2 powders were suspended in an isopropyl alcohol solution and irradiated with an Xe lamp. Methane was identified as the principal reduction product of CO_2. Isopropyl alcohol acted as the hole scavenger, facilitating charge separation and enhancing photocatalytic activity. The conversion of CO_2 to methane in a high-pressure reactor was carried out using unmodified commercial titanium dioxide. Under optimised experimental conditions, the process yielded 1.3 μmol $(g_{Ti})^{-1}$ of methane, corresponding to a formation rate of 0.43 μmol $(g_{Ti})^{-1}$ h^{-1}[150].

Solution Plasma Processing (SPP) technology has been used to introduce shallow-level defects that can thermally stimulate the migration of trapped electrons across deep-level defect states. Coloured wide-bandgap semiconductor oxides with abundant mid-gap states have long been considered promising candidates for visible-light-responsive photocatalysis. However, their practical performance is often limited by charge recombination at deep-level defects, which remains a major barrier to achieving efficient photocatalytic activity To address this limitation, a strategy was developed involving the creation of shallow-level defects above the deep-level states, enabling thermally activated migration of trapped electrons and thereby reducing recombination losses. SPP was applied to pre-synthesised yellow TiO_2 rich in oxygen vacancies (V_O). This treatment introduced hydrogen dopants into the TiO_2 lattice, generating shallow-level defects above the V_O states while maintaining the material's visible-light absorption[120-122]. At elevated temperatures, the SPP-modified TiO_2 showed a remarkable enhancement in photocatalytic performance, achieving a 300-fold increase in CO_2 reduction under simulated solar light and a 7.5-fold improvement in acetaldehyde degradation under UV irradiation. To further assess the effect of this strategy, photocatalytic (PC) and photothermocatalytic (PTC) CO_2 reduction experiments were conducted under solar and visible light irradiation. The results clearly demonstrated the superiority of PTC over conventional PC. Under solar light, PC with fresh catalyst produced modest CO and CH_4 productivity of 0.13 and 0.11 μmol g^{-1} h^{-1}, respectively, with a Rate of Reacted Electrons (RRE) of 1.14 μmol g^{-1} h^{-1}. In contrast, PTC achieved much higher CO and CH_4 productivity of 23.1 and 4.79 μmol g^{-1} h^{-1}, respectively, corresponding to a RRE of 84.64 μmol g^{-1} h^{-1} and a methane selectivity of 45.3%. After thermal treatment (T-2 h), PC activity improved moderately (CO = 1.03 μmol g^{-1} h^{-1}; CH_4 = 0.09 μmol g^{-1} h^{-1}; RRE = 2.78 μmol g^{-1} h^{-1}), whereas PTC exhibited a dramatic enhancement, reaching CO and CH_4 yields of 38.99 and 11.93 μmol g^{-1} h^{-1}, respectively, with an RRE of 173.42 μmol g^{-1} h^{-1} and methane selectivity of 55.0%[122].

A similar trend was observed under visible light. PC activity was limited, with CO yields of only 0.08–0.395 μmol g^{-1} h^{-1} and no detectable methane formation. By contrast, PTC consistently delivered superior performance, producing CO and CH_4 yields of 0.62 and 0.17 μmol g^{-1} h^{-1} (RRE = 2.6 μmol

 doi:10.20944/preprints202604.1590.v1

g^{-1} h^{-1}, CH_4 selectivity = 52.3%) for T-0 h, increasing to 3.51 and 1.16 μmol g^{-1} h^{-1} (RRE = 16.3 μmol g^{-1} h^{-1}, CH_4 selectivity = 56.9%) after T-2 h[122].

Overall, these findings demonstrate that SPP-treated TiO_2 with shallow-level defect engineering not only suppresses charge recombination but also enables activity for CO_2 reduction, particularly under photothermal catalytic conditions. Compared to conventional photocatalysis, PTC achieved over an order of magnitude higher activity and significantly improved methane selectivity, underscoring its promise for solar-driven CO_2 conversion and related energy and environmental applications.

4.2. g-C_3N_4 photocatalysts

Graphitic carbon nitride (g-C_3N_4) is a more recent photocatalyst with an interesting structure and properties. It is metal-free, containing only the Earth's most abundant elements, carbon and nitrogen, making it a green alternative to inorganic semiconductor photocatalysts. The distinctive properties of g-C_3N_4 include its optical bandgap in the visible region, semiconducting behaviour, thermal and chemical stability, and tuneable texture and structure[91, 123].

It has a bandgap of 2.7 eV, with the conduction and valence bands located at -1.4 and 1.3 eV vs NHE at pH 7, respectively. Due to its small bandgap, it can partially absorb the visible region of the spectrum (λ < 460 nm). However, it has certain limitations that affect its photocatalytic activity, such as a small surface area in bulk form, rapid charge recombination, moderate oxidation ability, and low charge carrier mobility.

The g-C_3N_4 produced by simple polymerisation often encounters challenges such as low specific surface area, limited visible light absorption range, high rates of photogenerated carrier recombination, and poor charge transfer efficiency, resulting in suboptimal catalytic performance. Consequently, recent research has focused on modifying and optimising the composition and structure of g-C_3N_4 to enhance its efficiency in photocatalytic solar-to-chemical energy conversion. Various surface modification strategies have been used to address the drawbacks of photocatalysts and improve CO_2 photoreduction.

To enhance the photocatalytic activity of these materials, several strategies have been employed, including decoration with metal nanoparticles (NPs), structural doping, exfoliation and nanostructuring, structural modifications, modification with plasmonic and carbonaceous materials, formation of heterojunctions with other photocatalysts and surface protonation[124-126].

For example, the presence of porous structures can significantly increase the specific surface area of g-C_3N_4 and the number of surface-active sites. In one study, g-C_3N_4 was prepared by direct thermal condensation of an organic precursor containing carbon and nitrogen, such as melamine, dicyandiamide, or dicyanamide. The surface area was adjusted by exfoliation using an ultrasound (US) probe operating at variable US power intensities, resulting in an exfoliated material with enhanced specific surface area. The synthesised g-C_3N_4 catalysts, produced using various US power levels, were only partially crystalline and exhibited two main reflections at 2θ = 13° and 2θ = 27.4°, attributed to interlayer stacking of aromatic rings and interplane packing of linear heptazine chains, respectively, similar to graphite. It is important to note that the main diffraction angles of the reflections shifted from the theoretical values given in the JCPDS card to higher diffraction angles. Bulk C_3N_4 samples obtained by calcination at 550°C and 600°C exhibited low surface areas of 9 and 6 m^2/g, respectively, which increased to 28 and 20 m^2/g when 120 W ultrasonic power was applied to partially exfoliate the materials. Diffuse reflectance UV-Vis spectroscopy showed that the samples had a band gap between 2.7 and 2.9 eV. With such a band gap, the material was responsive to visible light. The photocatalytic performance for the photoreduction of CO_2 was determined at 8 bar and 80°C and compared with commercial titania P25 nanopowder. The productivity of formic acid ranged from 4 to 8 mol/h kg_{cat} for all samples, which is significantly higher than values reported in the literature. g-C_3N_4 outperformed the commercial titania catalyst, increasing HCOOH productivity by at least 30%, even for the bulk material, regardless of calcination temperature. The ultrasound

 doi:10.20944/preprints202604.1590.v1

procedure was effective in increasing surface area and improving productivity, especially when the highest ultrasound power (120 W) was applied[127].

A new strategy has been proposed to activate CO_2 molecules by selectively eliminating specific amino groups located along the edges of g-C_3N_4. This targeted removal leads to a local accumulation of photogenerated electrons at the nitrogen atoms adjacent to the removed NH_2 groups. As a result, carbon nitride shows improved light absorption and enhanced photoelectric conversion capability compared with CN-NH_2, resulting in a higher concentration of electrons at the catalytic active sites. This increased electron density is crucial for strengthening the chemisorption and activation of CO_2 molecules, effectively lowering the energy barrier for the CO_2 reduction process. Consequently, the enhanced chemisorption and activation of CO_2 enable g-C_3N_4 to achieve significantly improved photocatalytic performance compared with CN–NH_2[128].

Reconstruction of the g-C_3N_4 nanostructure has proven an effective strategy for enhancing its photocatalytic performance, particularly through the formation of hollow micro- and nano-structures. These architectures promote multiple internal light scattering within the material, increasing light utilisation efficiency and thereby enhancing catalytic activity. In a related study, fusiform-shaped g-C_3N_4 capsules were synthesised by precisely controlling the nucleation kinetics of supramolecular assemblies, demonstrating that careful regulation of the growth process can produce tailored morphologies with improved photocatalytic properties. The resulting micron-nanostructures had ultrathin walls and optimised carbon/nitride ratios, reducing the recombination rate of photogenerated carriers. The hollow structure and higher specific surface area of the fusiform-shaped capsules enhanced light scattering within the material, leading to improved carrier utilisation efficiency. Additionally, the reduced bandgap and negative conduction band position increased the responsiveness of hollow fusiform-shaped g-C_3N_4 capsules (Hf-g-C_3N_4) to visible light, enhancing their photoreduction performance. In terms of hydrogen evolution, Hf-g-C_3N_4 achieved a rate of 7052 μmol g^{-1} h^{-1}, which is 10.9 times higher than that of the bulk structure. Moreover, Hf-g-C_3N_4 can produce CH_4 at a rate of 1.63 μmol g^{-1} h^{-1} without a co-catalyst or hole sacrificial agent in the photocatalytic reduction of CO_2 to CH_4.

5. Photocatalyst Modification Strategies

As mentioned above, the main issue in the photocatalytic process is rapid electron-hole recombination (~10^{-9} s). To address this problem, noble metal nanoparticles are often loaded onto semiconductors. The Fermi level of these nanoparticles is typically close to the energy potential of the semiconductor conduction band, enabling them to capture photo-excited electrons[129-131].

The addition of certain noble metals may also enhance light-harvesting properties through the Surface Plasmon Resonance (SPR) effect. Furthermore, if metal addition is followed by thermal reduction in H_2 to reduce the metal, the presence of the metal can promote titania reduction during activation in the reducing environment, thereby indirectly decreasing the original semiconductor band gap.

Modification can be a surface or bulk phenomenon, with the latter known as doping. In other cases, the bulk junction of two semiconductors may occur, with composite production following certain regular heterojunction concepts[132, 133].

5.1. Modification of TiO_2-based catalysts

Metal deposition is an effective method to enhance the photocatalytic activity of TiO_2 nanocomposites. Compared to other modification methods, it significantly improves electron-hole separation in semiconductor materials. Metal doping in the bulk or addition on the surface is the most widely used surface modification method to prevent the recombination of photogenerated electron-hole pairs on TiO_2[134].

Pure TiO_2 cannot absorb low-energy solar radiation because its high band gap (3.2 eV) corresponds to the UV region of the solar spectrum. Doping with metal ions or non-metal elements may also reduce the band gap energy.

 doi:10.20944/preprints202604.1590.v1

For example, incorporating metal nanoparticles into the TiO_2 matrix can create structural defects and reduce the band gap energy, shifting the absorption threshold towards the visible region. Experimental studies have shown that co-doping TiO_2 with Ni and Bi can progressively lower the band gap energy from 3.1 to 2.84 eV. As a result of this modification, Ni–Bi doped TiO_2 produced a methane (CH_4) yield about 6.5 times higher than that of pristine TiO_2[135].

In various studies, Pt, Au, Ag, Fe, Cu, Ni, Pd, and Ru have been added to TiO_2 and shown to enhance its photocatalytic activity. Some of these metals can exhibit a SPR effect or partially reduce titania during activation, leading to the oxygen defective compound called black titania. Therefore, in addition to bulk doping, which has a structural effect, surface addition may influence activity and light harvesting. Examples are reported in the following references.

A study investigating Au–Ag deposited TiO_2 photocatalysts for CO_2 reduction reported that pure TiO_2 produced syngas as the reaction product. However, when bimetallic Au–Ag catalysts were introduced, the reaction selectivity shifted towards methane (CH_4) formation under UV light irradiation[136].

Pd nanoparticles supported on the surface of TiO_2 have been investigated to enhance the photocatalytic conversion of CO_2 to CH_4. In this approach, a composite was prepared by coordinating $Pd(OAc)_2$ with an N-heterocyclic carbene framework, where the HN structure serves as a platform linking TiO_2 with highly dispersed Pd nanoparticles and enhances CO_2 adsorption. The resulting composite exhibited a high specific surface area of 373 $m^2\ g^{-1}$ and significantly enhanced CO_2 photoreduction performance, achieving a CH_4 production rate of 237 $\mu mol\ g^{-1}\ h^{-1}$ with selectivity above 99.9%. Although the CH_4 evolution rate increased slightly after Pd loading, the CO evolution rate remained unchanged. In contrast, pure TiO_2 and the HN framework alone showed low efficiency for CO_2 reduction to both CH_4 and CO[137].

TiO_2 nanoparticles (NPs) with numerous defects were synthesised using a photochemical method. These nanoparticles served as a substrate for loading highly dispersed Pt NPs, highlighting the interaction between metal sites and oxygen vacancies to improve performance and stability in CO_2 photoreduction. The CO_2 photoreduction efficiency of Pt/TiO_2 photocatalysts was evaluated under simulated sunlight irradiation (380 nm), using H_2-Pt/TiVo-UV or P-Pt/TiVo-UV (commercial TiO_2 dried and treated at 400 ℃ under 5% H_2/air flow, dispersed in H_2PtCl_4 solution, then subjected to 1 h UV treatment) and I-Pt/TiVo-H_2 (commercial TiO_2 dried and treated at 400 ℃ under 5% H_2/air flow, impregnated with H_2PtCl_4 solution, then calcined at high temperature under H_2 flow) as controls. Loading Pt nanoparticles significantly increased the amount of reduction products. The CH_4 content increased 15-fold (47.8 $\mu mol\ g^{-1}$). The sample obtained by calcination in air after Pt impregnation had significantly fewer oxygen vacancies than the sample reduced in H_2. Moreover, the amount of CH_4 produced by H_2-Pt/TiVo-UV increased sharply to 145.6 $\mu mol\ g^{-1}$ when Pt nanoparticles were loaded onto the TiVo-H_2 surface. The absorption edge of pure TiO_2 was around 380 nm, indicating that it could only respond to UV radiation. In contrast, after H_2 treatment, the absorption region of TiVo-H_2 shifted towards visible light at 420 nm. When Pt nanoparticles were loaded, the catalyst's absorption range extended from 420 to 550 nm. The H_2-Pt/TiVo-UV sample prepared by photoreduction exhibited an absorption edge at approximately 530 nm, indicating a high capacity for photoexcitation of charges under visible light irradiation. The binding energies of the variously prepared samples showed different degrees of positive shift compared to pure TiO_2. This suggests that electrons migrate from TiO_2 to the Pt metal sites, which positively influences the enhancement of photoreduction efficiency. For a detailed evaluation of reduction efficiency, the total electron yield of products generated during the CO_2/H_2O reduction process was calculated using the following expression: total electron yield = 2r(CO) + 2r(H_2) + 8r(CH_4). As anticipated, the best-performing catalyst showed excellent photocatalytic activity in converting CO_2 to CO and CH_4, achieving a total electron yield of 382.4 $\mu mol\ g^{-1}\ h^{-1}$. This performance was approximately 26 times higher than that of TiO_2 alone. The high dispersion of Pt nanoparticles acted as electron traps, improving the separation of photogenerated carriers, while the constructive interaction between metal sites and oxygen vacancies enhanced the adsorption capacity for the reactants[138].

 doi:10.20944/preprints202604.1590.v1

Pt NPs were used as the active metal phase in another study reporting the design and fabrication of a novel three-component nanostructured photocatalyst material consisting of TiO_2 nanotube arrays, reduced graphene oxide, and Pt NPs. The use of platinum-deposited catalysts enhanced methane production during the photocatalytic reduction of carbon dioxide under moderate pressure and temperature conditions. Furthermore, varying the duration of platinum deposition on TiO_2 nanotubes (TNTs) resulted in noticeable differences in methane production[139].

Pt-TiO_2 photocatalysts supported on carbon-based materials were prepared using electrostatic self-assembly to investigate CO_2 photoreduction for CH_4 production. 5 wt% Pt/TiO_2 was synthesised by the photodeposition technique. The catalytic activities of the synthesised photocatalysts were related to the particle size and distribution of the active metal. The increased photocatalytic activity of the composites could be attributed to their lower band gaps compared to anatase TiO_2, enabling absorption of visible light. Furthermore, the combined effect of adding Pt and carbon materials prolonged the lifespan of charge carriers, further enhancing the photocatalytic activity of the composites. There was a strong correlation between Pt-TiO_2 particle size and the photoactivity of the catalysts, with smaller particles showing enhanced photocatalytic performance[140].

Pt nanoparticles supported on TiO_2 with oxygen vacancies (Pt/TiO_2-V_O) were synthesised using a single-step flame aerosol method. In situ hydrogenation in the flame introduced oxygen defects, resulting in a strong electronic metal-support interaction (EMSI) between the Pt nanoparticles and TiO_2-V_O. Under light illumination, Pt/TiO_2-V_O showed the highest activity (to methane+CO) of 141 μmol g_{cat}^{-1} h^{-1}, which was 2.4 times higher than TiO_2-V_O, 1.9 times higher than Pt/TiO_2 and 13.8 times higher than commercial titania P25. Pt deposition led to CH_4 production on both Pt/TiO_2 (CH_4 selectivity: 70%) and Pt/TiO_2-V_O (CH_4 selectivity: 81%). The EMSI facilitated electron transfer from defective TiO_2-V_O to Pt NPs, increasing electron density on the Pt surface, enhancing CO_2 photoreduction activity and boosting CH_4 selectivity. Additionally, EMSI-stabilised Pt^0 helped prevent the gradual loss of metallic and oxygen vacancies during an 8-hour photoreaction, thus delaying catalyst deactivation[141].

The photocatalytic performance of noble metal-deposited TiO_2 in the reduction of CO_2 under both UV and visible light exhibited increased light absorption, which enhanced CO_2 photoreduction and resulted in higher selectivity towards CO. The conversion of CO_2 to CO followed the order Rh > Ru > Pt, with the highest activity observed for Rh/TiO_2 at 10.65 μmol/g_{cat} under visible light and 7.84 μmol/g_{cat} under UV light. These values were approximately three and ten times higher, respectively, than those for pristine anatase TiO_2 (0 and 2.43 μmol/g_{cat}). Noble metal nanoparticles, which have a higher affinity for hydrogen, can retain hydrogen more effectively, thereby increasing its availability for the reverse water-gas shift (RWGS) reaction. This, in turn, enhanced the overall photocatalytic activity of the metal nanoparticles, resulting in a higher CO production rate compared to pristine TiO_2. In addition, the Rh/TiO_2 sample exhibited a greater number of basic sites, which resulted in more active centres for CO_2 adsorption due to Rh deposition. The enhanced photoreduction efficiency of metal-added samples can be attributed to the strong Schottky barrier formed at the interface between the noble metals and TiO_2. This barrier effectively trapped electrons and prevented electron-hole recombination. Significantly higher photocatalytic activity was achieved under visible light irradiation compared to UV light, due to a distinct light response mechanism. Firstly, the optical light response of the metal-loaded samples was enhanced and the band gap values were slightly reduced, resulting in increased formation of photogenerated charge carriers. The noble metal nanoparticles deposited on the TiO_2 surface exhibited a SPR effect, enabling absorption of visible light and harvesting a broader range of the solar spectrum. Additionally, noble metal nanoparticles can produce hot electrons with higher kinetic energy. These electrons can be efficiently transferred to the TiO_2 semiconductor, generating additional electron-hole pairs and thus boosting photocatalytic activity[142].

According to studies in the literature, the deposition of Au and Ag nanoparticles enhances the visible-light activity of many semiconductor materials due to the effects of localised SPR and Schottky barrier formation. The LSPR generates an electromagnetic field, and the photoreaction is improved

 doi:10.20944/preprints202604.1590.v1

through scattered photons, plasmonic energy transfer and electron excitation. Au nanoparticles deposited on TiO_2 nanotubes (TNTs) have been used to enhance the photocatalytic reduction of CO_2 to CH_4. In this approach, Au nanoparticles were introduced onto TNTs by a simple electrochemical deposition method. The resulting Au–TNT structures exhibited improved light harvesting under visible irradiation due to the LSPR effect of the Au nanoparticles. Consequently, the photocatalytic activity increased significantly. The TNT and Au-TNT systems exhibited increases in CH_4 production of 8.26% and 14.67%, respectively, compared to bare TiO_2[143].

Producing methane remains challenging due to the slow process of multiple proton-coupled electron transfers and the involvement of various C1 intermediates. A catalyst comprising Ag clusters supported on anatase-phase TiO_2 microspheres, featuring Ag–O hybridisation, was synthesised for the photocatalytic methanation of CO_2. Mechanistic analysis indicated that the Ag clusters enhanced the separation and migration of photogenerated charge carriers and improved CO_2 adsorption. Additionally, Ag–O hybridisation enhanced the multiple proton–electron coupling transfer process by stabilising intermediates and facilitating $^*CO$ hydrogenation to $^*CHO$, leading to selective CO_2 reduction to CH_4. The Ag cluster/TiO_2 sample showed an electron selectivity of 86% for CH_4 production, with a yield of 25.25 μmol g^{-1} h^{-1}[144].

Dendritic porous silica nanospheres (DPSNs) were used as a carrier, featuring large pores arranged in a centre-radial configuration. These DPSNs supported the growth of TiO_2 nanoparticles (NPs) on the surface of the central radial pores. Subsequently, small Au NPs were loaded onto the well-dispersed TiO_2 NPs. By controlling the calcination duration, a series of DPSNs@TiO_2@Au nanocomposites containing Au NPs of different sizes were fabricated. Incorporation of Au, which exhibits the LSPR effect, enabled DPSNs@TiO_2@Au nanocomposites with Au NPs ranging from 3 to 5 nm to demonstrate excellent methane (CH_4) production efficiency, achieving a rate of 34.25 μmol g-TiO_2@Au^{-1} h^{-1}, as well as moderate carbon monoxide (CO) production at a rate of 15.27 μmol g-TiO_2@Au^{-1} h^{-1}[145]. Moreover, these nanocomposites demonstrated robust cycling stability under simulated sunlight using a 300 W Xe lamp. The incorporation of Au NPs reduced the recombination rate of photo-generated electrons (e^-) and holes (h^+) under UV light and also enabled visible light photocatalytic CO_2 reduction through the LSPR effect of Au.

Single-atom CoN_x cluster-decorated TiO_2 (CoN_x/TiO_2) was synthesised in situ by calcining a composite prepared by immersing a MOF (Mil-125) in a cobalt tetra(4-pyridyl)porphyrin (CoPy4) solution. The synthesised CoN_x/TiO_2 exhibited outstanding CO_2 photoreduction activity, with CO and CH_4 yields of 24.4 and 119.9 μmol g^{-1}, respectively, and an overall photoactivity of 1007.6 μmol g^{-1} h^{-1}, which was higher than that of TiO_2 alone and CoO_x/TiO_2. The CoN_x/TiO_2 derived from the CoPy4/Mil-125 composite with a weight ratio of 4:500 showed the optimal component ratio for CO_2 photoreduction. The N_x clusters formed by pyrolysis of H_2Py_4 may enhance the adsorption and activation of reactants (CO_2/H_2O) more effectively than CoO_x in CoO_x/TiO_2, thereby boosting the photoactivity of TiO_2. Moreover, another possible reason is that the CoN_x clusters act as a cocatalyst, significantly enhancing the rapid transfer and separation of photogenerated charge carriers in TiO_2, as well as the adsorption and activation of the reactants (H_2O/CO_2). The results indicated that CoN_x/TiO_2 exhibited minimal photogenerated charge recombination, achieved the fastest charge transfer and had the lowest charge transfer resistance, thus boosting its photocatalytic activity[146].

Ti_3CN MXene was synthesised using a Lewis acidic etching method, avoiding toxic hydrofluoric acid (HF). The Ti_3CN MXene was then used as a support for the in situ hydrothermal growth of TiO_2 and Ru nanoparticles. The improvement in photocatalytic activity was attributed to the constructive interaction between the in-situ growth of TiO_2 on Ti_3CN MXene and the presence of Ru nanoparticles.

In particular, with the addition of only 0.5 wt% Ru, the Ru-Ti_3CN-TiO_2 composite achieved the highest CO (99.58 μmol/g) and CH_4 (8.97 μmol/g) production rates, which were 20.5 and 9.4 times higher than those of P25, respectively[147]. This significant enhancement was attributed to the strong electron-capturing ability of Ru species, which efficiently extracted photogenerated electrons, as shown in Figure 11.

 doi:10.20944/preprints202604.1590.v1

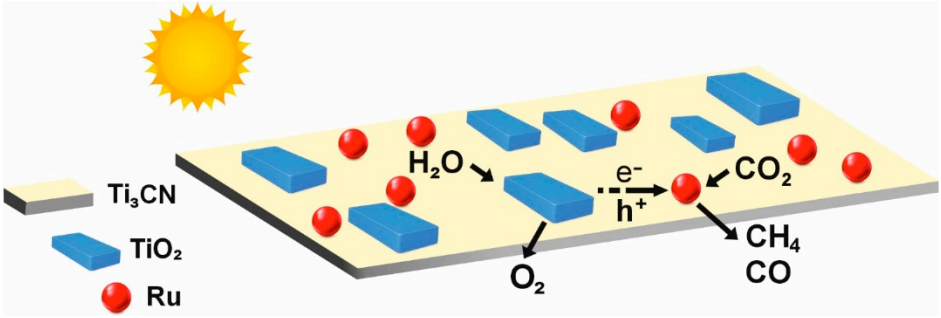

Figure 11. Proposed photocatalytic CO_2 reduction mechanism for Ru-Ti_3CN-TiO_2. Readapted from[147].

A series of CuO_x deposited on TiO_2 photocatalysts with varying TiO_2 nanocrystal supports was synthesised to investigate the impact of CuO_x–TiO_2 interactions on reconstruction and photocatalytic performance in CO_2 reduction using water as the reducing agent. The interaction between CuO_x and TiO_2 was strongest in CuO_x/TiO_2- photocatalysts. Under Xe light irradiation, CuO species supported on TiO_2- 001 were photo-reduced to stable Cu_2O species, which were active in converting CO_2 to CH_4. In contrast, CuO_x species on TiO_2- 100 and TiO_2- 101 were photo-reduced to Cu^0 species, which were less favourable for CH_4 production. The reduction of CuO_x to Cu^0 was more pronounced under Hg light irradiation. In situ Diffuse Reflectance Infrared Spectroscopy (DRIFTS) results showed that CO_2 reduction to CH_4 proceeded via bicarbonate and carboxyl intermediates across all CuO_x/TiO_2 photocatalysts, with additional CO_2^- and formate intermediates observed over CuO_x/TiO_2- 100 and CuO_x/TiO_2- 101 photocatalysts. These findings enhance the fundamental understanding of Cu-based photocatalysts for CO_2 reduction and highlight the importance of the TiO_2 nanocrystal facet effect in TiO_2-related photocatalysis[148].

In another study, the gas-phase photoreduction of CO_2 was investigated using composites of Cu_2O nanoparticles and anodised TiO_2 nanotube arrays. The nanoparticles, with an average size of 90 nm, were pulse-electrodeposited onto vertically aligned hollow TiO_2 nanotubes with an average pore size of 90 nm. Electron spin resonance spectroscopy and radical trapping experiments showed that photoinduced charge separation in the Cu_2O-loaded TiO_2 nanotubes occurred via a direct Z-scheme mechanism. CO_2 photoreduction from a water/CO_2 mixture was monitored in high vacuum using a quadrupole mass analyser, which measured the partial pressures of intermediate and final reaction species in real time under UV-Vis light irradiation (300–600 nm). The main products were formaldehyde and methanol, whereas platinum-loaded TiO_2 nanotubes produced methane and hydrogen. Both specimens formed carbon monoxide (CO)[149].

The use of copper-based semiconductors for CO_2 photoreduction is challenging because these catalysts often exhibit poor stability in aqueous media, due to concurrent oxidation reactions. To address this limitation, the interaction between metallic Cu^0 and TiO_2 has been investigated as a strategy to improve catalyst stability, with TiO_2 serving as both a charge separator and a support for Cu^0 nanoparticles. In this approach, Cu^0 nanoparticles were deposited onto the TiO_2 surface by reducing copper nitrate with a sodium borohydride solution. Given the varying effectiveness of different copper oxidation states in these processes, understanding the oxidation state of copper in the photocatalysts was crucial. Interestingly, a mixture of copper oxidation states has been found to yield better results than a single oxidation state. The addition of copper to the TiO_2 surface enhanced the electron transfer process, thereby increasing the lifespan of these charge carriers, as demonstrated by photoluminescence analysis. As shown in the diffractogram of post-reaction samples, TEM images and XPS spectra, metallic copper, together with Cu^{2+} and Cu^+ species, was present on the TiO_2 surface. Some of the copper dispersed over TiO_2 was oxidised by photogenerated holes (h^+) during CO_2 photoreduction and these oxidised species can be reduced back to Cu^0. Additionally, Cu^{2+} species could capture photoexcited electrons, transforming into Cu^+ species, which could then be oxidised back to Cu^{2+} by oxidising ions and/or O_2 in the system. The coexistence of these different copper species effectively extended the lifetime of photogenerated charge carriers, facilitating electron

 doi:10.20944/preprints202604.1590.v1

transfer to adsorbed CO_2 and thereby enhancing the efficiency of CO_2 photoreduction. The presence of metallic copper resulted in a higher selectivity in CO production (82.32%), while pure TiO_2 was more selective for CH_4 (62.44%)[150].

In another study, supported copper single-atom (Cu-SA) catalysts demonstrated distinctive activity and selectivity in reducing CO_2. The efficiency of the Cu-SA/TiO_2 photocatalyst for CO_2 reduction was evaluated in a gas-solid heterogeneous photocatalytic system using simulated sunlight from a Xe lamp. However, long-term photocatalytic reactions showed that the activity of the Cu-SA/TiO_2 catalyst decreased significantly with prolonged illumination, indicating that the photocatalyst gradually became deactivated during CO_2 photoreduction. The decline in activity of the Cu-SA/TiO_2 photocatalyst for CO_2 reduction was due to the transformation of $Cu^{\delta+}$ to metallic Cu^0 under continuous light exposure. However, it was observed that the Cu-SA/TiO_2 catalyst can maintain stable performance in long-term photocatalytic CO_2 reduction after the introduction of a small amount of O_2 (117.6 ppm) into the reaction system, suggesting that the presence of molecular oxygen helps stabilising the chemical state of $Cu^{\delta+}$ active sites. The total productivity of CH_4 and CO reached 34.64 μmol g_{cat}^{-1} h^{-1} after introducing 117.6 ppm O_2, resulting in enhanced durability[151].

Titania-based ternary composites were synthesised via a two-step process using the Pechini method, followed by impregnation with 3 wt.% CeO_2 and CuO. The N-TiO_2/CuO sample achieved the highest formic acid production, approximately 40 times greater than pure TiO_2, while N-TiO_2/CeO_2/CuO exhibited a sixfold increase in hydrogen evolution. The enhanced performance was attributed to the formation of distinct heterojunctions. For CO_2 photoreduction, the affinity of CuO for CO_2 molecules facilitated the formation of a Z-scheme. Conversely, for hydrogen evolution, the strong affinity of Ti^{3+} for H_2O molecules led to the formation of type II heterojunctions. In both systems, the charge carriers had an extended lifetime, enhancing photoactivity[152].

A composite photocatalysis system was developed using semiconductors enriched with oxygen vacancies and coupled with metallic cocatalysts to enhance charge separation and electron transfer. Mesoporous TiO_2 and titanium-based perovskite oxide ($BaTiO_3$ and $SrTiO_3$) nanoparticle assemblies were synthesised, incorporating abundant oxygen vacancies and copper particles, for the photoreduction of CO_2, as shown in Figure 12[153]. For example, TiO_2 decorated with varying amounts of Cu particles significantly influenced the photocatalytic conversion of CO_2 into CH_4 and CO. In particular, the optimised TiO_2/Cu catalyst exhibited a 13.5-fold increase in CH_4 yield (22.27 μmol g^{-1} h^{-1}) compared to pristine TiO_2 (1.65 μmol g^{-1} h^{-1}). Similarly, $BaTiO_3$/Cu and $SrTiO_3$/Cu composites also exhibited increased CH_4 yields in CO_2 photoreduction compared to their pristine counterparts. Temperature-programmed desorption (TPD) and photoelectrochemical measurements indicated that the co-embedding of Cu particles and abundant oxygen vacancies within titanium-based oxides enhanced CO_2 adsorption capacity, facilitated the separation and transfer of photoinduced electron-hole pairs, and ultimately improved the efficiency of CO_2 photoreduction in TiO_2/Cu, $SrTiO_3$/Cu, and $BaTiO_3$/Cu composites[153].

Co_3O_4/TiO_2 photocatalysts were used to efficiently produce alcohols via CO_2 photoreduction with H_2O under UV or visible light. The presence of Ti^{3+}, Co^{2+}, and Co^{3+} ions reduced the band-gap energy of TiO_2 and decreased the probability of recombination of photogenerated electron-hole pairs. These ions also enhanced the adsorption of CO_2 and CO generated on the photocatalyst surface. This improvement increased the rate of formyl radical formation, which was crucial for alcohol production during CO_2 photoreduction. The highest yield of isopropanol under UV irradiation was observed in the photocatalytic CO_2 reduction with H_2O using 1% Co_3O_4/TiO_2. In contrast, the highest production of propanol occurred when the reaction was photocatalysed by 10% Co_3O_4/TiO_2[154].

 doi:10.20944/preprints202604.1590.v1

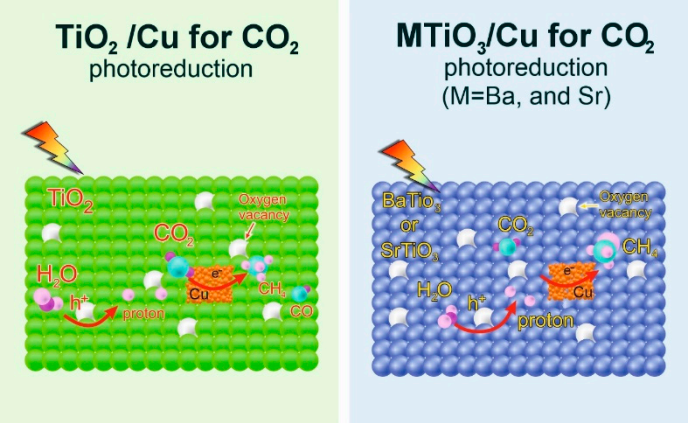

Figure 12. CO_2 photoreduction process on TiO_2/Cu, $BaTiO_3$/Cu, and $SrTiO_3$/Cu samples. Readapted from[153].

Modulating the interfacial structure can significantly influence the photocatalytic performance of supported metal phthalocyanine (MPc) systems. In one method, ZnPc was deposited onto nanosized gold-modified TiO_2 nanosheets (Au–T) to create a broad-spectrum ZnPc/Au–T photocatalyst. Under UV–Vis irradiation, both the ZnPc molecules and the TiO_2 nanosheets were excited simultaneously, enabling cooperative charge transfer processes within the composite system. The photogenerated electrons were transferred from the conduction band of TiO_2 to Au nanoparticles, where they combined with the holes of ZnPc, following a Z-scheme charge separation mechanism. Enhanced by the presence of Au, the holes in TiO_2 facilitated water oxidation, while the photoelectrons activated CO_2 at the Zn(II)-N4 centres. Small Au nanoparticles with a diameter of about 3 nm were successfully introduced between ZnPc and TiO_2 nanosheets to create ZnPc/Au-T heterojunctions[155]. For photocatalytic CO_2 reduction, the optimised 2.5ZnPc/1Au-T exhibited a threefold and tenfold increase in photoactivity compared to 2.5ZnPc/T and pristine TiO_2, respectively, producing CO and CH_4 as the main products. Small Au nanoparticles were more effective than larger ones (8 nm) in facilitating Z-scheme charge transfer from TiO_2 to ZnPc, as confirmed by various characterisations. Furthermore, the interaction between Au nanoparticles and the aromatic ring of ZnPc, evidenced by FTIR and XPS, resulted in improved dispersion of ZnPc assemblies, enhancing visible-light absorption and greater exposure of Zn-N_4 catalytic sites. The same design strategy can also be applied to other transition metals, such as Ni, Co and Fe[155].

The effect of the basic properties of MgO on the photoactivity of MgO/TiO_2 nanocomposites in the CO_2 reduction reaction, as well as the photocatalytic efficiency of pure TiO_2 and TiO_2/MgO nanocomposites, was evaluated in both water and 0.1 M NaOH solution. Methane production from CO_2 photoreduction was higher in NaOH solution than in water, owing to CO_2 greater solubility of CO_2 in NaOH solution compared to pure water. MgO enhanced the adsorption of acidic CO_2 molecules due to its basic character. Meanwhile, water molecules in the reaction medium were oxidised in the valence band of TiO_2 (H_2O/O_2, +0.82 V). The nanocomposite containing 1% MgO produced more CH_4 than the other samples analysed. It is hypothesised that CO_2 adsorbs onto the MgO layer on the TiO_2 surface, forming metastable magnesium carbonate species. However, when the MgO content was increased (in TiO_2/MgO 2% and 5%), the catalytic efficiency decreased. This suggests that the insulating effect of MgO particles became dominant. With higher MgO amounts, the TiO_2 surface may be completely covered, hindering the migration of photogenerated charge carriers on the TiO_2 surface and thus reducing activity[83].

The impact of three distinct substrates titanium, indium and tin oxide coated on polyethylene terephthalate (ITO-PET), and PET on charge transfer and activity in the photocatalytic CO_2 reduction using two noble-metal free catalysts was investigated through density functional theory (DFT), optical analyses and photo-electrochemical tests. The CO_2 reduction activity was significantly higher for catalysts placed on the Ti sheet compared to the other substrates. The density of states (DOS) for catalysts on the Ti substrate showed an intense energy state in the middle of the catalyst band gap,

 doi:10.20944/preprints202604.1590.v1

facilitating more efficient energy transfer of plasmons from the substrate to the catalyst conduction band. Additionally, the energy levels at which electron-hole recombination occurs vary with the substrate, affecting CO_2 reduction activity, as shown by the results for amorphous TiO_2 modified with SiO_2[156].

The photocatalytic performance of a Cu–Rh/TiO_2 system has been investigated under both ultraviolet and visible light irradiation. In this method, a coarse layer of TiO_2 was deposited onto a metal grid by electrophoretic deposition. Metals were then sequentially evaporated under vacuum thermal conditions, followed by heat treatment at the low temperature of 350 °C. This process enabled the formation of a Cu–Rh nanoalloy, resulting in a single-phase solid solution with controlled composition and well-defined lattice parameters. Interestingly, this outcome contrasted with the phase equilibrium diagram of the bulk Cu-Rh system, which predicted decomposition into two solid solutions enriched in Cu and Rh, respectively, at temperatures below 1150 °C. This result was interpreted as evidence of a size effect typical in such systems, where reducing particle size lowers the phase transition temperatures. Cu-Rh alloys with compositions of 25/75, 50/50 and 75/25 at% were synthesised and deposited on a TiO_2 layer electrophoretically coated onto a stainless-steel grid, with an average thickness not exceeding 10 nm[157]. It was found that varying the composition of the Cu-Rh alloy in combination with TiO_2 enabled control of the photocatalytic process. Under UV irradiation, the sample with a 75/25 at% ratio of Cu-Rh exhibited the highest activity in generating acetaldehyde, while the 50/50 at% sample produced the most methanol. In the visible light range, the highest acetaldehyde production was observed with the Cu-Rh alloy at 25/75 at%. Furthermore, surface modification of TiO_2 with nano-islands increased acetaldehyde formation activity in the visible range[157].

A self-improving photocatalyst, TiO_2@BiOCl, was developed by growing ultra-thin BiOCl layers on the imperfect surface of TiO_2 nanotubes. The nanocomposites exhibited exceptional photocatalytic performance in CO_2 reduction, achieving a peak CH_4 production rate of 168.5 μmol g^{-1} h^{-1} with a CH_4 selectivity of 99.4%. The high surface area provided ample sites for CO_2 adsorption and reduction. Additionally, the ultrathin heterostructure minimised the distance for charge transport from the bulk to the surface, enhancing charge carrier separation across interfaces and increasing the availability of electrons for photoreduction. Under UV–Vis irradiation, oxygen vacancies on TiO_2 effectively captured electrons generated by TiO_2, while Bi^0 atoms directed electrons from BiOCl towards these vacancies, efficiently gathering electrons to enhance productivity[158]. During CO_2 photoreduction, hydrogen-incorporated oxygen vacancies significantly suppressed H_2 generation and promoted rapid hydrogenation of CO_2. Furthermore, catalytic sites formed by Bi and Ti metals surrounding oxygen vacancies inhibited CO production, further enhancing selective CH_4 productivity through enhanced hydrogenation pathways[158].

A 10 wt% nickel co-catalyst was applied to 3D spherical TiO_2 microparticles (MPs) and 1D wire-like TiO_2 nanowires (NWs) for CO_2 hydrogenation to renewable fuels under visible light. Initial experiments showed that CO_2 hydrogenation did not occur below 250 °C, even with visible light irradiation. At 250 °C, the production of CH_4 and CO increased 3.69-fold with visible light. However, this effect diminished at higher temperatures, indicating that the photothermal effect of visible light was more significant at lower temperatures. The 1D 10Ni/TiO_2 NWs demonstrated superior performance in photothermal methanation, achieving a CH_4 and CO production rate of approximately 19.8 mmol g_{cat}^{-1} h^{-1}, which was 1.5 times higher than that of the 3D spherical TiO_2 catalyst. This enhancement was due to the one-dimensional wire-like structure, which increased the catalyst's surface area and porosity, improving CO_2 adsorption. Additionally, the improved dispersion of nickel on the one-dimensional structure prevented the growth of NiO nanoparticles, facilitating the adsorption and dissociation of H_2 gas into hydrogen atoms. Remarkably, the 10Ni/TiO_2 NWs catalyst showed extended durability over four cycles, with performance gradually improving in each cycle. This improvement was attributed to the continued reduction of NiO to metallic Ni by excess unreacted H_2 gas. Visible light irradiation also facilitated this reduction, generating more active Ni sites as the reaction progressed[159].

 doi:10.20944/preprints202604.1590.v1

A binary component catalyst consisting of single atoms (Pt and Au) supported on self-doped TiO_2 nanotubes was evaluated for CO_2 photoreduction. The results showed that covalent interactions enabled effective transfer of photogenerated electrons from defect sites to the single atoms, while also enhancing electron–hole separation and overall charge transfer efficiency. The maximum photocatalytic performance of Pt-Au/R-TNTs with 0.33 wt% single atom metals was recorded as 149 times that of unmodified R-TNT, with CH_4 and C_2H_6 yields increased to 360.0 and 28.8 μmol g^{-1} h^{-1}, respectively[160].

Examples of various metal-doped TiO_2-based photocatalysts are provided in Table 7, including the associated experimental conditions and CO_2 photoreduction activity. The yield of CO_2-converted products is strongly related to the choice of metal, reductant, photoreactor, light source and intensity, as well as product selectivity.

The selection of appropriate metal cocatalysts, combined with the surface basicity of TiO_2, has been identified as a key strategy to enhance photocatalytic CO_2 reduction efficiency. Uniform, ligand-free metal nanoparticles of Ag, Cu, Pd, and Pt loaded on TiO_2 surfaces were investigated for the photoreduction of CO_2 using water as the reductant. According to the reported results, Ag was the most active for CO production, while Pd and Pt primarily generated hydrocarbons such as methane and ethane. Furthermore, amine-modified TiO_2 provided a 2.4-fold enhancement in CO_2 photoreduction activity compared with bare TiO_2[161].

Table 7. Summary of recent results for photocatalytic CO_2 reductions using metal doping or metal co-catalysts.

Photocatalyst	Reactants	Reactor	Radiation	Product	Yield (μmol g^{-1} h^{-1})
Pt–Ru/TiO_2	CO_2 + H_2O	Gas-closed circulation system	Xe lamp (320–780 nm)	CH_4	38.7
Fe/TiO_2	CO_2 + H_2	Continuous flow quartz	Hg lamp (252 nm)	CH_4	166
Ag/TiO_2	CO_2 + H_2O	Continuous flow reactor	Xe lamp (365 nm)	CH_4, C_2H_6, C_2H_4, C_2H_5OH	0.42, 0.10, 0.12, 1.9
Ni–Bi/TiO_2, Cu/Cu_2+/TiO_2	CO_2 + Na_2SO_4	Batch photo-reactor, Quartz	Hg lamp (350 nm) Xe lamp (350 nm)	CH_4, CH_4, CO	2.4, 21.1, 7.8
Ag/TiO_2, Pt–Au/R–TNTs	$NaHCO_3$ + H_2O	Cell, Photochemical reactor, Quartz cell	Hg lamp (350 nm) LED light (365 nm)	CO, CH_4, C_2H_6	1.9, 11.9, 28.8
Pd/TiO_2–N	CO_2 + $NaHCO_3$	Quartz cell	Hg lamp (320–390 nm)	CH_4	360.0
Pt/TiO_2–N, Au/TiO_2(Ar)	CO_2 + H_2O	Continuous flow reactor	LED light (365–530 nm)	C_2H_6, CO	8.3, 3.9
Ru–TiO_{2-x}	$NaHCO_3$ + H_2O vapor	Glass Reactor	Xe lamp (320 nm)	CH_4, C_2H_6, CH_4	0.87, 31.6

Recently, the performance of CO_2 photoreduction to CH_4 over Ru supported on partially reduced TiO_2 (1% Ru–TiO_{2-x}) was investigated, showing a significant increase in photocatalytic activity compared with both Ru–TiO_2 and TiO_{2-x}, with a CH_4 yield of 31.6 μmol g^{-1} h^{-1}[1162].

TiO_2 was modified with Au, Ag, Pd and Pt to produce monometallic and bimetallic samples. Diffuse reflectance Spectroscopy showed significant differences in light-harvesting capacity between bare TiO_2 and the metal-loaded samples. A lower band gap in the photocatalyst corresponded to

 doi:10.20944/preprints202604.1590.v1

higher photocatalytic efficiency. All these metals are also capable of SPR (Figure 13), especially gold, which has a plasmonic band visible at 560 nm, and silver, with a lower intensity around 460 nm. Platinum behaves similarly to silver, although its SPR bands are usually found at lower wavelengths, depending on the size of the nanoparticles[59, 67].

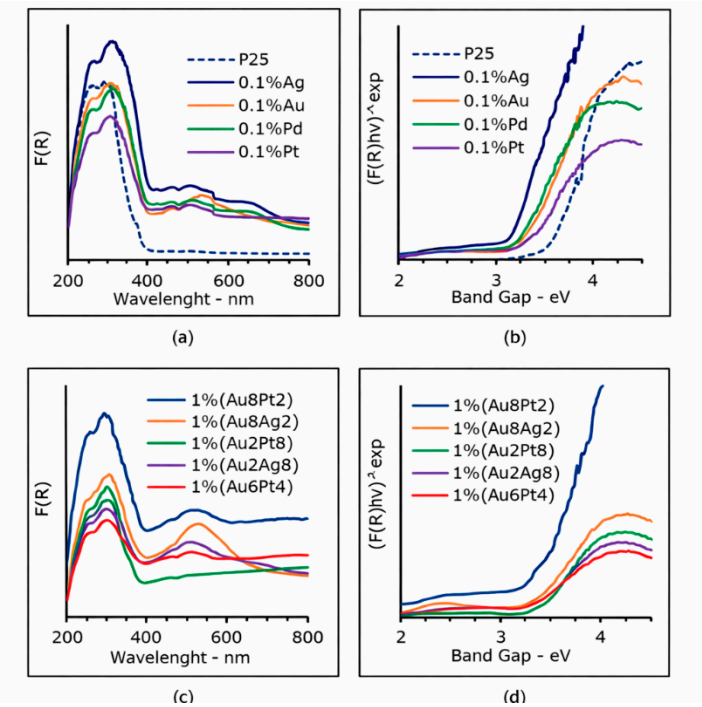

Figure 13. UV-Vis diffuse reflectance spectra (DRS): (a) monometallic and (b) bimetallic titania-based photocatalysts, together with the corresponding Kubelka–Munk transformations (r = ½) plotted as a function of band gap energy in (c) and (d). The step observed at 565 nm is attributed to instrumental effects. Reproduced from [59] under the Creative Commons Licence.

Pt@Bi–TiO_2 photocatalysts were synthesised using a two-step method involving Bi doping via sol–gel and Pt deposition via photodeposition for CO_2 photoreduction. The reaction was conducted in a batch gas–solid photoreactor under UV irradiation, where pure TiO_2 produced CO with only minor amounts of CH_4. According to various published studies, introducing Pt into TiO_2 causes CH_4 to become the major product. This shift in selectivity is due to the redox potential of CO_2, as CH_4, the most reduced single-carbon product, requires eight electrons and therefore has a less negative potential. Pt nanoparticles act as electron traps with a reduction potential less negative than that of the conduction band of TiO_2, facilitating the reduction of CO_2 to CH_4. Therefore, TiO_2 produced methane with a yield of 3.3 μmol g^{-1} after 10 hours of reaction, while this value reached 20.6 μmol g^{-1} for 3 wt% Bi and 1.5 wt% Pt (1.5Pt@3Bi-T). When the photo-deposition method was used to introduce Pt onto TiO_2, Pt nanoparticles tended to locate on specific surface sites of TiO_2 where photo-generated electrons could more easily reach them. Thus, Pt nanoparticles did not disperse randomly but instead concentrated on sites that facilitate more efficient extraction of electrons from the conduction band of TiO_2. Moreover, the introduction of basic Bi onto the surface of TiO_2 enhanced the chemisorption of CO_2, a vital initial step in CO_2 photoreduction. X-ray diffraction patterns indicated the presence of $Bi_2Ti_2O_7$, which was uniformly dispersed in the Bi-modified samples. This phase assisted in stabilising CO_2 by forming carbonate species, as shown in Figure 15[163].

Both theoretical and experimental studies indicate that when an element with an oxidation state lower than that of the host elements (which is +4 for Ti^{4+} in TiO_2) is doped into TiO_2, it tends to create oxygen vacancies to balance the lower electrical charge. An oxygen vacancy can be filled by one of the two CO_2 oxygens, which alleviates cleavage of the C=O bond[163].

Preprints.org (www.preprints.org) | NOT PEER-REVIEWED | Posted: 22 April 2026 doi:10.20944/preprints202604.1590.v1

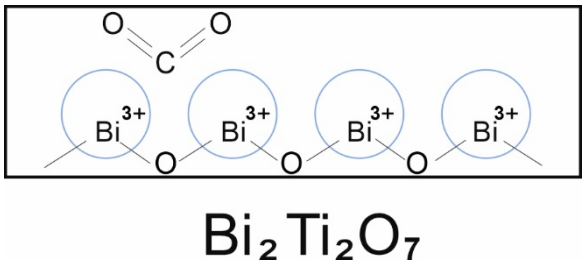

Figure 15. CO_2 photo-reduction mechanism on 1.5Pt@3Bi-T. Readapted from[163].

TiO_2 nanostructures doped with various concentrations of Fe were synthesised using the sol-gel process, followed by annealing at 470°C. Doping with 2 wt% Fe resulted in the highest rates of CO_2 photoreduction, producing approximately 0.35 μmol g^{-1} min^{-1} of CO and 0.67 μmol g^{-1} min^{-1} of CH_4, both higher than those of pristine TiO_2. UV irradiation generated intrinsic electrons in the conduction band and holes in the valence band of the Fe-doped TiO_2 nanostructures, while additional electrons were supplied by donor defects such as oxygen vacancies and interstitial titanium. Moreover, V_O-related defects on the surface of Fe-doped TiO_2 contributed additional electrons, resulting in more electrons and holes than in pristine TiO_2. The prolonged charge-carrier lifetimes were attributed to the formation of Fe^{3+}/Fe^{2+} and Fe^{3+}/Fe^{4+} levels on the surface. The optical band gaps in Fe-doped samples decreased due to the introduction of defect levels within the TiO_2 forbidden band gap, as shown in Figure 16[164].

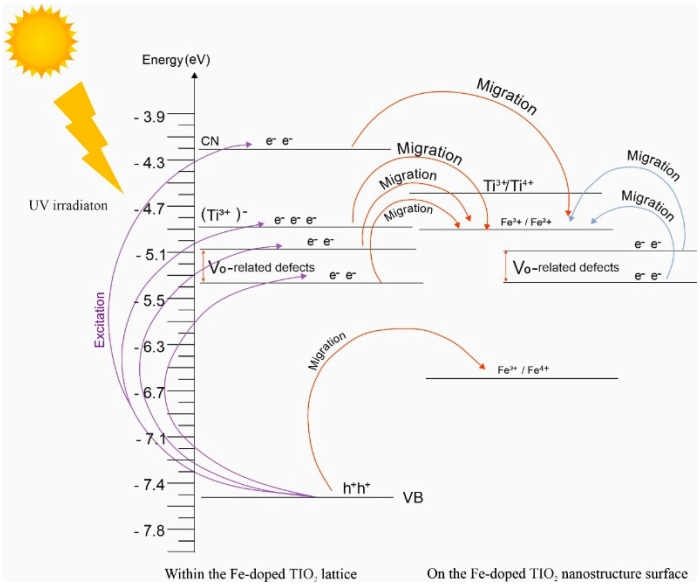

Figure 16. Proposed band gap diagram and pathway of charged carriers under UV irradiation. Readapted from[164].

Cu_xO-doped TiO_2 catalysts were prepared and used for CO_2 photoreduction to produce CH_4 in a two-dimensional flow reactor, where the gas stream passes over a thin catalyst layer under UV light. Analysis of the photocatalysts indicates that the oxidation state of Cu changes during the reaction, altering the catalyst's physicochemical properties. Core-level and valence-band spectroscopies were used to construct a band diagram for the most effective catalyst, revealing a Z-scheme structure[165]. Moreover, selecting an appropriate hole scavenger, such as ethanol, and optimising its concentration increased CH_4 production rates to 117 μmol CH_4 g_{cat}^{-1} h^{-1} under low-power LED irradiation. Another study reported the use of sacrificial agents in photocatalysis and examined the role of ethanol in the photoreduction of CO_2 to CH_4 using Cu-P25 photocatalysts in a flow reactor. Increasing the ethanol concentration resulted in higher CH_4 production, achieving a

 doi:10.20944/preprints202604.1590.v1

yield of 235 μmol CH_4 g_{cat}^{-1} h^{-1} with an ethanol flow rate of 0.25 μmol min^{-1} in the gas stream, highlighting the crucial role of the sacrificial agent in the reaction[72].

A mesoporous photocatalyst for CO_2 photoreduction was developed and optimised by integrating TiO_2 with a mesoporous carbon (CMK-3) template, followed by removal of the template. A detailed investigation of silver doping strategies using photodeposition and synchronous doping techniques was also conducted. By examining the effects of acid/base behaviour and charge-carrier recombination rates on CO_2 photoreduction performance and product selectivity, it was found that the impact on CO_2 photoreduction followed the order: Lewis acid sites > Lewis basic sites > charge-carrier recombination rates. The proposed mechanism indicates that Lewis acid sites govern H^+ production and regulate the rates and selectivity of CO and CH_4 production, as shown in Figure 17. Furthermore, the irradiation-induced Lewis acid/base behaviour of the photocatalyst was demonstrated by NH_3/CO_2 temperature-programmed desorption. The most promising catalyst achieved 96% CH_4 selectivity and an eleven-fold higher yield compared to commercial TiO_2 P25[166].

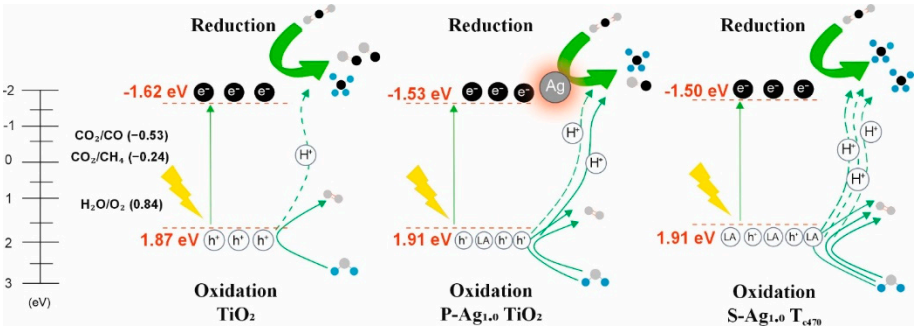

Figure 17. Schematic illustration of the proposed mechanism of Ag-doping on the CO_2 photoreduction. Readapted from[166].

A Ce-doped TiO_2 aerogel with oxygen vacancies anchored on chitosan-derived oriented carbonaceous structures (Ce–TiO_2@CS) was synthesised using the sol–gel method combined with freeze casting, supercritical drying and heat treatment. The CH_4 and CO yields were 9.45 μmol g^{-1} h^{-1} and 42.26 μmol g^{-1} h^{-1}, respectively. Ce-doping in pristine TiO_2 introduced impurity levels within the band gap, effectively extending the light response range into the visible region. In addition, the rapid recombination of electrons and holes was mitigated by the two-phase microstructures, while the swift electron transfer rate was facilitated within the oriented porous carbon framework. Through doping, Ce^{3+} replaced Ti^{4+} in the TiO_2 lattice, generating oxygen vacancies. This modification enhanced the utilisation of photo-induced electrons for CO_2 conversion and simultaneously formed basic sites. The carbonaceous (CS) aerogel acted as a carrier, enhancing light absorption and facilitating charge carrier transfer, while the Ce-doped TiO_2 (Ce-TiO_2) aerogel served as the active site for CO_2 photoreduction[167].

Noble metals such as Pt and Au, as well as transition metals including Ni-doped nanoflakes, were investigated when assembled on TiO_2@carbon microrods with a high specific surface area and rutile crystal structure, synthesised via a solvothermal method. The Pt-doped catalyst showed improved hydrogen production efficiency and increased CH_4 selectivity, while the Ni-doped catalyst exhibited significant CO_2 reduction activity. Both Ni and Au promoted higher selectivity towards CO. The results showed that significant differences in activity among the tested catalysts ranked in the following descending order: Ni-TiO_2@C > Au-TiO_2@C ≈ TiO_2@C > Pt-TiO_2@C. One possible reason for the superior activity of the Ni catalyst compared to Pt and Au was its lower activation energy for CO_2 dissociation. Additionally, XPS results indicated that Ni existed in both metallic Ni and NiO states. The presence of Ni in higher valence states reduced the CO binding energy, increased the activation barrier for concurrent hydrogenation of CO, and promoted CO production. Based on the amounts of CO and CH_4 produced, the Ni-doped catalyst achieved the highest CO yield with a selectivity of 88%, while the Pt catalyst showed the highest CH_4 yield with a selectivity of 41%. The

 doi:10.20944/preprints202604.1590.v1

metal-free TiO_2@C catalyst exhibited 100% CO selectivity. The increased selectivity of Pt towards CH_4 was attributed to the prolonged photoinduced electron lifetime facilitated by the Schottky junction formed at the Pt–TiO_2 interface, as well as higher efficiency in charge separation, which led to greater electron efficiency. Moreover, Ni surfaces, being highly oxophilic, enhanced CO_2 dissociation, while Pt surfaces, which were less oxophilic, promoted CH_4 formation[11].

A strategy was proposed for fabricating reduced graphene oxide (rGO)-wrapped Ag/TiO_2 nanofibres. Coaxial electrospinning with a negative electric potential was used to align rGO along the direction of the electric field while to facilitate the electrohydrodynamic transport of Ag^+ ions to the surface of the fibres. This process resulted in the fabrication of rGO-wrapped Ag/TiO_2 nanofibres (NFs) with a well-concentrated and uniformly distributed Ag layer between the rGO and TiO_2 after thermal treatment. This surface-concentrated Ag layer enhancing the transport and collection of photogenerated electrons during CO_2 reduction and improved light harvesting efficiency by extending the response from UV to visible light. By adjusting the rGO content during electrospinning, a thin (1–2 nm) rGO monolayer was successfully wrapped around the Ag/TiO_2 NFs without blocking light. This rGO layer provided an additional pathway for interfacial charge transfer between Ag, TiO_2, and rGO, thereby enhancing charge separation and electron enrichment in the ternary nanocomposite (rGO/Ag/TiO_2) for CO_2 conversion. As a result, the rGO/Ag/TiO_2 nanofibres demonstrated superior CO_2-to-CH_4 photoreduction performance under visible light, with a CH_4 yield more than 25 times higher than that of bare TiO_2 nanofibres without Ag and rGO. Furthermore, the complete wrapping of rGO around the entire fibre structure improved the structural stability of the ternary nanocomposite. This stability enabled the rGO/Ag/TiO_2 nanofibres to maintain high CO_2-to-CH_4 photoreduction efficiency consistently over six repeated testing cycles (17 hours)[168].

Mixing TiO_2 with Mo_2C has recently been proposed to enhance the photocatalytic conversion of CO_2 to methanol under visible light, although further work is required to improve process performance. In this context, employing p-type semiconductors such as Cu_2O through co-doping strategies can improve charge redistribution owing to its narrower bandgap, as well as increase reaction selectivity towards methanol. A continuous visible light-driven CO_2 photoconversion process to methanol was developed in an optofluidic microreactor using Cu_2O/Mo_2C/TiO_2 heterostructures. Notably, the production of CH_3OH per gram of photocatalyst per unit time was significantly enhanced by incorporating Cu_2O into the heterostructures. This demonstrated the positive synergistic properties of the investigated photocatalytic structures, where improved visible light absorption, enhanced photoexcitation delocalisation, and reduced recombination rates of photogenerated charges contributed to increased CO_2 photoreduction selectivity towards CH_3OH. The Cu_2O/Mo_2C/TiO_2 materials exhibited a narrower optical bandgap, enabling better absorption of solar energy in the visible range and more efficient excitation of electrons from the valence band to the conduction band. This superior photocatalytic performance was likely due to improved separation and transfer of photogenerated charge carriers in the heterostructures[89].

An electrochemical method was developed to create a series of POM@TiO_2 hybrid catalysts by loading individual polyoxometalate (POM) clusters onto anatase TiO_2 nanotubes. The high electron-accepting and storage capacities of POMs improved the separation of photogenerated electrons and holes in these hybrid catalysts, resulting in efficient CO_2 photoreduction and water oxidation. Systematic testing showed that adjusting the redox properties and electron-accepting capabilities of POMs significantly influenced the concentration of photogenerated holes reaching the surface in the POM@TiO_2 composites, thereby enhancing water oxidation and promoting CO_2 reduction. Various characterisations revealed that P_2Mo_{18} exhibited the best electron acceptance and storage abilities. Consequently, P_2Mo_{18}@TiO_2-1 (where 1 represents the POM concentration, mM) significantly improved CO_2 photoreduction activity, achieving an electron consumption rate of 1.26 mmol g^{-1} for CO_2-to-CH_3OH conversion, which was 11 times higher than that of pure TiO_2 nanotube arrays[169].

The effect of different metals (Cu, Ag, Au) on enhancing the photocatalytic reduction of CO_2 by TiO_2 was investigated. Incorporation of these metals improved light absorption and reduced charge recombination, with the charge carrier lifetime increasing from 0.21 ns to approximately 1.2 ns, thus

 doi:10.20944/preprints202604.1590.v1

enhancing overall photocatalytic efficiency. Among the metals studied, Au showed the highest electron selectivity for H_2 (>97%), while Ag and Cu showed greater selectivity for CO_2 reduction (~20% for Cu). The study highlighted the critical role of intermediate stabilisation in determining reaction pathways and final products[170]. For example, Ag and Cu facilitated different pathways, including the carbene and formaldehyde routes, respectively, leading to distinct final products. To increase CO selectivity, it was essential to design the catalyst surface to favour weak CO adsorption. CO-TPD measurements showed that Ag sites effectively stabilised weakly adsorbed CO^*, resulting in higher CO selectivity compared to Cu. Meanwhile, Cu's higher CH_3OH formation rates were attributed to improved stabilisation of reactive M=O species, which promoted the conversion of CH_4 to CH_3OH. Cu also stabilised CH_3O^* intermediates more effectively, enhancing methanol production via the formaldehyde route. In contrast, Ag's stabilisation of CH_2^* indicated a greater tendency for the carbene pathway, leading to CH_4 as the final product[170].

A controlled synthesis of Cu-doped TiO_2 with varying exposed facets was demonstrated to selectively photocatalyse the reduction of CO_2 to CH_4 using a topological transformation from MIL-125 (Ti) precursors. Notably, the optimal Cu/TiO_2 (001) catalyst, with its round, cake-like structure, showed high photocatalytic activity for CO_2 reduction, achieving a CH_4 yield of 40.36 μmol g^{-1} h^{-1} and a selectivity of 94.1%. These values were significantly higher than those for TiO_2 (001) (4.7 μmol g^{-1} h^{-1} and 52.6% selectivity), Cu/TiO_2 (101) (14.73 μmol g^{-1} h^{-1} and 78.9% selectivity) and Cu/TiO_2 (001 + 101) (18.95 μmol g^{-1} h^{-1} and 69.6% selectivity). Both experimental and theoretical analyses showed that the (001) facet of the Cu/TiO_2 photocatalyst enhanced CO_2 adsorption and activation, while Cu ion doping improved the efficiency of photogenerated charge separation and transfer. This study highlighted the importance of combining facet engineering with ion doping to develop high-performance photocatalysts for the selective reduction of CO_2 into multi-electron products[171].

5.2. Modification of g-C_3N_4-based catalysts

Recently, the development and application of composites comprising noble and non-noble metal nanoparticles with g-C_3N_4 has become a significant research focus in the field of g-C_3N_4. An ion-loading pyrolysis method was used to in situ anchor Pd single atoms and twinned Pd nanoparticles onto ultra-thin graphitic carbon nitride nanosheets (PdTP/PdSA-CN) for highly efficient photoreduction of CO_2. The electronegative nitrogen sites in g-C_3N_4 connected Pd single atoms (SAs) and Pd-twinned particles (TPs), forming Pd–N bonds with strong electronic metal-support interactions (EMSI) and enabling directional electron transfer from Pd-TPs to Pd-SA sites[172]. The optimised PdTP/PdSA-CN demonstrated significantly improved photocatalytic activity for CO_2-to-CO conversion compared with bare g-C_3N_4, PdSA-CN and PdTP-CN, achieving a CO evolution rate of up to 46.5 μmol g^{-1} with complete selectivity. The Pd-TPs acted as electron donors, increasing electron density at the catalytic centres of single-Pd sites via the N ligands in the g-C_3N_4 networks. This downshifted the d-band centre, facilitating carbonyl desorption for CO production. Furthermore, the incorporation of Pd-TPs improved light absorption and promoted charge transport and separation[172].

A dual-site single-atom catalyst was developed by incorporating adjacent Sn(II) and Cu(I) centres into a C_3N_4 framework. This configuration resulted in a significant enhancement in HCHO production, driven by a four-electron transfer mechanism proceeding via the $^*OCHO$ intermediate. While the Sn-based sites alone favoured HCOOH formation, the introduction of isolated Cu sites enabled an alternative reaction pathway, promoting the selective generation of HCHO. Under optimised conditions, with a Sn precursor mass ratio of 3:1, the system achieved a maximum HCHO productivity of 259.1 μmol g^{-1} and a selectivity of 61% in 24h. This selectivity for HCHO was significantly higher than that of other metal-embedded C_3N_4 photocatalysts. The generation of HCHO was believed to occur via the two-electron reduction of HCOOH, as supported by the in-situ FTIR peak at 1637 cm^{-1}, which was attributed to $^*HCHO$ intermediates adsorbed at the dual-atom Sn–Cu sites. This study provided new insights into multi-electron transfer mechanisms in dual-atom

 doi:10.20944/preprints202604.1590.v1

catalytic systems, where specific intermediates were selectively stabilised through the synergistic action of heteronuclear dual-atom sites[173].

The g-C_3N_4/$Bi_{19}Br_3S_{27}$ S-scheme heterostructure was synthesised by in situ deposition of $Bi_{19}Br_3S_{27}$ onto porous g-C_3N_4 nanosheets. Density functional theory (DFT) simulations revealed distinct Fermi levels for BBS and P-CN, leading to the formation of a built-in electric field at their interface. This field served as a crucial driving force for carrier migration, facilitating the transfer of electrons from the CB of P-CN to the VB of BBS via the S-scheme mechanism. Additionally, the CS bond served as an efficient charge transport channel between the BBS and P-CN interface, significantly reducing the charge-transfer energy barrier across the interfaces and further enhancing the charge-transfer process in the S-scheme. These strategies collectively contributed to the improved photocatalytic CO_2 reduction activity of the BBS/P-CN heterojunction. Notably, under visible-light irradiation (420 nm), the optimised BBS/P-CN heterojunction achieved a CO evolution rate of 32.78 μmol g^{-1} h^{-1}. Furthermore, the BBS/P-CN heterojunction demonstrated excellent cycling stability, maintaining over 90% of its activity after 25 hours across five cycles[174].

Single-atom Ni on g-C_3N_4 was fabricated using a high-energy ball milling method. The photocatalyst containing 0.32 wt% single-atom Ni achieved the highest CO_2 reduction rate of 19.9 μmol g^{-1} h^{-1}, even without a sacrificial agent. The well-dispersed single-atom Ni active sites on the substrate surface enhanced the cleavage of π-bonds in the C=O group, lowered the Gibbs free energy for CO_2 adsorption on CN, and facilitated the spontaneous adsorption and activation of CO_2. The photo-excited electrons were efficiently transferred through the conduction band of CN to the uniformly distributed single-atom active sites, while the photo-excited holes remained in the valence band of CN to react with H_2O, generating O_2 and H^+. This uniform distribution of single-atom Ni on CN significantly reduced the overall activation energy barrier by optimising the reaction pathway, resulting in more efficient photocatalytic conversion of CO_2 to CO. Consequently, the catalytic activity was more effective than that of other CN-based photocatalysts[175].

A two-step photoinduced process was used to fabricate an AuCu/PANI/g-C_3N_4 heterostructure photocatalyst, in which a polyaniline (PANI) conducting layer and an AuCu alloy cocatalyst were sequentially deposited onto graphitic carbon nitride (g-C_3N_4) nanoflakes. Under simulated sunlight, the CO production rate of the AuCu/PANI/g-C_3N_4 photocatalyst was 1.3 times greater than that of AuCu/g-C_3N_4, 2.3 times greater than that of PANI/g-C_3N_4, and 5.4 times greater than that of pure g-C_3N_4. The enhanced photocatalytic performance of AuCu/PANI/g-C_3N_4 was attributed to several factors. First, the PANI layer improved CO_2 adsorption and electron transfer. Second, AuCu nanoparticles increased light absorption and accelerated charge separation. Finally, the AuCu cocatalyst provided efficient active sites for CO_2 conversion. Furthermore, the AuCu/PANI/g-C_3N_4 photocatalyst exhibited stable performance during extended photocatalytic CO_2 reduction tests[176].

A method for preparing g-C_3N_4/ZnO nanocomposites is proposed in[177], based on refluxing a zinc salt solution in methanol with pre-formed g-C_3N_4, using KOH in methanol as the precipitating agent. Ultrafine ZnO nanoparticles were in-situ grown and decorated on ultrathin g-C_3N_4 layers, forming a well-defined interface. This arrangement not only facilitated efficient charge transfer and separation but also increased the number of active sites available for CO_2 adsorption and activation. The hybridization of ultrathin g-C_3N_4 layers with ZnO nanoparticles enhanced the chemisorption capacity of CO_2/H_2O, which was crucial for the photocatalytic CO_2 reduction process. In the CZ-40 composite, the proton-coupled electron transfer (PCET) process for CO_2 photoreduction was enhanced, resulting in higher selectivity for CH_4 production and an overall increase in photocatalytic activity for CO_2 reduction. In contrast, single g-C_3N_4 showed lower H_2O chemisorption than the composite, leading to higher selectivity for CO production. However, its lower CO_2 chemisorption resulted in significantly reduced overall photocatalytic activity for CO_2 reduction. Additionally, the ultrathin g-C_3N_4 layers may affect H_2O and CO_2 adsorption behaviours differently. H_2O molecules on the solid surface can enhance the mass transfer of CO_2 from the gas phase to the solid surface, thereby increasing CO_2 adsorption. This improvement supports the acceptance of photogenerated electrons for CO_2 reduction via the PCET process.

 doi:10.20944/preprints202604.1590.v1

In another study, ultrasmall subnanometre Ni- and Mn-oxo clusters (with an average diameter of 0.8 nm) were uniformly anchored on customised chitosan oligomer functionalised ultrathin g-C_3N_4 nanosheets, using OH and NH_2 groups in chitosan as coordination sites. The optimised Ni and Mn co-modified photocatalyst, developed by adjusting the metallic molar ratio, showed a remarkable 22-fold increase in CO_2 conversion rate under solar irradiation and a 20-fold increase in quantum efficiency at 405 nm compared to pristine g-C_3N_4. Under solar irradiation, photogenerated electrons and holes excited from carbon nitride are captured by the Ni- and Mn-oxo clusters anchored by the pre-modified chitosan molecules. The Ni-oxo species enhance the catalytic function for CO_2 reduction, while the Mn-oxo species facilitate H_2O oxidation. Consequently, the synergistic effects of the Ni- and Mn-oxo clusters result in dual modulation of charge carriers, significantly improving charge separation and enhancing photoactivity for CO_2 reduction reactions[178].

Copper/zinc oxide/graphite nitrogen carbide (Cu/ZnO/g-C_3N_4) was synthesised using a hydrothermal method. The 3 wt% Cu/ZnO/g-C_3N_4 photocatalyst showed significant production rates of CH_4 (40.7 μmol g^{-1} h^{-1}), CO (65.1 μmol g^{-1} h^{-1}) and CH_3OH (92.5 μmol g^{-1} h^{-1}), which were 38.3, 77.1 and 58.1 times higher, respectively, than those of pure g-C_3N_4. Under UV and visible light, Cu/ZnO/g-C_3N_4 was continuously excited, generating electron-hole pairs. The electrons in the CB of g-C_3N_4 migrated to the surface of ZnO, while the holes generated in ZnO moved to the VB of g-C_3N_4. This process reduced electron-hole pair recombination, resulting in the accumulation of excited electron-hole pairs. The accumulated holes in the VB of g-C_3N_4 oxidised water molecules adsorbed on its surface to produce O_2 and protons. Concurrently, electrons accumulated on the surface of ZnO effectively reduced CO_2 molecules adsorbed on the ZnO surface to form CO, CH_4, and CH_3OH with the aid of protons. Cu nanoparticles acted as an electron reservoir, capturing electrons and preventing the recombination of photogenerated electron-hole pairs. Additionally, these nanoparticles supplied additional electrons to the CO_2 reduction process, significantly enhancing the photocatalytic performance[179].

In another study, $Cu_{2-x}S$/g-C_3N_4 composite photocatalysts were synthesised using a straightforward solvothermal method. The composite showed significantly improved CO_2 photoreduction activity for CO and CH_4 compared with both pure g-C_3N_4 and $Cu_{2-x}S$ under UV–Vis and even near-infrared light. This improvement was attributed to effective interfacial contact and the formation of S–C bonds, which increased the number of active sites for CO_2 photoreduction and facilitated better separation of photogenerated electrons and holes. Additionally, the composites exhibited improved CO_2 adsorption capacity, further promoting the CO_2 reduction process. In the reduction of CO_2 to CO, HCOOH served as a key intermediate and the reduction of HCHO to CH_4 also occurred with the composite photocatalyst[180].

The g-C_3N_4/MnP composite catalytic material was prepared using phosphate anchoring. This g-C_3N_4/MnP composite showed superior photocatalytic activity for CO_2 reduction under specific conditions: a g-C_3N_4/MnP mass ratio of 100:1, H_2O as the solvent, and 6 mL of TEOA additive. Its photocatalytic efficiency was five times greater than that of pure g-C_3N_4. In the CO_2 reduction process with g-C_3N_4 semiconductor composites, the MnP complex acted as a crucial co-catalyst. Loading MnP onto the g-C_3N_4 catalyst significantly reduced the recombination rate of photogenerated electron-hole pairs and enhanced catalytic performance[181].

Doping C_3N_4 photocatalysts with metals can increase surface area, enhance visible light absorption, reduce electron-hole pair recombination, accelerate electron transfer to the catalyst surface, and raise redox potential. Single Ni atoms were effectively anchored to g-C_3N_4 nanosheets using boron-oxo species through a simple ion exchange method. The dative interaction between the B atom and the sp^2 N atom of g-C_3N_4 ensured high dispersion of boron-oxo species, with O atoms coordinating with individual Ni(II) sites to form a distinctive six-oxygen-coordinated structure. The optimised single-atom Ni photocatalyst, comparable to Pt-modified g-C_3N_4 nanosheets, demonstrated an excellent CO_2 reduction rate, producing CO and CH_4 as products. Under illumination, the single Ni sites, fully coordinated by O atoms, efficiently captured photoelectrons and preferentially activated adsorbed water molecules to generate H atoms. These active H atoms

 doi:10.20944/preprints202604.1590.v1

then interacted with CO_2, leading to the production of CO and CH_4 through a distinct hydrogen-assisted CO_2 reduction pathway, as shown in Figure 18[182].

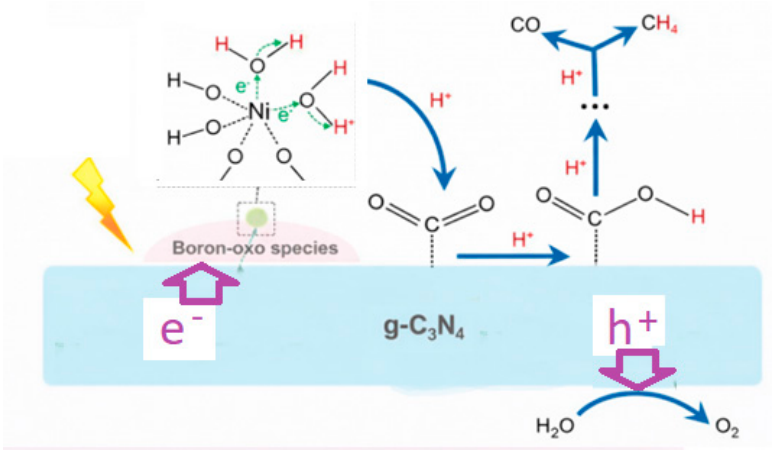

Figure 18. Hydrogen-assisted CO_2 reduction process mechanism over single-atom Ni-OB-CN photocatalyst. Readapted from[182].

Layered porous Ru-loaded and La-doped g-C_3N_4 nanosheets were synthesised through a one-step calcination process, followed by *in situ* photo-deposition of Ru. The resulting material exhibited excellent photocatalytic performance for CO_2 reforming of methane under visible light. The productivities of CO, C_2H_6, CH_3OH and $CH_3CH(OH)CH_3$ were 133, 154, 251 and 133 μmol h^{-1} g^{-1}, respectively. CO_2-TPD and CH_4-TPD tests, together with theoretical calculations, indicated that the enhanced photocatalytic activity was due to the synergistic interaction between bimetallic Ru and La composites. The spatial separation of the valence band maximum and conduction band minimum effectively inhibited recombination and promoted the separation of photogenerated carriers. In other words, the excited electrons migrated to the CB, located around the La atoms, to participate in the reduction of adsorbed CO_2, while the holes moved in the opposite direction towards the VB to engage in the oxidation process[183].

A rapid synthesis method for producing efficient composite photocatalysts was reported, employing a one-step microwave molten salt heating technique. Potassium ions (K^+) were incorporated into the interlayer cavities of polymeric carbon nitride (PCN), while CoN nanoparticles selectively formed on the potassium-doped PCN. The resulting catalysts exhibited interesting photocatalytic performance, achieving a CH_4 productivity of 45.71 μmol g^{-1} h^{-1} with a selectivity of 98.18% under visible light. XPS, UV-Vis and photoelectrochemical analyses indicated that the superior photocatalytic performance of the composite was attributable to several factors: expanded light absorption, improved charge transfer pathways, enhanced carrier separation and transfer efficiency, and increased CO_2 adsorption capacity resulting from the loading of CoN[184]. Additionally, the introduction of K ions shifted the selectivity of CO_2 photoreduction from CO to CH_4, both kinetically and thermodynamically, as confirmed by experimental results and DFT calculations.

The impact of CuO and Sr-doped nanoparticles as cocatalysts on g-C_3N_4 was investigated. First, Sr was intercalated into the g-C_3N_4 framework to reduce the interlayer distance and enhance the electrical transport properties, improving its performance in CO_2 photoreduction. Sr doping increased the electron density, facilitating the eight-electron CO_2 reduction to CH_4 and enhancing CH_4 selectivity while reducing CO production. The photocatalytic behaviour of Sr-doped g-C_3N_4 was influenced by the amount of Sr loaded, with optimised Sr intercalation leading to improved CH_4 yield and selectivity. Nevertheless, Sr intercalation also accelerated H_2O reduction to H_2. Adding CuO to SrCN significantly improved selectivity for CO_2 photoreduction by affecting the rate of electron consumption in reductive reactions. The presence of CuO notably increased the rate of CO_2 photoreduction while suppressing H_2O reduction to H_2. Furthermore, integrating CuO further

 doi:10.20944/preprints202604.1590.v1

increased CH_4 selectivity in CO_2 photoreduction to over 90%. This improvement was attributed to the synergistic effect of enhanced CO_2 chemisorption and increased electron density on the surfaces of CuO and Sr-doped g-C_3N_4, resulting in higher CH_4 yield and selectivity[185].

The interaction interface and synergistic effects between magnesium nitrate hydroxide and molybdenum phosphide (Mg–MoP) were optimised to enhance polymeric C_3N_4. The resulting functionally tailored Mg–MoP/PCN exhibited high efficiency in catalysing the conversion of CO_2 to CH_4 in pure water, achieving a rate of 24.45 μmol h^{-1} g^{-1} and a selectivity of 95.3%. Characterisation showed that the catalytic sites were located on the outer layer of Mg, while the interfacial layer of MoP played a crucial role in transferring photogenerated electrons within the Mg–MoP/PCN composite. The precise interfacial positioning of MoP and Mg was essential for optimising both selectivity and activity in CH_4 production. Extensive investigations using light-irradiated XPS, in situ FTIR and DFT calculations revealed that the interfacial MoP layer acted as the electron collection site, enhancing electron transfer and improving catalytic activity. The outer Mg layer improved selectivity by promoting CO_2 adsorption and stabilising CO^* intermediates[186].

ZnO-gC_3N_4 heterostructures with varying g-C_3N_4 content (15%, 50% and 85%) were synthesised by precipitating ZnO onto the g-C_3N_4 surface at room temperature using an alkaline solution. The satisfactory photocatalytic performance of the analysed materials during CO_2 conversion was primarily attributed to two factors: (i) the enhanced stability of ZnO achieved through its coupling with the g-C_3N_4 surface and (ii) the formation of type-II heterostructures that facilitate the migration of photogenerated charges and increase the photocatalyst's reduction potential. Additionally, it is important to note that a direct Z-scheme mechanism may also be possible, as the CO_2 photoreduction experiments were conducted under UV irradiation. This enabled the photoactivation of both semiconductors (ZnO and g-C_3N_4), potentially enhancing the reduction potential of the heterostructure, since CO_2 reduction could occur in the conduction band of g-C_3N_4, which has a higher reduction potential than that of ZnO[73].

Mesoporous g-C_3N_4 (MCN) with a high specific surface area was synthesised by producing a mesoporous structure to investigate the relationship between CO_2 adsorption capacity and photocatalytic CO_2 reduction activity. Ag particles, serving as co-catalysts, effectively enhanced charge separation efficiency and increased photocatalytic activity. The mesoporous structure of g-C_3N_4 significantly increased its specific surface area and improved CO_2 adsorption capacity, while Ag particles efficiently separated the photogenerated charges and ensured that more electrons were available for CO_2 reduction. Consequently, the CO evolution rate of Ag/MCN reached 1.66 μmol g^{-1} h^{-1}, which was 2.81 and 2.41 times higher than that of pristine MCN and 1.0% Ag/BCN, respectively. This improvement was attributed to the synergistic effect between the mesoporous structure and Ag particles, as it enabled CO_2 molecules to migrate rapidly to the reaction sites (Ag particles) and accelerated CO_2 consumption[187].

An unsaturated edge confinement strategy was employed by coordinating single-atomic-site Ni on bottom-up synthesised porous g-C_3N_4 with few-layers (referred to as Ni_5-CN) using a self-limiting method. In this Ni_5-CN system, a few isolated Ni clusters were distributed along the edge of g-C_3N_4, which helped stabilise the non-edged single-atomic-site Ni species, thereby achieving a high density of single-atomic active sites. This photocatalyst exhibited a CO generation rate of 8.6 μmol g^{-1} h^{-1} under visible light illumination, 7.8 times higher than that of pristine CN (1.1 μmol g^{-1} h^{-1}). X-ray absorption spectrophotometric analysis revealed that the cationic coordination environment of the single-atomic-site Ni centre, formed by Ni–N doping and intercalation within the first coordination shell, enhanced the synergistic N–Ni–N connection and facilitated interfacial carrier transfer. The predicted photocatalytic mechanism confirmed that the introduced unsaturated Ni–N coordination effectively bound CO_2, accelerated the rate-determining step for intermediate formation, and resulted in enhanced CO generation[188].

Pt single atoms anchored on C_3N_4 nanosheets with a unique Pt–N_4 coordination were designed and synthesised. Compared with CN, the synthesised Pt1@CN photocatalyst exhibited enhanced CO_2 photoreduction activity and 100% CO selectivity, outperforming most previously reported single-

 doi:10.20944/preprints202604.1590.v1

atom anchored C_3N_4-based photocatalysts for CO_2 photoreduction using H_2O as a reductant. Moreover, Pt1@CN exhibited excellent long-term photocatalytic stability. Experimental and theoretical results revealed that the Pt–N4-coordinated single atoms acted as active sites, promoting the dynamic transfer of photogenerated charge carriers, adsorption and activation of CO_2 molecules, generation of the *COOH intermediate, desorption of *CO, and evolution of CO, thus accounting for the enhanced CO_2 photoconversion with high CO selectivity[189].

5.3. Non-metal doping and desorption

Non-metal doping is another strategy for materials modification, widely used with TiO_2. Like metal doping, non-metal doping has been employed to enhance the solar harvesting of TiO_2 composites. As shown in Figure 19, non-metal dopants reduce the bandgap of TiO_2 by introducing new energy levels above the valence band, allowing easier electron promotion from the valence band to the conduction band. The most common non-metal dopants are N, C, S and P, which have been used to lower the TiO_2 bandgap and thus enhance visible light absorption[190].

Substitutional non-metal doping introduces defect states that narrow the band gap and enhance visible light absorption. However, at high dopant concentrations, the density of beneficial defects decreases due to defect clustering or recombination effects, reducing photocatalytic efficiency. Photocatalytic activity often decreases as non-metal doping increases because the defect density declines at higher doping levels. Therefore, non-metal doping requires careful consideration to maintain an appropriate defect level while optimising dopant concentration for improved visible light absorption and enhanced photocatalytic activity[134, 191].

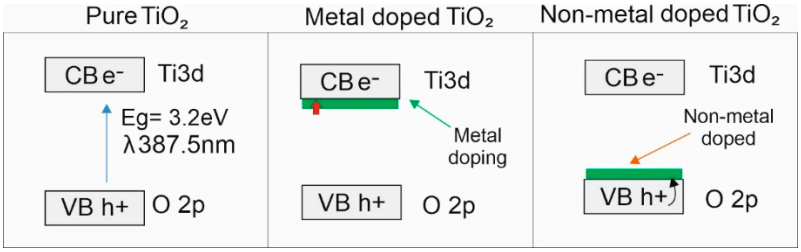

Figure 19. Schematic illustration of band structure of the pure, metal doped and non-metal doped TiO2. Readapted from[102].

According to the literature, C-doped TiO_2 synthesised from a glucose precursor enhanced the activity of CO_2 photoreduction to produce CH_3OH. The highest photocatalytic activity was observed with 6 wt% glucose loading (6C-TiO_2), yielding 19.5 mmol g^{-1} h^{-1} of CH_3OH, twice that of pure TiO_2 (9.5 mmol g^{-1} h^{-1})[192]. Self-assembled C-doped TiO_2 nanoparticles were also used in a direct Z-scheme heterojunction with a three-dimensional hierarchical petal structure of flower-like β-Bi_2O_3. As the C-TiO_2 content increased, CO production reached a maximum rate of 31.07 μmol g^{-1} h^{-1} with 100% selectivity. This rate was more than 9.5 times higher than that of pure TiO_2 and was among the highest reported for TiO_2-based heterojunction photocatalysts[193].

Doping commercial TiO_2 powder with nitrogen has been reported to enhance activity for CO_2 photoreduction. The average CH_4 production rate was 0.191 μmol g^{-1} h^{-1}[194].

Co-doping is a common strategy that employs an electron donor-acceptor pair to reduce charge recombination in non-metal doped TiO_2. Recently, a Cu/P co-doped g-C_3N_4@TiO_2 photocatalyst was used to improve visible light-driven CO_2 photoreduction. The results showed that P and Cu doping increased the specific surface area, reduced the band gap energy and recombination rate, and extended light absorption into the visible region. The optimum CH_3OH production yield was reported as 859 μmol g^{-1} over a 10 h test, corresponding to an average productivity of 85.9 μmol g^{-1} h^{-1}, which was 5 and 11.6 times higher than that of g-C_3N_4 and TiO_2, respectively[191].

TiO_2 co-doped with carbon and nitrogen, featuring numerous oxygen vacancies (designated as C/N-TiO_2-V_O), was synthesised using a hydrothermal method. Several characterisation techniques

 doi:10.20944/preprints202604.1590.v1

confirmed that the carbon and nitrogen originated from N,N'-dimethylformamide (DMF), while the oxygen vacancies were primarily generated by isopropyl alcohol (IPA), which acted as a reducing agent. Co-doping with carbon and nitrogen provided additional active sites, further enhancing CO_2 activation. According to UV-Vis results, compared to pure TiO_2, C/N-TiO_2 exhibited enhanced light absorption, with the absorption edge of C/N-TiO_2-V_O extending to around 410 nm due to the introduction of oxygen vacancies. The material demonstrated 100% selectivity for the photoreduction of CO_2 to CO, significantly higher than the selectivity of C/N-TiO_2 (80.03%) and pure TiO_2 (67.22%). Compared to TiO_2(101), the introduction of carbon, nitrogen and oxygen vacancies in the C/N-TiO_2-V_O material increased the density of states (DOS) at the conduction band edge, enhancing electron transport. Additionally, several defect levels were created, which promoted the separation of photo-generated carriers, thereby improving the photocatalytic reduction of CO_2. In the electron localisation function (ELF) analysis of TiO_2(101) and C/N-TiO_2-V_O, the presence of carbon, nitrogen and oxygen vacancies in the latter, facilitated electron excitation and accumulation around the Ti atoms near the oxygen vacancies. This led to electron enrichment on the Ti atoms, enhancing the material's efficiency in separating photo-generated carriers[195].

Boron and nitrogen co-doped titanium dioxide (TiO_2) nanosheets with a surface area of 136.5 m^2/g were synthesised using ammonia borane, an environmentally friendly and multifunctional reagent. This method was necessary to introduce surface defects on TiO_2. Tested for the photo-reduction of CO_2 with steam under simulated sunlight, they demonstrated approximately 3.5 times higher CO production compared to pristine TiO_2 under the same conditions. Optical measurements, both steady-state and transient, indicated that a reduced band gap, abundant defect states and a higher conduction band energy enhanced light absorption efficiency and facilitated charge transfer at the catalyst/CO_2 interface. Charge redistribution resulting from B and N doping increased surface polarisation, which was further enhanced by oxygen vacancies, leading to significant charge accumulation on the CO_2 molecule. This activation of CO_2 lowered the energy barrier for reduction, enabling the generation of intermediate products and facilitating electron transfer at the interface[196].

Cu-loaded Nb and N co-doped TiO_2 aerogels were synthesised via a sol-gel process, followed by supercritical CO_2 drying and annealing under controlled atmosphere. When exposed to a full-spectrum Xe lamp, the TiO_2 aerogel absorbed photons across both UV and visible wavelengths, promoting the transition of electrons from the valence band to the conduction band and generating electron-hole pairs. The incorporation of Nb and N doping may not only facilitate charge separation but also expand the range of light absorption, particularly in the visible spectrum. The high specific surface area of TiO_2 aerogels enabled efficient CO_2 adsorption and provided abundant active sites for reactions. Simultaneously, Nb and N doping, together with Cu_xO loading, enhanced the optical properties of TiO_2 and the dynamics of charge carriers, increasing the activity for the photoreduction of CO_2 to methanol, with a productivity of 1.69 mmol g_{cat}^{-1} h^{-1}[197].

According to the literature, the Bi_2MoO_6/Ni–N co-doped TiO_2 composite was synthesised using a hydrothermal method followed by a solvothermal process. This composite was employed for CO_2 photocatalytic conversion under visible light irradiation. The results showed that incorporating nickel and nitrogen into TiO_2 resulted in a higher surface area and a narrower bandgap than pure TiO_2. This modification also improved the efficiency of electron-hole separation by reducing CO_2 adsorption on the catalyst surface. The Ni–N co-doped TiO_2 sample exhibited a significant improvement in CO_2 conversion, achieving a rate nine times higher (67.9 μmol/g) than that of undoped TiO_2 (3.2 μmol/g). This enhanced photocatalytic activity was attributed to nitrogen and nickel co-doping in TiO_2, as well as the heterojunction structure. Together, these factors increased light absorption capacity and improved charge carrier separation efficiency[198].

A mild synthesis method was developed to prepare a mesoporous spherical N-doped TiO_2 photocatalyst with site-selective deposition of redox co-catalysts. Nitrogen doping promoted the formation and stabilisation of V_O in TiO_2. Introducing nitrogen into TiO_2 efficiently improved methane selectivity. Nitrogen doping also reduced the bandgap of titanium dioxide, expanding its light absorption range. Furthermore, the generated oxygen vacancies enhanced its capacity to adsorb

 doi:10.20944/preprints202604.1590.v1

and activate CO_2. Suitable dual co-catalysts can be precisely loaded onto N-TiO_2, with the Pt co-catalyst selectively deposited at the oxygen vacancies and CoO_x clusters dispersed around these vacancies. Photoelectrochemical and optical measurements revealed that Pt serves as the primary active centre for CO_2 adsorption and activation, while CoO_x is responsible for H_2O oxidation and proton transfer. The designed composite achieved a maximum CH_4 production of 409.17 μmol/g, which was 180 times higher than that of pure TiO_2[199].

Ni and I co-doped TiO_2 nanoparticles with a mixed anatase-brookite phase were prepared using a hydrothermal-calcination technique. The synergistic effect of co-doping not only broadened the photo-response range, generating abundant photo-generated carriers, but also formed a TiO_2 anatase-brookite phase heterojunction with a suitable band structure for CO_2 reduction. This enabled efficient transfer and separation of carriers. Impurity doping improved the CO_2 adsorption capability of the TiO_2 catalyst, leading to a significant improvement in its photocatalytic CO_2 reduction performance. In addition, theoretical simulation results indicate that co-doping with Ni and I enhanced the light absorption capability of TiO_2 materials. After 15 hours of light exposure, the optimised Ni/I-TiO_2 produced 3.49 μmol/g of CO, 158.25 μmol/g of CH_4 and 246.30 μmol/g of O_2[200].

A hybrid catalyst composed of well-structured TiO_2 hollow spheres and N-doped carbon dots (CDs) was developed for photocatalytic CO_2 reduction to CH_4 under simulated sunlight. Electron microscopy revealed a porous hollow sphere structure uniformly decorated with N-doped CDs. With increased CD content in the composites, the CH_4 formation rate also increased, reaching a maximum of 26.8 μmol h^{-1} g^{-1} which contained 2 wt% CD. H_2 production with this catalyst was minimal, achieving 98% selectivity for CH_4. Furthermore, the catalyst exhibited stability across multiple runs without significant loss of efficiency[201].

A hydrophobic Ni@N-doped TiO_2-HCP (HCP = hydrophobic carbon paper) photocatalyst has been developed to inhibit H_2 evolution and enhance CO_2 conversion efficiency. The photocatalyst features vertically aligned thin TiO_2 nanosheets with oxygen vacancies and nitrogen doping, contributing to strong CO_2 chemisorption, efficient spatial separation and migration of photogenerated carriers and high light absorption. Additionally, the HCP substrate improved the mass transfer of reactant molecules by reducing water transport and increasing CO_2 adsorption, while also preventing the photocatalyst surface from being covered by hydrophobic reagents, thus maintaining abundant reactive sites. When transitioning from a solid–liquid to a gas–liquid–solid interface, the TiO_2-HCP photocatalyst primarily produced CO rather than H_2, effectively suppressing hydrogen evolution. Notably, both the rate and selectivity for CH_4 increased with N-doping and Ni loading on the TiO_2-HCP catalyst. In a gas–liquid–solid CO_2 photoreduction system without any sacrificial agent, the CH_4 production rate of Ni@N-doped TiO_2-HCP reached 134.17 μmol m^{-2} h^{-1} with a high selectivity of 74.6%, representing 21.6-fold and 2.3-fold increases compared to TiO_2-HCP and N-doped TiO_2-HCP, respectively[202].

Titania-based ternary composites were prepared using a two-step process. First, pure and N-doped titanium dioxide powders were synthesised by the Pechini method. These powders were then impregnated with 3% by weight cerium and copper oxide particles. The findings showed that materials derived from a urea precursor incorporated nitrogen atoms into the titanium dioxide structure and inhibited particle growth, resulting in broader particle size distributions and reduced interparticle porosity, thereby increasing specific surface area values. The higher anatase phase content in nitrogen-doped composites was attributed to a more ordered structure. N-doped titania formed at a lower temperature due to the additional energy released from the combustion of the carbon matrix, which promoted phase crystallisation. These results also indicated that N-doped titania-based materials exhibited a greater potential for Ti^{3+} defects. The N-TiO_2/CuO sample showed the highest formic acid production, ca. 2 mmol g^{-1} h^{-1} approximately 40 times greater than that of pure TiO_2. Meanwhile, N-TiO_2/CeO_2/CuO showed significantly increased H_2 evolution, about six times higher than pure TiO_2[152].

In g-C_3N_4, ion doping altered the band structure and created electron or hole traps that prevented the recombination of photogenerated carriers, resulting in a red shift in the spectral

 doi:10.20944/preprints202604.1590.v1

response range. This significantly improved visible light utilisation and enhanced photocatalytic activity. The type, concentration, and preparation method of the doped ions influenced the photocatalytic performance of g-C_3N_4[203]. Highly crystalline poly(triazine) imide was modified by incorporating non-metallic boron to produce two B/PTI catalysts: Bi/PTI, with boron deposited in the six-fold cavity of the structure and Bs/PTI, where boron substituted for carbon in the framework. In the Bs/PTI system, boron incorporation weakened the partial conjugation of PTI, leading to the formation of new frustrated Lewis pairs that activated nitrogen sites for CO_2 reduction. This process followed the hydrogenation mechanism of adsorbed H atoms or protons, producing CO and CH_4. Additionally, boron introduced impurity states into PTI, which helped preventing carrier recombination and enhanced photon utilisation efficiency. Bs/PTI was easily synthesised, had low formation energy and high thermal stability. This provided valuable theoretical insights for designing non-metallic CO_2 reduction catalysts.

A photocatalyst composed of zero-dimensional black phosphorus quantum dots integrated with one-dimensional carbon nitride nanotubes achieved a CO_2 reduction rate to CO of 44.6 μmol g^{-1} h^{-1}. The reduced electron lifetime in these composites indicated that interfacial charge transfer occurred via a non-radiative pathway. Furthermore, the improved separation efficiency of photoinduced charge carriers could be attributed to the edge-state effect, the quantum confinement effect of QDs, and the formation of electron transfer channels between QDs and the nanotubes. The higher photocurrent intensity observed indicated greater photo-response efficiency, while the lower resistance value confirmed enhanced conductivity. The hybrid photocatalyst not only enhanced light absorption but also promoted the separation and transfer of photoinduced charge carriers[204].

A 3D S-doped g-C_3N_4/2D O-doped g-C_3N_4 step-scheme heterojunction was prepared using a hydrothermal method followed by calcination. An S-scheme heterojunction is a type of semiconductor heterojunction used in photocatalysis to enhance charge separation and improve photocatalytic performance. S-scheme heterojunctions are characterised by selective recombination of photogenerated electrons and holes at the interface of two distinct semiconductors. The optimised sample exhibited significantly higher CO_2 photoreduction conversion rates compared to the control groups, including the S-doped, the O-doped and bulk. O and S as dopants improved charge transfer efficiency and light absorption. The production rates of CO and CH_4, increased by 2.18 and 1.77 times, respectively. This design not only effectively separated photogenerated electron-hole pairs but also provided a large surface area and a high number of active sites for multi-electron reactions[205].

Visible-light-driven gas-phase photocatalytic CO_2 reduction to CH_4 was achieved by designing a three-component Au/doped C_3N_4/TiO_2 composite photocatalyst. A high-quality C_3N_4/TiO_2 heterojunction was formed by integrating low concentrations of doped graphitic carbon nitride with commercially available TiO_2 UV-100. This heterojunction enhanced visible light absorption and charge-carrier separation. Additionally, small Au nanoparticles (approximately 3 nm) were selectively deposited onto the TiO_2 surfaces, serving as electron traps and cocatalysts, while also contributing surface plasmonic effects. The doped g-C_3N_4 material, especially when carbon-doped, showed enhanced visible light absorption. Furthermore, B and C doping in C_3N_4, which lowered the conduction band position, played a significant role in achieving high CH_4 selectivity. The 0.77 wt% Au/0.59 wt% C–C_3N_4/TiO_2 composite photocatalyst, providing an optimal balance of these factors, achieved a continuous CH_4 production rate of 8.5 μmol g^{-1} h^{-1} under visible light for at least 10 hours. This level of performance was unprecedented for continuous gas-phase CO_2 reduction with water as a reducing agent, without the need for additional sacrificial agents[206].

Phosphorus/boron co-doped, highly porous carbon nitride nanosheets were successfully synthesised using a green, dual gas-blowing-assisted thermal condensation method. The incorporation of both phosphorus and boron, along with the porous structure and surface groups, enabled fine-tuning of the band structure and electronic properties of graphitic carbon nitride, and also activated the nitrogen atoms located between phosphorus and boron. This activation generated active sites for the CO_2 reduction reaction. This synergistic modification approach simultaneously optimised the physicochemical, morphological, optical and electronic properties of the carbon

 doi:10.20944/preprints202604.1590.v1

nitride, resulting in enhanced photocatalytic activity and selectivity. The CO yield increased to 22.45 μmol g^{-1} h^{-1} under visible light irradiation, approximately 12 times higher than that of pristine graphitic carbon nitride, due to extended visible light absorption, effective charge separation, rapid charge transfer and injection, and improved adsorption capacity[207].

5.4. Catalyst modifications with carbon-based materials

The synthesis of hybrid carbon-based compounds, including semiconductors, is an interesting approach because carbon-based materials are widely available, inexpensive, have a large specific surface area, exhibit significant corrosion resistance, possess strong electrical and thermal conductivity and offer adjustable surface properties[208]. Graphene, graphene oxide (GO), reduced graphene oxide (rGO), carbon nanotubes (CNTs) and carbon quantum dots (CQDs) are the carbon-based materials most frequently used in TiO_2-based catalysts for CO_2 photoreduction[209].

Porous hyper crosslinked polymer TiO_2 graphene composite photocatalysts were evaluated under visible light irradiation, exhibiting a surface area of 988 m^2 g^{-1} and a high CO_2 adsorption capacity of up to 12.87 wt %, with a CH_4 production activity of 27.62 μmol g^{-1} h^{-1}[1210]. In another case, graphene modified TiO_2 spherical shells were used, where the double-sided modification increased the contact area of the structure, enabling more efficient separation of photoelectrons from both sides of the shell, with CO as the main product and only a small amount of CH_4 detected[211].

Reduced graphene oxide–TiO_2 composites were synthesised, achieving a CH_3OH productivity of 2.33 mmol g^{-1} h^{-1}. This was achieved by modifying the band gap and promoting the separation of photogenerated carriers. Cu_xO-doped TiO_2 photocatalysts were combined with CNTs, resulting in a CH_4 production rate of 117 μmol g^{-1} h^{-1} under low-power LED lighting. Achieving such CH_4 generation rates required careful selection of a hole scavenger and gradual adjustment of its concentration[72, 165, 212].

Other studies have shown that combining TiO_2 nanostructured materials, especially TiO_2 nanotubes (TNTs) and nanorods (TNRs), with reduced graphene oxide and carbon quantum dots significantly enhanced photocatalytic CO_2 conversion. For example, rGO-modified TNTs have been developed as visible light-sensitive catalysts for converting CO_2 to CH_4, and the incorporation of rGO improved the efficiency of electron-hole separation. The enhanced photocatalytic activity was confirmed by an increase in CO_2 to CH_4 conversion to 9.27%, twice that achieved with TNTs (5.12%)[213].

In another study, TNTs were modified with biomass-derived CQDs and the composite obtained by mixing 10 mL of CQDs solution with TNTs produced 13.55 and 3.54 mol g^{-1} h^{-1} of CO and CH_4, respectively, corresponding to 2.4- and 2.5-fold higher values compared to bare TNTs[214].

A rod-like TiO_2-modified rGO composite was developed for visible light-driven CO_2 photoreduction, exhibiting a high specific surface area of 287.3 m^2/g and a pore volume of 0.72 cm^3/g, which enabled rapid intraparticle molecular transfer and efficient reactant adsorption (Figure 20**)**. The total carbon yield obtained with TiO_2–rGO was 15.7 times higher than that of pure P25. In addition, the carbon conversion in P25–rGO composites was more than six times higher than that observed for pure P25[215].

 doi:10.20944/preprints202604.1590.v1

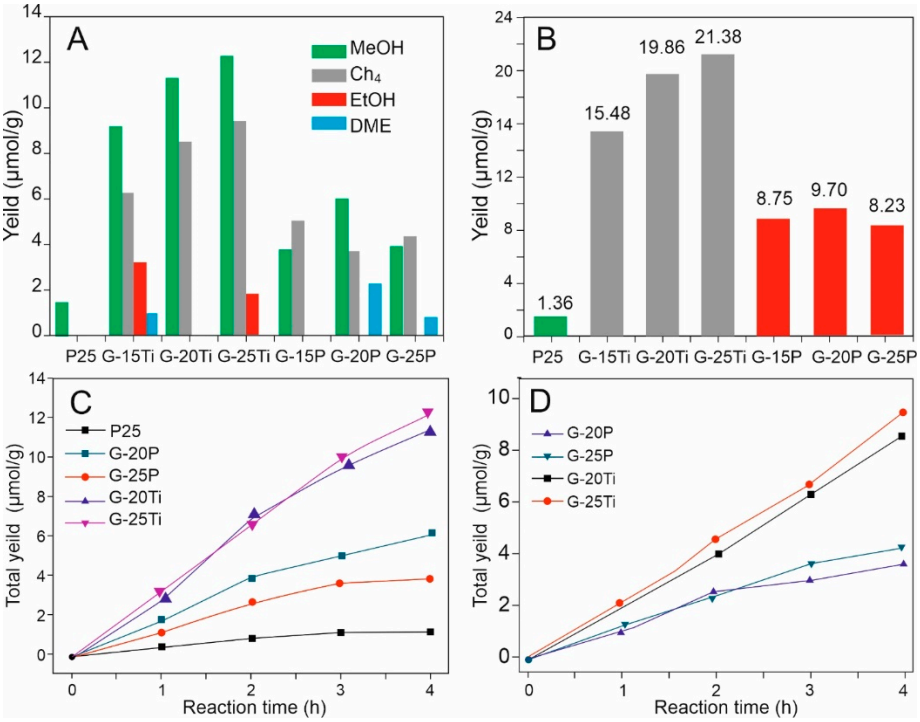

Figure 20. Activity of rGO-modified TiO_2 composites for the photocatalytic CO_2 reduction. (a) yields of MeOH, CH_4, EtOH and DME, (b) total carbon yields for different catalysts. (c) and (d) individual yields of methanol and methane, respectively. Readapted from[215].

According to the literature, urchin-like TiO_2 with a rutile crystal structure was synthesised under acidic conditions. When carbon (C) powder was introduced during the reaction, the rutile TiO_2 transformed into a biphasic structure of rutile and anatase, which has been reported to improve charge separation. In the presence of C/Ag@TiO_2, the productivities were 5.46 μmol g^{-1} h^{-1} for CH_4 and 1.51 μmol g^{-1} h^{-1} for CO, with CH_4 constituting 78.3 mol% of the total. This suggests that the addition of carbon (C) promoted selectivity in CO_2 reduction while limiting the formation of CO[216]. According to Electrochemical Impedance Spectroscopy (EIS) and Mott-Schottky (MS) curves, the absorption peaks of the samples were centred around 350 nm, with C/Ag@TiO_2 showing the highest absorption within the visible light spectrum. The photogenerated electrons in the conduction band of anatase readily transferred to the rutile conduction band, which has a lower Fermi level, and then moved to the Ag surface. The addition of Ag increased the molar ratio of CH_4 to CO, indicating that Ag facilitated enhanced electron transfer. Furthermore, carbon (C) showed a high capacity for H_2O adsorption, allowing photogenerated holes to accumulate on its surface and directly decompose H_2O to form H^+. This accumulation of electrons and H^+ ions promoted the conversion of CO_2 to CH_4, thereby reducing CO production[216].

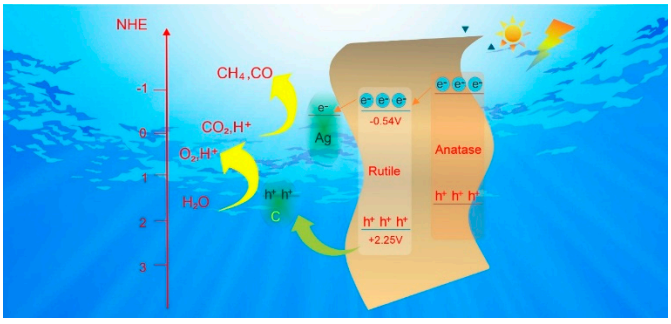

Figure 21. CO_2 photoreduction mechanism over C/Ag@TiO_2. Readapted from[216].

 doi:10.20944/preprints202604.1590.v1

The effect of adding carbon spheres (CS) in proportions from 0.05 to 1.00 g per 1 g of TiO_2 was investigated. The photocatalysts were evaluated in a liquid-phase system under alkaline conditions, with the suspensions exposed to UV-Vis irradiation for 6 hours. The identified products of CO_2 photoreduction were H_2, CO and CH_4. Incorporating 10 wt% CS into TiO_2 enhanced CO production. Intermolecular interactions within the materials may have a more significant impact on the CO_2 photoreduction process than factors such as pore size distribution or increased CO_2 adsorption capacity. Conversely, the enhanced adsorption capacity resulting from the addition of CSs could potentially benefit the performance of the photocatalyst[217].

5.5. Dispersion on supports

The dispersion of TiO_2 on various supports may enhance the electronic properties, product selectivity, and pore structure of the catalysts. Drawbacks include a low mass transfer rate and limited light absorption. TiO_2 photocatalysts can be immobilised on substrates such as fibres, membranes, glass, carbonaceous materials, silica and clays by dip coating or spin coating. Due to its better controllability, dip coating is recommended over spin coating [53, 134, 218].

The photocatalytic activity of dip-coated Pt/TiO_2 supported on mesoporous silica was investigated for CO_2 photoreduction to CH_4, showing significant production of CH_4 and CO, while only small amounts of CH_3OH were formed. Supporting Pt/TiO_2 on mesoporous silica-maintained selectivity for CH_4 generation and enhanced activity[219]. According to the literature, the photocatalytic activity of glass-supported NiO/TiO_2 photocatalysts was investigated for the photoreduction of gaseous CO_2 into hydrocarbon fuels. It was observed that the distribution of Ni, Ti and O atoms on the surface of these photocatalysts was stable, and the BET surface area changed only slightly as NiO loading increased. The absorption edge of the photocatalysts shifted towards the visible region. CH_4 was the main product, with maximum production (4.69 mmol g^{-1} after 90 min) recorded at 10 wt% NiO/TiO_2 loading, which was twice that of pure TiO_2[220].

According to the literature, ordered mesoporous silica, known for its large surface area and stability, was used as a support for dispersing TiO_2. Two sets of photocatalysts with varying Ti contents and support pore sizes were synthesised and evaluated for their microstructures, photoelectric properties, and CO_2 photocatalytic reduction efficiency in both solid-gas and liquid-gas testing modes. During the solid-gas reaction, a clear trend was observed: increasing the pore size of the support resulted in higher yields of both CH_4 and CO. Similar trends were observed in the liquid-gas reaction, yielding CH_3OH[221].

According to the literature, two silica-based materials (SBT10 and SBA-15) with different types and amounts of porosity were investigated as supports for TiO_2 in gas-phase CO_2 photoreduction with H_2O. The enhanced catalytic activity of the SBT10 composite, which outperformed pure TiO_2 despite containing only 10 wt% of the photoactive phase, was attributed to its large specific surface area. The excellent adsorption properties of this mesoporous silica created a substantial reagent reservoir on its surface, which was then progressively converted by the TiO_2 nanoparticles. The hydrophilicity of SBA-15 and the weak interaction of CO_2 with the non-functionalised silica surface were thought to induce competitive absorption of H_2O during the reaction, thereby enhancing the hydrogen evolution reaction in this composite. Despite the weak CO_2 bonding, the large specific surface area allowed a small amount of CO_2 to be trapped within the pores when the catalyst was exposed to a dark CO_2 flow, which was then photoconverted upon irradiation with H_2O[222].

According to the literature, photocatalytic CO_2 reduction in H_2O was enhanced by introducing Co-doped TiO_2 supported on graphene (rGO) as a photocatalyst. Reduced graphene oxide (rGO) increased light absorption capacity, thereby promoting activity and methanol selectivity. Furthermore, the presence of reduced graphene oxide promoted activation of adsorbed water, facilitating the formation of surface hydroxyl groups. This process led to the formation of adsorbed formate ($HCOO^-$) intermediates, which were subsequently reduced at the active sites of titanium (Ti). After 7 hours of irradiation, methanol yields were 32.3 μmol g_{cat}^{-1} for TiO_2, 730 μmol g_{cat}^{-1} for Co-doped TiO_2 and 936 μmol g_{cat}^{-1} for Co-doped TiO_2/rGO after 7 h irradiation[82].

 doi:10.20944/preprints202604.1590.v1

Pt-TiO_2 photocatalysts supported on carbon-based materials were prepared using electrostatic self-assembly. The catalytic activity correlated with the particle size and distribution of the active metal, which were influenced by the type of carbon-based support used. The effectiveness followed this order: multi-walled carbon nanotubes > single-walled carbon nanotubes > reduced graphene oxide > activated carbon. The increased photocatalytic activity of the composites was attributed to their lower band gaps compared to anatase TiO_2, which enabled them to absorb visible light. Furthermore, the combined effect of adding Pt and carbon materials prolonged the lifespan of charge carriers, further enhancing the photocatalytic activity of the composites for CH_4 production[140].

A multifunctional material combining RuO_2:TiO_2 with zeolite 13X enhanced solar-driven methane production. The hybrid material RuO_2 (4.0%)–TiO_2 (26.3%)/Z13X, prepared by solid-state impregnation (mechanical mixing), showed superior performance under simulated sunlight (0.75 W) at 150 °C. After 100 minutes, 88% CO_2 thermo-photoreduction was achieved, resulting in a specific CH_4 production rate of 29.2 mmol g^{-1} h^{-1} and an apparent quantum yield of 20.7%. The zeolite's porous structure prevented the formation of large Ru particles and ensured uniform dispersion across the bifunctional catalyst. However, its reusability declined after three cycles below 250 °C due to water accumulation from the Sabatier reaction. As zeolite 13X preferentially adsorbs water over CO_2, this led to RuO_2 double hydration and consequent changes in the Ru oxidation state[223].

The rGO/TiO_2/Cu and rGO/TiO_2 nanocomposites were synthesised for the production of CH_4 and CO from CO_2 photoreduction with water vapour under simulated solar light. An efficient one-pot method was proposed for directly synthesising the composites in a supercritical CO_2–ethanol medium, which showed better photocatalytic performance than traditional preparation methods. The study examined the impact of varying amounts of rGO as the support on the physicochemical properties and photocatalytic activity of the composites . Absorbance in the visible spectrum increased significantly when TiO_2 nanoparticles were supported on rGO in a supercritical CO_2 medium. The absorption threshold of the composite was higher (indicating a reduced bandgap) as the rGO to TiO_2 ratio increased. This effect was even more pronounced when the binary nanocomposite was doped with Cu, which enhanced electron transfer and increased photocatalytic activity. In the CO_2 reduction process using simulated solar light and rGO/TiO_2 binary catalysts, CH_4 production was minimal compared to CO, regardless of the rGO/TiO_2 ratio in the composite. Catalytic activity improved with increasing TiO_2 content, up to an rGO/TiO_2 ratio of 50% . The catalyst containing equal percentages of rGO and TiO_2 exhibited a CO_2 conversion rate 2.4 times higher than that of P25. When this composite, with equal percentages of rGO and TiO_2, was loaded with 1 wt% Cu, the production rates of CH_4 and CO were 22 and 2.6 times higher, respectively, than those of TiO_2 P25 nanoparticles[224].

A leaf vein-like 2D–1D g-C_3N_4/P-MWNTs donor–acceptor semiconductor was synthesised using a co-grinding and calcination method. CO_2 photoreduction experiments confirmed significantly improved performance compared to pure carbon nitride under UV-Vis and visible light irradiation, as well as good catalytic stability. The incorporation of P-MWNTs enhanced the photoabsorption and photoelectric conversion capabilities of g-C_3N_4[225]. The S-C heterojunction further improved the separation efficiency of photogenerated electron-hole pairs at the interface of Schottky-like barriers. In this leaf-vein-structured catalyst system, one-dimensional P-MWNTs were uniformly distributed on the surface of two-dimensional carbon nitride, acting as electron acceptors and effectively adsorbing CO_2 molecules. This distribution significantly increased the contact probability between CO_2 molecules and photogenerated electrons, thereby enhancing CO_2 photoreduction performance.

g-C_3N_4 was deposited onto nitrogen-doped rutile TiO_2 nanorods via in situ deposition, resulting in the formation of a core/shell step-scheme (S-scheme) heterojunction. The synthesised heterojunction containing 55 wt% g-C_3N_4 achieved the highest CO_2 photoreduction activity (33.35 μmol of CO) without additional co-catalysts or external sacrificial agents. The N-doped rutile TiO_2 core exhibited a small bandgap (~2.68 eV), enabling effective visible-light absorption. Furthermore, the uniform growth of the g-C_3N_4 shell on the nanorods induced a strong interaction between the

 doi:10.20944/preprints202604.1590.v1

components, promoting electron transfer and the S-scheme heterojunction improved charge separation and optimised redox capabilities[226].

Figure 22 illustrates the bandgap structure and the proposed mechanism for the CO_2 photoreduction process, adapted from the paper by Li et al.[227].

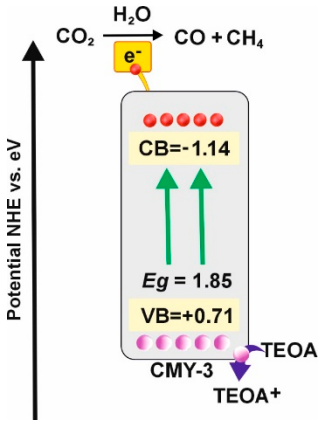

Figure 22. On the left band gap structure and on the right CO_2 photoreduction process of CMR-3. Readapted from[227].

A 2D–1D–2D multi-interfacial electron transfer scheme was developed using a g-C_3N_4/MWNTs/rGO composite. Regarding the reaction mechanism, UV- or visible light-activated pure carbon nitride generates electrons and holes in the conduction band (CB) and valence band (VB) of g-C_3N_4. The photogenerated electrons are transferred to the rGO via two pathways: from carbon nitride to P-MWNTs to rGO, or directly from g-C_3N_4 to rGO, both driven by the built-in electric field at multiple interfaces. Furthermore, the π-π conjugation effect at the interfaces of g-C_3N_4/P-MWNTs and g- C_3N_4/rGO further enhanced the electron generation process within pure CN[227]. The photogenerated holes in the valence band of CN were captured by triethanolamine (TEOA), effectively preventing the recombination of photogenerated carriers. The reaction of CO_2 with H_2O formed H_2CO_3, which then dissociated into $2H^+$ and CO_3^{2-}. CO_2 molecules adsorbed on the catalyst surface reacted with photogenerated electrons and H^+ ions to form CO molecules, which could either desorb from the catalyst surface as CO gas or remain adsorbed to undergo further reactions. The latter could react with additional electrons and H^+ ions to produce CH_4 molecules. Finally, CH_4 gas can be desorbed from the catalyst, following a typical 2/8 electron reduction process.

5.6. Surface sensitisation and heterojunctions

Surface sensitisation is another strategy for enhancing the efficiency of photoexcitation processes and expanding visible light harvesting capacity. The semiconductor is used primarily as a charge carrier rather than as an electron and hole generator, and the process is rapid. Dyes are the most commonly used sensitisers, with the dye acting as a light harvester and the semiconductor serving as an electron acceptor. Light-sensitised squaraine dyes were synthesised and combined with TiO_2 to produce dye-sensitised catalysts. After an induction period, the photodegraded squaraine was found to act as an effective photosensitiser under irradiation above 400 nm, achieving a turnover number for CO production of 165 over 70 h[190, 228, 229].

The most widely used method to enhance the photocatalytic performance of TiO_2 is heterostructure synthesis. Two compatible semiconductors are combined to form a heterostructure, which performs better than each semiconductor alone[190, 230]. For example, combining surface-modified TiO_2 nanoparticles with RGO and CeO_2 effectively promotes the conversion of CO_2 to CH_3OH and C_2H_5OH. The modified TiO_2/RGO/CeO_2 photocatalysts produced CH_3OH (641 μmol g^{-1} h^{-1}) and C_2H_5OH (271 μmol g^{-1} h^{-1}), seven times more than pristine TiO_2[231].

 doi:10.20944/preprints202604.1590.v1

According to the charge carrier separation process, three types of TiO_2-based heterojunctions can be distinguished: type II, direct Z-scheme, and S-scheme heterojunctions. Recent research on this topic has been summarised elsewhere[43, 102, 232, 233]. The following sections present several examples of Z-scheme and S-scheme heterojunctions. The classical Z-scheme heterojunction describes a photocatalytic system in which two semiconductors are independently excited by light, and the less energetic electrons and holes recombine across their interface. This recombination preserves only the most reducing electrons in one semiconductor and the most oxidising holes in the other[234-236].

In contrast, the S-scheme model emphasises Fermi-level alignment and the formation of a strong built-in electric field at the interface. Instead of requiring two full photoexcitation events, the S-scheme relies on selective recombination driven by this internal field. As a result, charge migration becomes directional and occurs only for the low-energy carriers, while the high-energy carriers remain spatially separated. This makes the S-scheme physically more realistic for many modern heterojunctions. Both schemes produce strong redox carriers, but they differ in the mechanism that leads to this separation. The Z-scheme is governed by geometry and band alignment, whereas the S-scheme is field-driven[74, 235-238].

The type II heterojunction is one of the most widely used configurations and can be formed by combining a semiconductor with a higher conduction band with another that has a lower valence band[239]. High CH_4 productivity was achieved using g-C_3N_4/TiO_2 photocatalysts under irradiation with an 8 W UV lamp for 4 hours[240]. Figure 23 also shows the photoreduction mechanism of modified TiO_2/RGO/CeO_2 photocatalysts leading to CH_3OH and C_2H_5OH.

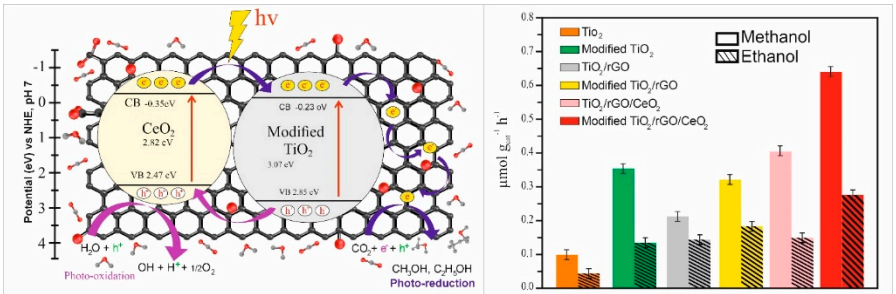

Figure 23. Heterojunction photocatalysts for CO_2 photoreduction: (a) the photoreduction mechanism of modified TiO_2/RGO/CeO_2 photocatalysts and (b) the CH_3OH and C_2H_5OH yields for different photocatalysts. Readapted from[102].

A hierarchical g-C_3N_4@TiO_2 hollow sphere was synthesised by assembling a TiO_2 shell onto the surface of a hollow carbon nitride sphere (HCNS). The photocatalytic performance showed a synergistic effect between the g-C_3N_4 and P-25 components, achieving a CH_3OH productivity of 11.3 µmol g_{cat}^{-1} h^{-1}. This rate was over 10 and 5 times higher than that of pristine P-25 and g-C_3N_4, respectively. As previously mentioned, the heterojunction facilitated rapid electron transfer at the semiconductors interface and improved the separation of electron-hole pairs, as shown in Figure 24. Additionally, the carbon nitride hollow structure enhanced light harvesting in the visible range and induced multiple light reflections within the interior cavity[241].

 doi:10.20944/preprints202604.1590.v1

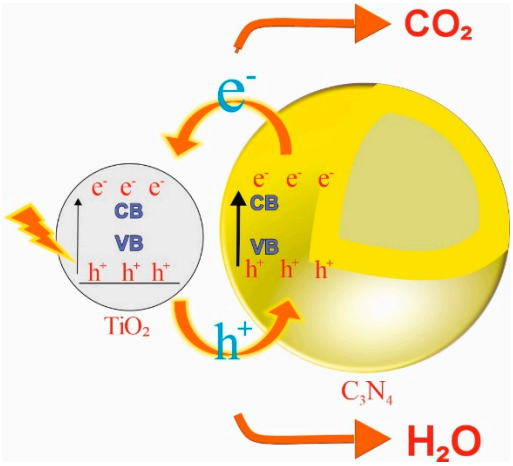

Figure 24. Illustration of the CO_2 photodegradation mechanism over g-C_3N_4@TiO_2 hollow nanosphere. Readapted from[241].

In another study, a porous core-shell photocatalyst was developed by combining TiO_2 nanoparticles with graphitic carbon nitride using self-assembled supramolecular precursors, achieving productivities of 26.89 μmol g^{-1} h^{-1} for CO, 8.91 μmol g^{-1} h^{-1} for CH_4 and 1.61 μmol g^{-1} h^{-1} for H_2, all significantly higher than those of the pristine semiconductors. The confined space within the core-shell structure played a major role by enhancing the concentration of reactants and increasing their likelihood of interacting with the catalyst. This same confinement at the core-shell interface also improved electron transfer through the Z-scheme concept[242].

A heterojunction nanocomposite photocatalyst combining $ZnIn_2S_4$ and TiO_2 was investigated, exhibiting higher yields of CO and CH_4 than those achieved with both semiconductors alone. The high CO yield with $ZnIn_2S_4$ was attributed to its negative reduction potential of -0.71 eV. In contrast, the CH_4 yield was higher with TiO_2, which has a less negative reduction potential of -0.37 eV. A nanocomposite containing 15 wt% $ZnIn_2S_4$ yielded 1754 μmol/g for CO and 481 μmol/g for CH_4 in 10 h experiments[232].

The ratio of the $AgVO_3$/Ag/TiO_2 nanowire composite was optimised by adjusting the mass ratio between $AgVO_3$ and TiO_2 nanowires using a hydrothermal method. Lower methanol productivity was attributed to the formation of larger Ag metal and $AgVO_3$ particles, resulting in a reduced specific surface area at lower $AgVO_3$ loadings. As the $AgVO_3$ loading increased to 50 wt% and 75 wt% on TiO_2-NWs, aggregation of $AgVO_3$ and Ag particles led to poor dispersion and lower surface area, causing a decrease in CH_3OH production yield to 6626.5 and 5603.3 μmol g^{-1} h^{-1}, respectively. In contrast, a 25 wt% $AgVO_3$ loading on TiO_2-NWs catalysts achieved the highest productivity (9561.3 μmol g^{-1} h^{-1} after 2-8 hours of accumulation time)[45].

An S-scheme mechanism was proposed to explain the charge transfer process, as illustrated in Figure 25. According to this mechanism, photoexcited electrons from the conduction band of $AgVO_3$ are transferred to the valence band of TiO_2 nanowires, where they recombine with holes present in this material. As a result, electrons with stronger reduction potential remain in $AgVO_3$, while holes with higher oxidation potential remain in TiO_2, boosting the photocatalytic reactions. Additionally, the SPR effect of metallic Ag on the photocatalyst surface also contributes to the enhancement of photocatalytic activity.

 doi:10.20944/preprints202604.1590.v1

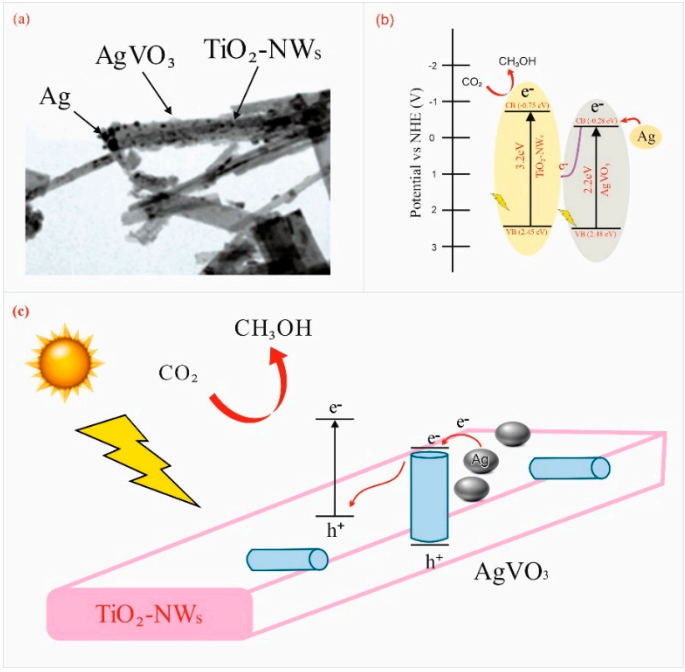

Figure 25. Band Structure and Charge Transfer Mechanism of $AgVO_3/TiO_2$-NanoWires (NWs). (a) the TEM image of the 25 wt% $AgVO_3/TiO_2$-NWs photocatalyst, (b) the band energy positions after contact between the semiconductors and the proposed charge transfer mechanism under light irradiation, and (c) the S-scheme charge transfer mechanism for the $AgVO_3/TiO_2$-NWs system under irradiation. Readapted from[45].

$V_2AlC@V_2O_5$ was supported on TiO_2 and immobilised on a honeycomb structure using the sol-gel dip-coating technique[243]. Reducing CO_2 with water using the $V_2AlC@V_2O_5/TiO_2$ composite primarily produced CO with a small amount of CH_4. However, the yields of CH_4 and H_2 increased significantly when CO_2 was reduced via the bi-reforming of methanol, as shown in Figure 26. The partial oxidation of V_2O_5 formed heterojunctions between V_2AlC/TiO_2 and V_2O_5/TiO_2, which effectively separated photoinduced charges and reduced recombination. Under UV light irradiation, electrons were initially generated on TiO_2 and then transferred to V_2O_5 due to its lower conduction band position compared to TiO_2. Simultaneously, holes moved from the valence band of V_2O_5 to TiO_2 because of their suitable relative potentials. In addition, the strong interphase interaction and high dispersion of TiO_2 on V_2AlC facilitated effective electron transfer towards V_2AlC. A recent breakthrough revealed that V_2C and TiO_2 have appropriate Fermi levels, enabling efficient electron transport at the interface.

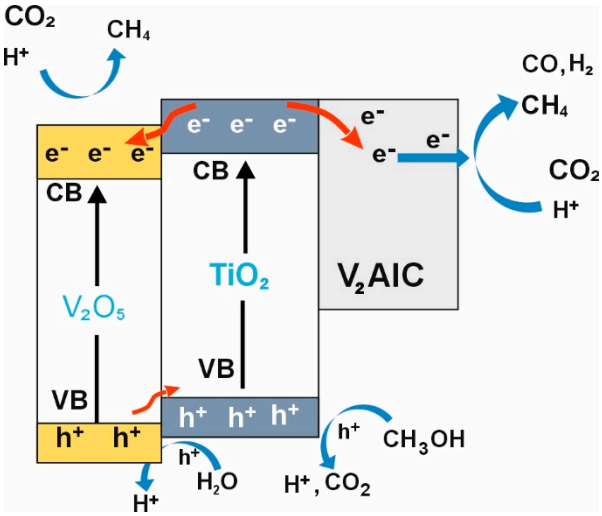

 doi:10.20944/preprints202604.1590.v1

Figure 26. Mechanism of photocatalytic CO_2 reduction using a water/methanol mixture. Readapted from[243].

ZnSe-sensitised hierarchical TiO_2 nanosheets encapsulating MIL-125(Ti) hollow nanodisks were designed, forming a sandwich-like structure through a series of solvothermal and selenylation reactions, using MIL-125(Ti) nanodisks as the precursor. TiO_2 nanosheets were transformed from MIL-125(Ti) and grew in situ on both sides of the MIL-125(Ti) shell, forming sandwich-like hollow nanodisks. The MIL-125(Ti)/TiO_2 ratio could be adjusted by varying the solvothermal time. The ternary hybrids provided enhanced light utilisation and numerous accessible active sites due to their bimodal pore-size distribution and hollow sandwich-like heterostructure. The multi-channel charge transfer routes in the ternary heterojunctions enhanced charge transfer and separation, extending the lifespan of the charge-separated state and increasing CO_2 photoreduction performance. The optimised ternary hybrid achieved significant yield rates for CO (513.1 μmol g^{-1} h^{-1}) and CH_4 (45.1 μmol g^{-1} h^{-1})[244].

TiO_2/$CsPbBr_3$ S-scheme heterojunctions were prepared by facet engineering of TiO_2 to modulate the internal electric field. This method aimed to control charge transfer dynamics and enhanced photocatalytic activity. The composite material achieved a CO yield of 12.5 μmol h^{-1} with a selectivity of 90.2%, which was 15.6 times higher than that of pristine T-101 TiO_2. This improvement was attributed to the exposed facets of TiO_2, as T-101/$CsPbBr_3$ exhibited a CO yield 5.6 times higher than T-001/$CsPbBr_3$. XPS and EPR analyses provided evidence of electron migration between the components, confirming the S-scheme mechanism of charge transfer in TiO_2/$CsPbBr_3$ heterostructures. DFT calculations indicated that the increased Fermi level gap between T-101 and $CsPbBr_3$ generated a stronger internal electric field with more pronounced band bending, creating a larger driving force compared to the T-001/$CsPbBr_3$ heterostructure, and effectively eliminating unnecessary photoinduced charge carriers[237].

A one-dimensional catalyst was synthesised using oxygen-deficient blue TiO_2 to enhance electron mobility and increase visible light absorption. Additionally, hexagonal $ZnIn_2S_4$ nanosheets, which have a small bandgap and improved visible light absorption, were used to form effective heterostructures. The constructive interaction between these two materials promoted efficient charge transfer from $ZnIn_2S_4$ to blue TiO_2. This significantly improved the activity and selectivity of the CO_2 conversion processes, with CH_4 productivity ten times higher than that of $ZnIn_2S_4$ alone, while bare blue TiO_2 did not produce CH_4. The high activity was attributed to the accumulation of electrons and the increased CO binding energy intensified by oxygen vacancies, which promoted the subsequent protonation step. However, a high loading of blue TiO_2 in the composite materials led to lower activity and selectivity, as it can completely cover $ZnIn_2S_4$, limiting the exposure of $ZnIn_2S_4$ facets and thus inhibiting charge transfer and separation[245].

Russelite Bi_2WO_6 has been extensively documented for its effectiveness in the photocatalytic degradation and mineralisation of various pollutants and organic compounds. These materials exhibit a perovskite-like structure with hierarchical morphologies, which endows them with exceptional optoelectronic properties. Bi_2WO_6/TiO_2 heterojunctions have been developed and tested for gas-phase CO_2 photoreduction efficiency under UV light, to stimulate the excitation of both semiconductors. Bi_2WO_6 primarily facilitated the production of CO and H_2, with smaller amounts of CH_4 and $C_2H_4O_2$. In contrast, coupling Bi_2WO_6 with TiO_2 semiconductors resulted in a 39.8-fold and 2.7-fold increase in CH_4 production compared to bare Bi_2WO_6 and TiO_2, respectively. The composite material also produced H_2 and CO, as well as smaller amounts of $C_2H_4O_2$, C_2H_4, and C_2H_6. The highest CH_4 yield was 15.9 μmol g_{cat}^{-1} after 15 hours of UV illumination, exceeding the yields obtained with either individual material, due to the more effective charge transfer mechanism in the heterojunction. Photoelectrochemical measurements showed enhanced charge transfer in the hybrids, with a decrease in charge transfer resistance upon illumination. Additionally, charge dynamics studies revealed a prolonged lifetime of photogenerated carriers in the hybrids and slower recombination rates, resulting from improved charge transfer in the heterojunction, so that reduction and oxidation occurred on TiO_2 and Bi_2WO_6, respectively. Moreover, surface composition studies showed

 doi:10.20944/preprints202604.1590.v1

preferential adsorption of CO_2 as carbonate or bicarbonate species on TiO_2 active sites, which participated in both the reaction and deactivation pathways[246].

A bifunctional dual-vacancy modified hollow heterojunction photocatalyst was also studied for the photoreduction of CO_2 to CO, coupled with the selective oxidation of benzyl alcohol to benzaldehyde. CO and benzaldehyde were produced with productivities of 105 and 323.5 μmol g^{-1} h^{-1}, respectively. A synergistic catalytic effect arose from the hollow heterostructures: TiO_2 with oxygen vacancies (TiO_{2-x}) and $Zn_{0.3-x}Cd_{0.7}S$ with zinc vacancies. The nanoparticles of the latter material were anchored in situ on the exterior of the TiO_2 shell, ensuring a close interface between the two components. During this process, partial reduction of TiO_2 generated TiO_{2-x} with oxygen vacancies. The hollow structure provided more active sites and enhanced light absorption for CO_2 photoreduction combined with benzyl alcohol oxidation, while the compact Z-scheme heterojunction facilitated carrier separation in the composite[247].

$CuCo_2S_4$ thiospinel was prepared with a hierarchical yolk-shell hollow structure using a cost-effective solvothermal method without surfactants or templates. This structure enhanced multiple scattering and reflections, maximising photon utilisation. Furthermore, Bi-modified TiO_2 was encapsulated in the thiospinel using the isoelectric point-assisted calcination technique, ensuring close contact between the two materials and, in principle, preventing random coupling, according to Figure 27[90]. This resulted in the formation of a Z-type heterojunction (CCS@3B-TiO_2). The CH_4 and CO yields were 42.2 and 25.5 μmol g^{-1}, respectively, which were ten times higher than those achieved with pure TiO_2 for methane production. Bi ions enhanced light absorption and promoted the separation and transfer of electron–hole pairs. Furthermore, the formation of a secondary phase, $Bi_2Ti_2O_7$, was observed on the TiO_2 surface, imparting surface basicity and stabilising CO_2 and the lower oxidation state of Bi^{3+} compared to Ti^{4+}. This facilitated the introduction of oxygen vacancies and modified the electronic properties[90].

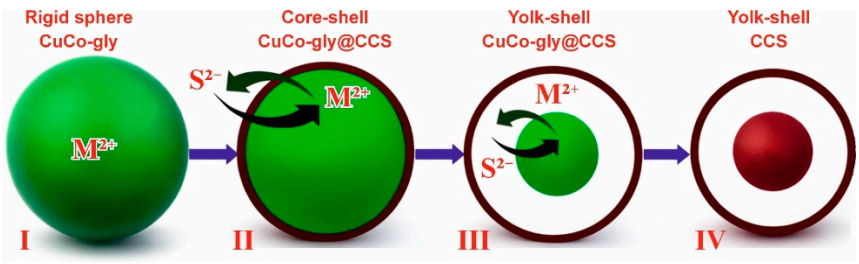

Figure 27. Scheme of $CuCo_2S_4$ yolk-shell hollow spheres. Readapted from[90].

Silver and cadmium sulphide nanoparticles, with an average particle size of less than 20 nm, were loaded onto the surface of TiO_2 nanotubes (Ag/CdS/TNTs) using sodium dodecyl benzene sulfonate, increasing the number of surface-active sites on the nanocomposites. Photocatalytic experiments with triethanolamine and acetonitrile as sacrificial agents yielded a CO productivity of 1456 μmol g^{-1} h^{-1}. Additionally, Ag/CdS/TNTs nanocomposites exhibited a H_2 evolution rate of 3700 μmol g^{-1} h^{-1}, which was twice that of pure TiO_2 due to the formation of a S-scheme heterojunction[248].

TiO_2–Cu_2ZnSnS_4 nanocomposites were prepared via a one-step hydrothermal procedure for visible light-driven production of CO and CH_4. The enhanced photocatalytic activity of the hetero-integrated nanocomposites was attributed to their small nanocrystal size, large surface area with more active sites, enhanced absorption of visible light and facilitated interfacial contact between TiO_2 and Cu_2ZnSnS_4, which promoted electron migration, suppressed recombination of photo-induced charges, and enhanced the redox capabilities of charge carriers. Increased charge separation occurred due to electric field-induced drift resulting from the formation of a p-n junction at the interface of n-type TiO_2 and p-type Cu_2ZnSnS_4[249].

Hybrid-phase $MoSe_2$ nanosheet-coated Cu-doped TiO_2 nanofibres effectively absorbed light across an extended band edge, exhibited prolonged charge carrier lifetimes and facilitated rapid charge transport via an S-scheme mechanism. In terms of morphology engineering, $MoSe_2$

 doi:10.20944/preprints202604.1590.v1

nanosheets with varying proportions of the 1T phase and abundant active sites were synthesised, influencing their interaction with the reaction environment to enhance CO_2 photoreduction by creating highly hydrophobic surfaces. However, excessive $MoSe_2$, particularly when the 2H phase predominates on the Cu-TiO_2 nanofibre surface, reduced active site density and introduced a light-screening effect. Moreover, excessive $MoSe_2$ accumulation on the Cu-TiO_2 surface can promote charge carrier recombination, thereby reducing the photocatalytic efficiency[250].

Pb^{2+} ions in PbO-decorated TiO_2 composites induced the transformation of brookite TiO_2 quasi-nanocubes (pristine TiO_2) into heterophase junctions comprising brookite nanorods and anatase nanoparticles. The 1.0% PbO/TiO_2 sample achieved the highest CH_4 and CO productivities of 53 and 6 μmol g^{-1} h^{-1}, respectively, with an overall photoactivity (total consumed electron number) of 437.7 μmol g^{-1} h^{-1}. This corresponded to a 33.2-fold increase compared to pristine TiO_2. Moreover, the brookite/anatase TiO_2 heterophase junctions effectively suppressed photogenerated charge recombination, while the presence of PbO with these heterophase junctions enhanced CO_2 adsorption and activation processes[251].

S-scheme heterojunction of TiO_2/g-C_3N_4 was formed, followed by a hydroxyl group removal from the surface of the catalyst by mild-temperature hydrogen reduction, creating active sites rich in vacancies. The CO_2 photoreduction rate to produce CH_4 without additional hole scavengers except pure water was approximately 27.4 μmol g^{-1} h^{-1} with 93.6% selectivity, 39 times higher than pristine g-C_3N_4 and 5.6 times higher than TiO_2. Characterisation techniques including photoluminescence, time-resolved photoluminescence, femtosecond transient absorption spectroscopy and electrochemical impedance spectroscopy have demonstrated that the defects promoted ultrafast charge carrier transfer pathways and enhanced interactions at heterojunction interfaces. Moreover, H_2 reduction of the photocatalyst improved the transfer of light-excited charges to the surface, hence boosting its strong redox capabilities in photocatalytic reactions[252].

The Co_3O_4/Ti^{3+}-TiO_2/NiO hollow core-shell heterojunction demonstrated significantly enhanced photocatalytic performance compared to bare TiO_2. This included H_2 evolution (2135 μmol g^{-1} h^{-1}, a ca. 80-fold increase) and CO_2 photoreduction (H_2/CH_4/CO = 34.85/132.25/12.65 μmol g^{-1} h^{-1}, ca. 30-fold increase), along with improved CO_2 photoreduction selectivity. These enhancements were attributed to the synergistic effects of Ti^{3+} ions and oxygen vacancies and of dual p-n junctions within the heterojunction structure. In particular, the Ti^{3+}-TiO_2, with shallow donor levels induced by Ti^{3+}/V_O, not only enhanced solar harvesting efficiency, but also lowered the threshold for H_2O^* to H^* and $^*CO$ to $^*CHO$ reduction, so improving the selectivity for hydrogen evolution reaction and methane production. This included boosting H^+ diffusion and the adsorption of H_2O/CO_2/$^*CO$. Furthermore, the dual p-n junction, with a suitable potential gradient, efficiently improved the separation and transport of photogenerated carriers. The synergistic effects of Ti^{3+}/V_O and dual p-n junctions ensured a balanced generation, separation, and transportation of photo-generated charge carriers. This facilitated rapid electron diffusion into water for the photoreduction of H_2O to H_2 and CO_2 photoreduction to CH_4/CO[253].

Binary Cu BTC@TiO_2 catalysts with adjustable inner cavities were synthesized using copper-based metal organic framework octahedrons via a solvothermal reaction. The inner Cu-BTC octahedrons were selectively etched into hollow octahedral structures using HF. Subsequently, Cu-BTC@CuSe@TiO_2 hollow octahedrons (HOs) were created through a selenization reaction. These structures exhibited several beneficial properties, such as abundant active sites for CO_2 adsorption and reduction reactions, a shortened charge transfer distance to mitigate electron-hole recombination and internal reflection/scattering effects that enhanced solar light utilisation. Furthermore, the formation of dual p-n heterostructures between p-type CuSe and n-type semiconductors (Cu-BTC and TiO_2) effectively facilitated spatial separation and migration of charge carriers. CO production rate was 72.3 μmol h^{-1} g^{-1} with 100% selectivity[254].

In order to enhance sunlight utilisation, improve the separation and transfer efficiency of photogenerated electron-hole pairs, and optimise the reaction on the catalytic surface, a $CuInS_2$/C/TiO_2 hierarchical tandem heterostructure has been designed. Various in-situ

 doi:10.20944/preprints202604.1590.v1

characterisations and DFT simulations revealed that CQDs not only served as a co-catalyst but also acted as a bridge between TiO_2 and $CuInS_2$. This bridging role facilitated the efficient separation and concentration of photogenerated electron-hole pairs while effectively preventing their recombination. This structure significantly enhanced the performance due to the construction of a tandem heterojunction electron transfer mechanism, which enabled electrons to flow in an orderly and directional manner, significantly increasing the number of effective electrons involved in the protocatalytic reaction process[255].

A $CsPbBr_3$@mesoporous TiO_2 beads S-scheme heterojunction was synthesised by incorporating $CsPbBr_3$ perovskite QDs into the pores of titania. The CO_2 photoreduction performance was examined in a CO_2-saturated ethyl acetate and water mixture. The heterostructure increased the photocatalytic efficiency, resulting in close contact and strong interaction, which ensured efficient electron transfer between them. This electron transfer created a built-in electric field from $CsPbBr_3$ to TiO_2, which promoted the formation of the S-scheme heterojunction[256].

Covalent organic frameworks (COFs) have demonstrated significant potential in forming S-Scheme junctions, which feature both spatial separation and a robust redox capability of photogenerated charge carriers. S-scheme TiO_2/COF heterojunctions were investigated. When T-001 and T-110 TiO_2 were combined with COF, their activity for photocatalytic CO_2 reduction was significantly enhanced. With an optimal amount of coupled COF, T-001/COF achieved a photocatalytic CO_2 reduction rate of 2.5 μmol g^{-1}, which was approximately 4.2 times greater than that of T-001 nanosheets alone, even if lower than other simpler materials. When the weight ratio of COF exceeded 3%, the photocatalytic activity for CO_2 reduction was suppressed. Samples with 101 facets exhibited a boost of 14.5 times in activity. For instance, T-101/3% COF achieved a photocatalytic CO_2 reduction rate of 11.6 μmol h^{-1} with a selectivity of 95% for CO. The transfer of electrons between each component was demonstrated by XPS and EPR, confirming the S-scheme pathway of charge transfer[257].

Similarly, a van der Waals heterojunction composite, integrating g-C_3N_4 with nitrogen vacancies and COF, demonstrated CO evolution rate for the heterojunction 45 and 15 times higher than that of g-C_3N_4 and g-C_3N_4/COF, respectively. Additionally, the π-π stacking interactions helped stabilise nitrogen vacancies during the reaction. Consequently, g-C_3N_4(NH)/COF demonstrated proper selectivity and stability in the photocatalytic reduction of CO_2 to CO. Both experimental and theoretical results indicated that the S-scheme system effectively integrated CO_2 capture, activation and charge transfer features[258].

The composite material TiO_2@CTF-Py (Covalent Triazine Framework) connected the inorganic semiconductor to a nitrogen-rich, porous, conjugated and coordinating organic structure through covalent bonds. When modified with Co^{2+}, this composite served as an effective photocatalyst for converting CO_2 to CO with high selectivity, using water as the electron donor and operating without the need for external photosensitisers or sacrificial agents. The 60-TiO_2@CTF-Py composite exhibited the highest performance, achieving 43 μmol g^{-1} h^{-1} CO productivity and a selectivity of 98.3%. UV–Vis light exposure promoted electrons in both nano TiO_2 and CTF-Py materials. The excited TiO_2 electrons transferred to CTF-Py and finally accumulated at the metal sites for CO_2 reduction, while the positively charged holes gathered in the TiO_2 VB for H_2O oxidation. The performance was attributed to its porous structure, which promoted CO_2 adsorption and diffusion, to the Z-Scheme heterojunction structure and to the covalent bonding within TiO_2@CTF-Py that allowed efficient separation and migration of photogenerated electrons[42].

TiO_2 nanoflower composites with the UiO-66 metal organic framework were investigated and the results indicated that the composite, particularly the one containing 25% UiO-66, significantly enhanced the CH_4 and CH_3OH production compared to the separated components, as usual increasing the separation of electrons and holes (e^-/h^+) and enhancing the CO_2 adsorption capacity. The efficiency of electron-hole separation and transfer was assessed using transient optical current, impedance spectroscopy and photoluminescence[259].

 doi:10.20944/preprints202604.1590.v1

TiO_2 was activated to enable CO_2 reduction under visible light by adding Bi_2MoO_6 as an electron donor, achieving 27.1 μmol g^{-1} methanol production. Introducing Bi_2MoO_6 nanoparticles into V_O-modified TiO_2 facilitated the electron transfer across the interface. This enabled TiO_2 active sites to adsorb CO_2, while photogenerated charges from Bi_2MoO_6 facilitated CO_2 reduction reaction, as testified through photophysical and photoelectrochemical characterisations[260].

Photonic crystals composed of TiO_2 nanotube arrays with periodically modulated diameters were synthesised using a precise charge-controlled pulsed anodisation method and adorned with Au nanoparticles. CO_2 photoreduction was tested at various irradiation wavelengths and illumination sequences. The spectral composition of incident light could be employed to freely switch photoreduction pathways between a methane-producing route and a plasmonic Z-scheme that generated HCHO and CO. Under simulated sunlight, CH_4 was observed as the dominant product, achieving 302 μmol g^{-1} h^{-1} productivity with 89.3% selectivity. Conversely, HCHO and CO were primarily produced (420 μmol g^{-1} h^{-1} and 323 μmol g^{-1} h^{-1}, respectively) under visible + UV light[261].

A 0D/1D $Cu_{2-x}S/TiO_2$ S-scheme photocatalyst was synthesised using a solvothermal method. The CH_4 production rate was 14.1 μmol h^{-1}, approximately 3.9 times greater than that of pure TiO_2. By integrating $Cu_{2-x}S$ with TiO_2 to form an S-scheme heterojunction, the charge separation and reduction activity of the hybrid photocatalyst were enhanced efficiently compared to pure TiO_2. The uniformly distributed $Cu_{2-x}S$ improved light absorption and CO_2 adsorption of the hybrid photocatalyst. Moreover, the photothermal effect due to the SPR of $Cu_{2-x}S$ synergistically increased the efficiency for the CO_2 photoreduction[262].

A series of Bi_2WO_6/TiO_2 composite photocatalysts with varying ratio of Bi_2WO_6 nanosheets to TiO_2 nanobelts was synthesised using a hydrothermal technique. A methane yield of 11.95 μmol g^{-1} in 8h experiments was achieved and DRS indicated that the Bi_2WO_6 nanosheets extended TiO_2's light absorption into the visible spectrum, achieving an apparent bandgap as small as 1.9 eV. The physicochemical and optical properties of the photocatalysts demonstrated improved CO_2 adsorption and the formation of the heterojunction effectively facilitated charge carrier transfer, prolonging the separation time of photoinduced charge carriers and thereby enhancing photocatalytic performance. Additionally, the reduced recombination rate of electron-hole pairs contributed to increase the CO_2 photoconversion efficiency[263].

The photocatalytic efficiency of g-C_3N_4 demonstrated heavily influenced by the recombination probability of photogenerated carriers. When g-C_3N_4 was combined with other semiconductors, an internal electric field was created at the heterojunction interface, leading to band bending. This formed a close-contact interface that enhanced the transfer and separation of free charges, addressing the issue of poor visible light absorption. The formation of heterogeneous interfaces, along with suitable electronic structures and band gap configurations, can effectively boost photocatalytic activity. For instance, an efficient CO_2 photoreduction catalyst was produced by embedding ZIF-67-derived Co_3O_4 hollow polyhedrons into a 3D graphitic carbon nitride using a NaCl template, followed by loading Ag through photo-deposition. The composites were characterised by two simultaneously created heterojunctions: a p-n junction between Co_3O_4 and g-C_3N_4 and a metal-semiconductor junction between Ag and g-C_3N_4. In this system, Co_3O_4 acted as a hole (h^+) trapping site and Ag served as an electron (e^-) sink, enabling spatial separation of charge carriers. The composites demonstrated higher transient photocurrent responses compared to pure components, indicating rapid separation and transfer of the photogenerated electron-hole pairs. When Ag was further deposited onto the composites, the resulting metal doped ternary compound exhibited the highest photocurrent density[264].

A series of ternary NiAl layered double hydroxide/g-C_3N_4/CQDs photocatalysts has been synthesised for the photoreduction of CO_2 to CO using a hydrothermal method. CQDs with nanometric sizes of 3 to 4 nm were uniformly distributed on the surface, forming tight junctions. This well-dispersed arrangement of CQDs facilitated the transfer of photogenerated charge carriers between interacting heterojunctions, reducing their recombination by effectively enhancing the separation of electron-hole pairs. The photocatalytic performance under full-spectrum irradiation

 doi:10.20944/preprints202604.1590.v1

was significantly improved by CQDs addition, even in the absence of sacrificial reagents or photosensitisers: CO yield of 20.67 μmol g^{-1} h^{-1} was obtained and attributed to a type-II heterojunction for charge transfer[265].

A lead-free double perovskite Cs_2TeBr_6 was combined in a heterojunction with g-C_3N_4. Electrons from g-C_3N_4 naturally migrated across the interface to Cs_2TeBr_6 and this created a space charge layer at the interface, where g-C_3N_4 became positively charged and Cs_2TeBr_6 negatively charged, establishing an internal electric field. The latter drove the photoinduced electrons in the CB of Cs_2TeBr_6 to recombine with the photoinduced holes in the VB of g-C_3N_4. As a result, g-C_3N_4 and Cs_2TeBr_6 were enriched with strong electron and hole concentrations, respectively. This S-scheme charge transfer mechanism offered efficient separation of photoinduced carriers and the retention of the powered redox potentials of the hybrid material[266].

A two-step hydrothermal calcination tandem synthesis strategy was introduced, involving the incorporation of CQDs into g-C_3N_4 to produce ultra-thin nanosheets. This approach ensured the creation of a heterojunction with a thin structure, increased surface area and improved crystallinity. The integration of CQDs triggered a structural reconfiguration in g-C_3N_4, which revealed abundant built-in electric fields on its surface and enhanced the optical properties of CQD/g-C_3N_4, reducing charge recombination and improving electron exchange efficiency, which accelerated the photocatalytic reduction process. The CO productivity resulted 48 μmol g^{-1} h^{-1}, three times higher than that of pure g-C_3N_4[267].

A durable S-scheme heterojunction was created, consisting of 3D ZnO hollow spheres encased by 2D g-C_3N_4 layers. The electrostatic attraction between the components aided in the exfoliation of the g-C_3N_4 layers and enhanced the overall stability of the photocatalyst framework. The g-C_3N_4/ZnO photocatalyst achieved a CH_4 production rate approximately 40 times higher than pure ZnO and 7 times higher than pure g-C_3N_4. This improvement was due to the extended light absorption and reduced charge carrier recombination. Additionally, EPR was employed, beyond conventional methods, to investigate charge transfer within the S-scheme heterojunction. A noticeable shift in the relevant EPR band was observed after forming the g-C_3N_4/ZnO heterostructure, demonstrating the occurrence of electron transfer[268].

2D/2D g-C_3N_4/Bi_4TaO_8Cl heterojunction catalysts were prepared using an electrostatic self-assembly method in an acidic solution. The charge separation efficiency was demonstrated by higher photocurrent density of the composite than that of Bi_4TaO_8Cl and g-C_3N_4, suggesting that the formation of the heterojunction enhanced the separation of photogenerated electrons. Additionally, a sharp increase in photocurrent was observed for upon illumination. This occurred because photogenerated electrons and holes transferred to and accumulated on the surfaces of Bi_4TaO_8Cl and g-C_3N_4, where they then recombined with species in the electrolyte, resulting in a decrease in photocurrent. The photocatalytic performance of a sample with top-to-top facet coupling surpassed that of lateral-top combination, emphasising the additional significance of facet coupling[269].

The simultaneous proton reduction to H_2 and CO_2 reduction to CO was observed upon irradiation of a hybrid photocatalytic system comprising a black phosphorus/Co@C_3N_4 heterojunction. Specific H_2/CO syngas ratios ranging from 1 to 5 were achieved by adjusting the black phosphorus loading in the system, with a linear increase in the H_2/CO ratio. The most effective formulation produced 69 μmol g^{-1} h^{-1} with a syngas ratio of 2 . Moreover, the addition of $CoCl_2$ enhanced the H_2 production, providing an alternative method to control H_2/CO syngas ratios using lower black phosphorus loading[270].

g-C_3N_4 nanosheets were chosen as the primary photocatalyst, onto which rod-like CeO_2 and rGO were deposited to create a 2D-1D-2D sandwich photocatalyst structure. The photocatalytic CO_2 reduction tests demonstrated that the construction of a multi-interface S-scheme structure significantly enhanced electron transfer efficiency, which was crucial for improving CO_2 photoreduction efficiency. Additionally, the S-scheme electron transfer mode maximised the redox potential of the charge carriers. The integration of rGO introduced various contact interfaces across different dimensionalities (2D-1D; 1D-2D; 2D-2D), serving as electron transfer channels that further

 doi:10.20944/preprints202604.1590.v1

boosted electron transfer efficiency and CO_2 adsorption capacity. Moreover, the π-π conjugated structure of CN enhanced the photogenerated process of π-electrons. This was hypothesised as: after excitation, electrons in the CB of CN can transfer to the surface of rGO via a Schottky-like barrier at the 2D–2D π–π conjugated interface. Additionally, a portion of the electrons from the CB of CeO_2 can rapidly recombine with the photogenerated holes in the VB of CN through the 1D–2D interfacial contact and another fraction of electrons from the CB of CeO_2 can migrate to the rGO surface across a 1D–2D Schottky-like barrier interface[235].

A cascade Z-scheme g-C_3N_4/$BiVO_4$ heterojunction has been engineered through dual modifications involving phosphates and Ag nanoclusters for CO_2 reduction in pure water. Phosphates were incorporated at the interface using a simple impregnation method. At the same time, Ag nanoclusters were deposited on the CN surface via a light-induced in-situ deposition technique under a low-temperature environment created with liquid N_2. The optimised heterojunction achieved a CO production rate of approximately 48 μmol g^{-1} with 97% selectivity, representing a 24-fold increase if compared to pristine $BiVO_4$. When the two single semiconductors were excited under light illumination, electrons in the CB of $BiVO_4$ rapidly recombined with holes in the VB of CN, aided by the phosphate interfacial modification, following the Z-scheme charge transfer pathway. The Ag nanoclusters captured the electrons separated in the CB of CN. The strong affinity of CO_2 for Ag and its subsequent activation significantly promoted the production of COOH* intermediates. Additionally, the enhanced CO desorption properties of the modified Ag contributed to high selectivity in CO conversion[238].

Carbonised pomelo peel was utilised as a waste biomass precursor to construct a ternary heterojunction with carbon nitride, including BiOClBr nanosheets enriched with V_O), rich in N and O vacancy defects through secondary calcination combined with *in situ* growth. Under visible light irradiation, the CO production rate reached 22.9 μmol g^{-1} h^{-1}. Importantly, this heterojunction also demonstrated CO_2 reduction capability under infrared light, with a CO productivity of 3.28 μmol g^{-1} h^{-1}, indicating its potential for effective sunlight utilisation. The formation of the heterojunction and the introduction of defect-induced donor energy levels created a built-in internal electric field and an interfacial electron transfer channel, which enhanced the separation and movement of photogenerated electrons. The 3D porous structure of the biomass derived carbonaceous material and its biomimetic flower-like morphology extended the spectral absorption range. It also acted as an electron acceptor, photothermal cooperative centre and CO_2 adsorption activation site, contributing to an improved internal electric field[271].

An S-scheme composite was developed by in-situ growing tetragonal α-Ag_2MoO_4 nanoparticles, sized between 5 and 30 nm, onto ultrathin porous g-C_3N_4 nanosheets. The nanosheets effectively supported the nanoparticles, forming a composite and enhancing charge separation within the carbon nitride material, while preserving the strong redox capability of the composite and offering increased availability of adsorption sites for CO_2. CO and CH_4 productivities resulted 6.98 and 0.38 μmol g^{-1} h^{-1}, respectively[272].

A composite consisting of Au nanoparticles modifying hexagonal g-C_3N_4 tubes, g-C_3N_4 and CdS was developed and the incorporation of nanotubes enhanced the dispersion of the catalyst during the photocatalytic process. The addition of Au nanoparticles improved the photoelectric conversion efficiency of the g-C_3N_4/CdS type II heterojunction and increased the separation efficiency of photogenerated carriers within the composite. In CO_2 photoreduction experiments, the yields of CO and CH_4 were approximately 55.4 μmol g^{-1} and 8.6 μmol g^{-1}, respectively, after 4 hours of UV-Vis light exposure, ca. five times greater than that of the nanotubes/g-C_3N_4 composite, with appropriate stability[273].

$ZnIn_2S_4$ nanosheets were also incorporated onto hexagonal g-C_3N_4 tubes using an in-situ growth method. The composite demonstrated CO production rate of 883 μmol g^{-1} h^{-1} and an apparent quantum efficiency of 8.9% for CO at 420 nm, which was approximately 13 times and 2.4 times higher than that of the two pristine materials, respectively. This was attributed to the hierarchical structure of the composite, which significantly improved light absorption and reduced electron migration

 doi:10.20944/preprints202604.1590.v1

distance and to the S-scheme heterojunction, which facilitated the efficient migration and separation of photogenerated electron-hole pairs[274].

A hollow spherical Z-scheme SnS_2/g-C_3N_4/C photocatalyst was developed using a morphology-inherited strategy. Biomass mabospores served as both the precursor for creating the hollow spherical structure and the carbon source. The g-C_3N_4 and SnS_2 nanosheets were tightly anchored onto the surface of the mabospores-derived carbon spheres. This Z-scheme heterostructure demonstrated a 5.5-fold increase in activity for CO_2 photoreduction to CO, achieving a productivity of 40.86 μmol g^{-1} h^{-1}. Experimental and theoretical calculations revealed that the enhanced photocatalytic activity of the composite was due to the development of an internal electric field between g-C_3N_4 and SnS_2, and to the reduction of the energy barrier for generating the essential COOH* intermediate during CO_2 reduction[275].

Hydroxyl-modified g-C_3N_4/flower-like $Bi_2O_2CO_3$ composites with covalently bonded heterointerfaces were prepared using a direct mechanical mixing method. These composites demonstrated activity under visible light, with a CO productivity of 26.69 μmol g^{-1} h^{-1}. Additionally, the photocatalyst maintained stability over four cycles. OH, groups played critical roles in enhancing CO_2 photoreduction for the synthesised heterojunction photocatalyst. They modified the surface charge of g-C_3N_4, allowing it to be uniformly deposited onto the surface through electrostatic attraction, which led to a consistent heterostructure. These groups facilitated the formation of covalent Bi–O–C bonds between CN and bismuth oxycarbonate, thereby significantly improving the migration of photogenerated carriers across the two phases. The interaction between Bi^{3+} ions and OH groups promoted the formation of numerous stable V_O on the bismuth oxycarbonate surface, enhancing light absorption and charge separation. In addition, OH modification increased the photocatalyst's surface affinity, leading to greater adsorption of CO_2 and H_2O molecules and effectively driving the photocatalytic reactions[276].

A versatile strategy based on CQDs was employed to induce a confined co-assembly process, enabling the integration of ultrafine WO_3/CQDs with g-C_3N_4 and resulting in the formation of a compact S-scheme heterojunction. Operating without the need for sacrificial reagents, the optimised photocatalyst exhibited a high selectivity of 99.5% toward CO production, reaching a maximum productivity of 31 μmol g^{-1} h^{-1} in a gas–solid phase reaction system. It was concluded that the CQDs played a crucial role in the precise, quantum-sized assembly of high-density WO_3 nanocrystals on the g-C_3N_4 matrix surface, preventing aggregation, they served as efficient hole reservoirs, capturing and quenching more photo-induced holes from the valence band of WO_3. This process synergistically enhanced the S-scheme interfacial charge transport between the reduction photocatalyst g-C_3N_4 and the oxidation photocatalyst WO_3. Furthermore, in situ FTIR and DFT simulations revealed that the regulated electronic structure, resulting from the strong interactions within the heterostructure, promoted the adsorption and activation of CO_2 molecules[277].

An ultrathin dimensionally matched S scheme Bi_3NbO_7/g-C_3N_4 heterostructure was designed, enabling highly selective photocatalytic CO_2 reduction to CH_4, as confirmed by ^{13}C isotopic measurements. The optimised sample exhibited a CH_4 productivity of 38 μmol g^{-1} h^{-1}. Additionally, it remained stable after 10 reaction cycles and 40 hours of simulated solar irradiation without any sacrificial reagents. The Bi_3NbO_7/g-C_3N_4 composites achieved 90% selectivity for CH_4 production over CO. Since CO_2 adsorption was crucial for effective photoreduction, the CO_2 adsorption isotherms of the composite material revealed higher CO_2 adsorption capacity compared to the single semiconductors[278].

A Z-scheme g-C_3N_4/ß-Bi_2O_3 heterojunction photocatalyst was proposed, being formed through the self-assembly of nitrogen-vacant g-C_3N_4 nanosheets and ß-Bi_2O_3 micro-flowers. This system achieved CO evolution rate of 30.56 μmol g^{-1} h^{-1} under simulated solar light, without the need for any cocatalysts or sacrificial agents. The enhanced CO_2 photoreduction activity was attributed to the distinctive Z-scheme charge transfer mechanism and efficient surface nitrogen vacancy sites. Detailed mechanistic analyses revealed that the Z-scheme heterojunction facilitated electron accumulation in C_3N_4 while keeping holes in ß-Bi_2O_3, significantly improving the separation of photogenerated

 doi:10.20944/preprints202604.1590.v1

carriers. Additionally, the unique nitrogen vacancy sites stabilised the *COOH intermediates, reducing the most energy-intensive step in converting *COOH to *CO, which resulted in a more favourable free energy profile for the CO_2 photocatalytic process[279].

A heterojunction photocatalyst composed of electrochemically exfoliated graphene and g-C_3N_4 was developed with varying graphene loadings through an impregnation-calcination process. Their performance in CO_2 photoreduction was assessed in a continuous-flow reactor under visible light irradiation. The results showed that the most effective photocatalyst, with 0.075 EG-CN, achieved the highest CH_4 production rate of 21.32 μmol g^{-1} h^{-1} after 6 hours of light irradiation. Characterisation analyses demonstrated that incorporating graphene into the photocatalyst improved visible light absorption and accelerated the transfer and separation of photogenerated electron-hole pairs[280].

A surface-modified heterojunction composite of g-C_3N_4 on faceted ZnSe was designed to improve the transfer of photogenerated electrons (e^-) and holes (h^+) between the two semiconductors. The products of reaction were CO, H_2 and CH_4 under UV–visible light over 6 hours. In the proposed mechanism, photogenerated holes moved from the VB of ZnSe to the VB of g-C_3N_4, while electrons migrated from the CB of g-C_3N_4 to the one of ZnSe[281].

The ternary composite catalyst g-C_3N_4/Ti_3C_2/$MoSe_2$ was synthesised using a hydrothermal method, retuning CO and CH_4 productivities of 29.87 and 17.94 μmol g^{-1} h^{-1}, respectively. The enhanced catalytic performance was primarily attributed to the full-spectrum optical absorption, resulting from its integration with $MoSe_2$ materials. The formation of the g-C_3N_4/$MoSe_2$ S-scheme heterojunction further improved the efficiency by offering multiple pathways for photogenerated charge migration. Additionally, the inclusion of Ti_3C_2 contributed abundant active sites for the CO_2 catalytic reaction, and its excellent electrical conductivity facilitated the efficient transfer of photogenerated electrons and holes[282].

A S-scheme CeO_2/g-C_3N_4 heterojunction was developed using a two-step calcination method. This heterojunction demonstrated the ability to regulate CO/H_2 ratios in syngas from 1:0.16 to 1:3. The optimal composite achieved CO and H_2 production rates of 1169.56 μmol g^{-1} h^{-1} and 429.12 μmol g^{-1} h^{-1}, respectively. As shown in Figure 28, electrons migrated from the VB to the CB as expected upon irradiation. Simultaneously, a photosensitiser, $[Ru(bpy)_3]^{2+*}$ in its excited state, underwent metal-to-ligand charge transfer and was reductively quenched by triethanolamine (TEOA), forming the reduced species $[Ru(bpy)_3]^+$. The electrons from $[Ru(bpy)_3]^+$ were then transferred to the CB of CN, restoring $[Ru(bpy)_3]^{2+}$ to its initial state. Driven by a built-in electric field, some electrons on the CB of CeO_2 were captured by Ce^{4+} ions, reducing them to Ce^{3+}, while others moved to holes in the valence band of CN and recombined with them. The remaining photogenerated electrons in the CB of CN possessed enhanced reduction activity. These electrons were exploited by the CO_2 adsorbed on the catalyst surface, some of which were indirectly provided through the photosensitised electron transfer mediated by $[Ru(bpy)_3]Cl_2 \cdot 6H_2O$, and reacted with protons supplied from TEOA as a sacrificial agent to produce CO. Meanwhile, the holes in the VB of CeO_2 oxidized TEOA to $TEOA^{+}$[233].

 doi:10.20944/preprints202604.1590.v1

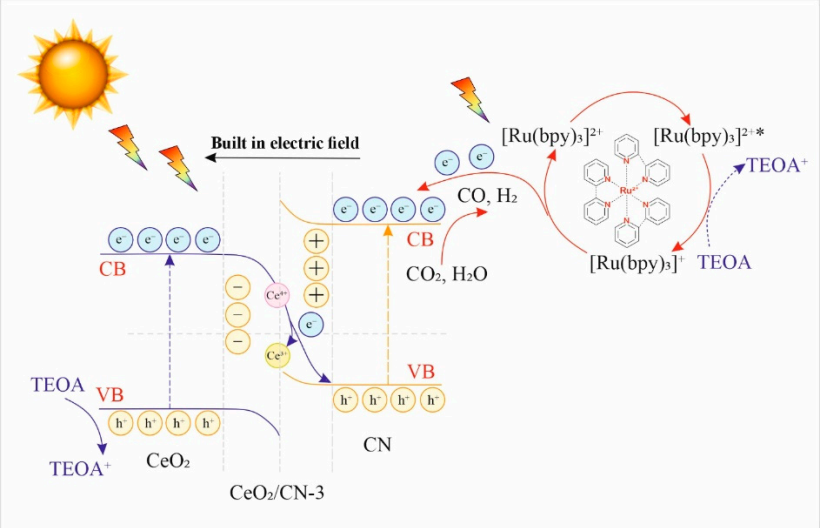

Figure 28. Proposed mechanism of CO_2 photoreduction over S-scheme CeO_2/g-C_3N_4. Readapted from[233].

The photocatalytic conversion of CO_2 and H_2O using an externally reflected photoreactor has been studied on an rGO-bridged g-C_3N_4/ZnV_2O_6 S-scheme heterojunction. The 4% rGO-bridged g-C_3N_4/ZnV_2O_6 (1:1) nanocomposite achieved the highest CH_3OH yield, reaching 6246.1 μmol g_{cat}^{-1}. This yield was 1.34 and 1.51 times greater than that of the g-C_3N_4/ZnV_2O_6 (1:1) and ZnV_2O_6 photocatalysts, respectively[236]. Incorporating rGO into the g-C_3N_4/ZnV_2O_6 nanocomposite formed an S-scheme heterojunction that enhanced solar fuel production by improving charge separation. rGO acted as a mediator, facilitating electron transfer between g-C_3N_4 and ZnV_2O_6. This g-C_3N_4/rGO/ZnV_2O_6 structure promoted faster electron transport from the ZnV_2O_6 CB to the g-C_3N_4 VB due to lower electrical resistance at the rGO/ZnV_2O_6 and rGO/g-C_3N_4 interfaces compared to g-C_3N_4/ZnV_2O_6 alone.

An urchin-like g-C_3N_4/NiAl layered double hydroxide heterojunction was formed using a self-sacrificing template method. The hollow core was made of g-C_3N_4 nanoparticles, on which NiAl nanoplates grew in situ. The photocatalytic CO production rate of g-C_3N_4/NiAl reached 27.02 μmol g^{-1} h^{-1}, which was 4.8 times higher than that of pure g-C_3N_4 and 7.2 times higher than NiAl alone. The spiny surface and hollow structure of g-C_3N_4/NiAl provided a large specific surface area, enhancing mass transfer and reactant capture. Additionally, the charge transfer between the components improved the separation of photogenerated charge carriers, leading to more efficient photon utilisation[283].

An innovative 2D/2D Schottky junction photocatalyst was developed, consisting of $Ti_3C_2T_x$ modified defective g C_3N_4 nanosheets with carbon vacancies ($Ti_3C_2T_x$/Vc CN), prepared via a self-assembly technique. In the $Ti_3C_2T_x$/Vc-CN system, energy disorder drove the dissociation of excitons into free charge carriers within the carbon vacancy defect states, resulting in the generation of more photogenerated carriers for the photocatalytic CO_2 reduction reaction. Given the lower Fermi energy level of $Ti_3C_2T_x$ compared to Vc-CN, the photogenerated electrons transferred from Vc-CN to $Ti_3C_2T_x$ due to the formation of a Schottky junction, further enhancing charge separation efficiency. This charge transfer led to electron accumulation on the $Ti_3C_2T_x$ surface, which was beneficial for converting CO_2 to CO. The combined effects of improved exciton dissociation and directional charge transfer, induced by the Schottky junction in the 2D/2D $Ti_3C_2T_x$/Vc-CN junction catalysts, worked together to enhance photocatalytic CO_2 reduction activity[284].

The photocatalytic CO_2 reduction and electron transfer mechanisms in the $Ti_3C_2T_x$/Vc-CN system are presented in Figure 29, where (a) shows the photocatalytic CO_2 reduction process under light irradiation and (b) illustrates the electron transfer mechanism in the heterostructure.

 doi:10.20944/preprints202604.1590.v1

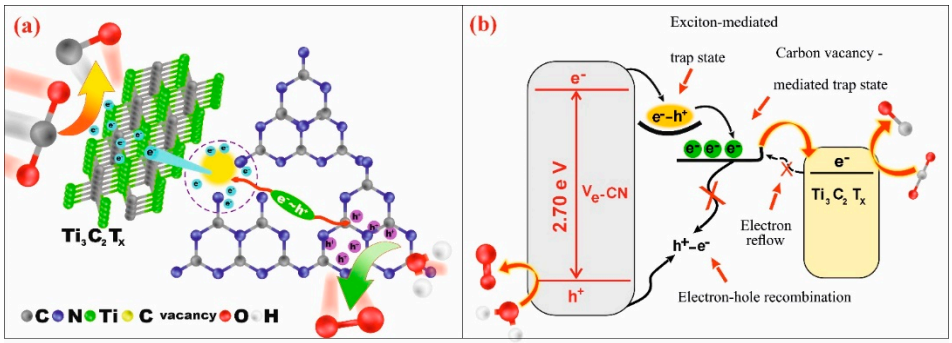

Figure 29. Photocatalytic CO_2 and electron transfer mechanism reduction process of Ti_3C_2Tx/Vc-CN. (a) photocatalytic CO_2 reduction process under light irradiation; (b) electron transfer mechanism in the heterostructure. Readapted from[284].

A study was reported regarding the development of a well-designed 2D/1D g-C_3N_4/CeO_2 visible-light-driven photocatalyst using a straightforward method. The binary photocatalyst demonstrated outstanding photocatalytic degradation performance, achieving a 99.07% removal rate of RhB within 120 minutes and a rate constant (k) of 0.0361 min^{-1}, which remained above 95% over four cycles. Remarkably, it showed high activity in converting CO_2 to CH_4 rather than CO during CO_2 photoreduction. The CH_4 productivity reached 14.63 μmol g^{-1} h^{-1}, which was 26.13 times higher than the CO generation rate of 0.56 μmol g^{-1} h^{-1}. This exceptional activity could be attributed to the well-matched band gaps of CeO_2 and g-C_3N_4, which provided favourable thermodynamics for both the built-in electric field and the S-scheme mechanism. Consequently, carriers involved in the S-scheme transfer process exhibited enhanced oxidation-reduction capabilities and a more effective separation rate[74].

Direct Z-scheme catalysts, consisting of graphitic carbon nitride (g-C_3N_4) nanosheets decorated with three-dimensional ordered macroporous WO_3, were produced using an in-situ colloidal crystal template method. The photonic crystal structure enhanced visible light absorption and improved light energy utilisation. The Z-scheme architecture effectively boosted the separation efficiency of photogenerated electron-hole pairs, with a CO production rate of 48.7 μmol g^{-1} h^{-1}. The electron transfer pathway in the photocatalyst was also discussed[234].

A type-II heterojunction of $Zn_{0.2}Cd_{0.8}S$/g-C_3N_4 nanocomposites for CO_2 photoreduction to produce CH_3OH was prepared using a combination of sonication and hydrothermal methods. Due to the enhanced photoelectric performance provided by the heterojunction, an optimised sample with a g-C_3N_4 to ZnCdS/CN mass ratio of 30% exhibited a CH_3OH production rate of 11.5 ± 0.3 μmol g^{-1} h^{-1}, 2.6 times higher than that of $Zn_{0.2}Cd_{0.8}S$ and 2.7 times higher than that of g-C_3N_4. The activity and photostability were attributed to the formed heterojunction, that also reduced photocorrosion[285].

A 2D/2D Nb_2O_5/g-C_3N_4 S-scheme heterojunction photocatalyst was successfully developed using a in situ calcination method from a niobic acid/urea precursor for gas-solid CO_2 reduction reactions. Under simulated solar irradiation, the optimised sample achieved total C1 product yields (CH_4 and CO) that were 6.7 times and 5.3 times higher than those produced by pristine Nb_2O_5 and g-C_3N_4 nanosheets, respectively, without the need for sacrificial agents or co-catalysts. This was primarily attributed to the close Nb-O-C charge transfer bridge and to the 2D/2D interface contact[286].

A plasma-assisted strategy was used to construct a g-C_3N_4/Bi/CQDs heterojunction with efficient charge separation and active for CO_2 reduction. The CQDs, enriched with various functional groups, played a key role in the in-situ confinement of plasmonic Bi species, leading to a high-density and uniform distribution of Bi/CQDs closely anchored on the surface of g-C_3N_4 nanomeshes. These embedded plasmonic quantum dots, characterised by high electrical conductivity, enhanced light absorption and promoted the generation of additional hot carriers, thereby improving the overall photocatalytic performance. Importantly, the built-in electric field, driven by differences in work function, effectively directed hot electrons from the Bi clusters to the CB of g-C_3N_4, while photoinduced holes in both the Bi clusters and g-C_3N_4 were directed into adjacent CQDs reservoirs

 doi:10.20944/preprints202604.1590.v1

through multiple interfacial charge transfer channels. This arrangement resulted in photocatalytic activity and recyclability for CO_2-to-CO conversion. Specifically, the optimised photocatalyst achieved the highest CO reduction yield of 22.7 μmol g^{-1} h^{-1}, which was 15.4 times higher than that of pristine g-C_3N_4[287].

In another study, a series of catalysts composed of hollow spherical Bi_2MoO_6 and ultrathin g-C_3N_4 were synthesised using a co-solvothermal method. The g-C_3N_4 component enhanced visible light absorption and reactant adsorption. The presence of variable valence molybdenum ions (Mo^{5+}/Mo^{6+}) on the surface of Bi_2MoO_6 helped reduce electrochemical impedance and improve the separation and transfer of photogenerated electron-hole pairs. Notably, the optimal catalyst, with an 18.87% Mo^{5+}/(Mo^{5+}+Mo^{6+}) ratio, achieved the highest CO production of 139.50 μmol with 96.88% CO selectivity. In-situ DRIFTS analysis revealed that visible light irradiation promoted the formation of COOH* species from CO_2 and HCO_3^-. DFT calculations confirmed that the activation energy for converting COOH* to CO* species, the rate-limiting step, was lowered by the Z-scheme heterojunction formed in the g-C_3N_4/Bi_2MoO_6 catalysts, facilitating the selective production of CO through CO_2 photoconversion[288].

Various Z-scheme photocatalysts, specifically γ-Fe_2O_3/g-C_3N_4 composites, were synthesised using straightforward methods such as calcination and impregnation-precipitation. The catalytic performance of these materials was tested for CO_2 photoreduction in the gas phase, where methane was the primary product, and no CO was detected. The highest CH_4 productivity was 2.9×10^2 μmol g^{-1} h^{-1} (pay attention to the values mistakenly written in the abstract with misinterpretation of the numbers reported in their own Figure) greater than that of bulk g-C_3N_4, but by far lower than reasonable benchmarks[289].

Reaching high-efficiency and long-term CO_2 photoreduction in an aqueous environment remained a challenge for $CsPbBr_3$-based catalysts due to their limited moisture resistance. To address this, multifunctional melamine foam and g-C_3N_4 were chosen to modify $CsPbBr_3$ for CO_2 reduction in pure H_2O. The 3D structure of the foam supported $CsPbBr_3$, preventing its degradation from direct contact with water. Additionally, the high porosity enhanced H_2O evaporation, facilitating better mixing of CO_2 with water vapor. The composite achieved a productivity of 975.57 μmol g^{-1} h^{-1}, with an electron consumption rate of 2571.27 μmol g^{-1} h^{-1}. Moreover, the strong surface hydrophobicity and excellent photothermal properties resulted in stable photocatalytic activity, with no significant reduction in CO and CH_4 yields after continuous operation for 76 hours[290].

The Z-scheme $LaCoO_3$/g-C_3N_4 heterojunction has been explored for its effectiveness in the photoinduced reduction of CO_2 into CO and CH_4. In this heterojunction, $LaCoO_3$ was uniformly distributed within the g-C_3N_4 nanotexture, facilitating electron-hole separation due to strong interfacial interaction. CO productivity was 135.2 μmol g^{-1} h^{-1} when 15% $LaCoO_3$ was loaded onto g-C_3N_4, representing a 1.2 increase compared to using either pure $LaCoO_3$ and g-C_3N_4. Similarly, CH_4 production improved with respect to single semiconductors alone[31].

Carbon doped In_2O_3 hollow tubular structures were synthesised by calcining MIL-68(In) as a sacrificial template, followed by combination with g-C_3N_4 through a hydrothermal process to form a C-In_2O_3/g-C_3N_4 heterojunction. The hollow tubular design, carbon doping and type-II heterojunction of C-In_2O_3/g-C_3N_4 enhanced light absorption and promoted the separation of photogenerated electron-hole pairs, thereby significantly improving the photocatalytic CO_2 reduction activity. Among the variants, C-In_2O_3/g-C_3N_4-5 demonstrated the highest CO_2 reduction efficiency, achieving CO production at 153.42 μmol g^{-1} h^{-1} and CH_4 production at 110.31 μmol g^{-1} h^{-1}[291].

g-C_3N_4/$W_{18}O_{49}$ nanocomposites were synthesised through a solvothermal method for solar-driven CO_2 photoreduction. The g-C_3N_4 sheets were found to enhance the dispersibility of $W_{18}O_{49}$ while ensuring good contact between them. Photo/electrochemical measurements indicated that the g-C_3N_4-$W_{18}O_{49}$ heterojunction effectively promoted the separation and migration of photoinduced charges, leading to its improved activity[292].

A van der Waals heterojunction was constructed between two-dimensional materials, namely layered Bi_3O_4Cl and g-C_3N_4. The weak van der Waals interactions within the Bi_3O_4Cl/g-C_3N_4

 doi:10.20944/preprints202604.1590.v1

composite enabled the formation of a moderate bandgap and an internal electric field, which contributed to the efficient separation of photogenerated electron–hole pairs. As a result, the Bi_3O_4Cl/g-C_3N_4 heterostructure exhibited enhanced photocatalytic CO_2 reduction performance when compared to the individual Bi_3O_4Cl and g-C_3N_4 components. The optimised Bi_3O_4Cl/20%g-C_3N_4 composite achieved the CO and CH_4 production rates of 6.6 and 1.9 μmol g^{-1} h^{-1}, respectively[293].

Defective g-C_3N_4/CeO_2 heterojunctions were developed to enhance the photocatalytic reduction of CO_2. The incorporation of g-C_3N_4 into CeO_2 created additional V_O, providing a more stable environment for electron supply and reducing the rate of photogenerated electron-hole recombination. Additionally, CO_2-TPD analysis indicated that light increased the CO_2 adsorption capacity of the composite catalyst, further enhancing its catalytic activity. The productivity of pure CO yield for a 5 wt% g-C_3N_4/CeO_2 composite was 45.66 μmol g^{-1} in 6h, 25 times greater than that of pure CeO_2. This composite also exhibited good cyclic stability and high selectivity, with CO identified as the primary product through in-situ infrared analysis. The improved charge separation and reduced free energy of CO_2 reduction contributed to the enhanced CO_2 conversion efficiency[294].

The activity of bare graphitic carbon nitride in the photocatalytic reduction of CO_2 was comparable with the photocatalysts based on TiO_2, despite the very remarkable advantage of being active under solar light. In contrast, when these two materials were coupled and a heterojunction was formed, the C_3N_4 sheets provided the sites for the adsorption of CO_2, while the presence of TiO_2 mitigated the high recombination rate of the former material by enhancing the separation of the charges long enough for the reaction to occur[60]. The results obtained at 18 bar, pH 14, with 31 mg L^{-1} of photocatalyst and 1.67 g L^{-1} of Na_2SO_3 after 6 h of reaction are presented in Figure 30.

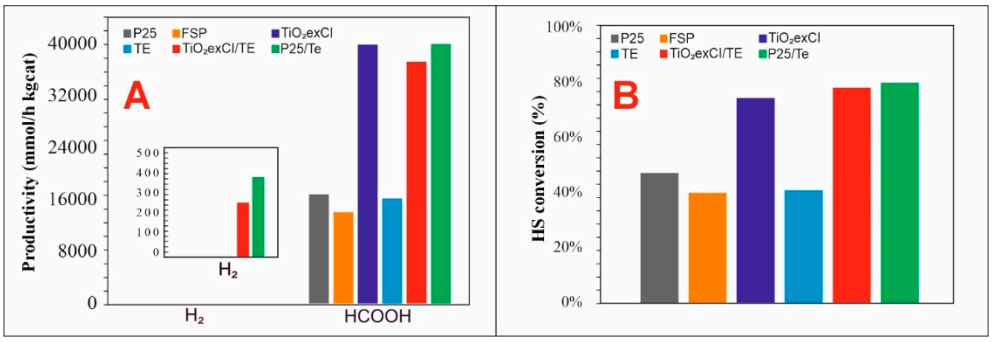

Figure 30. H_2 and HCOOH productivity and hole scavenger conversion for the different photocatalysts: (a) productivity results and (b) hole scavenger consumption for the different photocatalysts (TE = thermally exfoliated C_3N_4; P25 = TiO_2 P25 from Evonik; FSP = TiO_2 prepared by flame spray pyrolysis) Readapted from[60].

6. Quantification of stored energy as a mean to compare different results

Given the widely different reaction conditions and materials, a real comparison between the produced materials is almost impossible, as clearly visible from the above reported widely spread claims. In order to comparatively understand the success of such measures, some quantifiers have been recently suggested to have a practical sizing of the efficiency of the process to compare different solutions[20, 23, 63].

One may calculate first the amount of energy stored in the produced products based on the LHV (or HHV), the lower or higher heating values of the products. This levels off the comparison between cases in which multiple products are formed or where the productivity is stated differently, according to **equations 6.1 to 6.3.**

$$Stored\ power\ \left(\frac{MJ}{day\ kg_{cat}}\right) = Productivity\left(\frac{kg}{day\ kg_{cat}}\right) \times LHV\ or\ HHV\left(\frac{MJ}{kg}\right) \quad Equation\ (6.1)$$

 doi:10.20944/preprints202604.1590.v1

The exposed surface of the photoreactor is a measure of the average area that exposes the catalyst. This is simply calculated as equal to the surface of catalytic layers in the case they are immobilised on well defined supports (e.g. glass sheets). Otherwise, for slurry reactors it is calculated differently depending on the reactor geometry and lamp position. In case of reactors irradiated from top the exposed area is assumed as the top cross section of the reactor, receiving light. In case of reactors containing an immersed lamp (in axial position), it is considered as the logarithmic mean between the lamp surface and of the reactor surface.

Figure 31 presents the calculation of the exposed photoreactor area for slurry photoreactors with an immersion lamp. A_{mlg} corresponds to the logarithmic mean between the cylindrical surface of the photoreactor, considering its internal diameter ($A_{reactor} = \pi D_{reactor} L$), and that of the lamp ($A_{lamp} = \pi D_{lamp} L$). The logarithmic mean is calculated as $A_{mlg} = (A_{reactor} - A_{lamp}) / \ln(A_{reactor} / A_{lamp})$.

$$Incident\ light\ \left(\frac{MJ}{day\ kg_{cat}}\right) = Irradiance\ \left(\frac{MJ}{day\ m^2}\right) \times Exp.photoreactor\ surf.\left(\frac{m^2}{kg_{cat}}\right) \qquad Equation\ (6.2)$$

Finally, the efficiency of the reaction is calculated as the ratio between the stored power and incident energy. Variations of this calculation to cope with the effective fraction of light absorbed by the photocatalyst, based on its absorption edge are discussed in the same references.

$$\eta = \frac{Stored\ power\left(\frac{MJ}{day\ kg_{cat}}\right)}{Incident\ light\ \left(\frac{MJ}{day\ kg_{cat}}\right)} \qquad Equation\ (6.3)$$

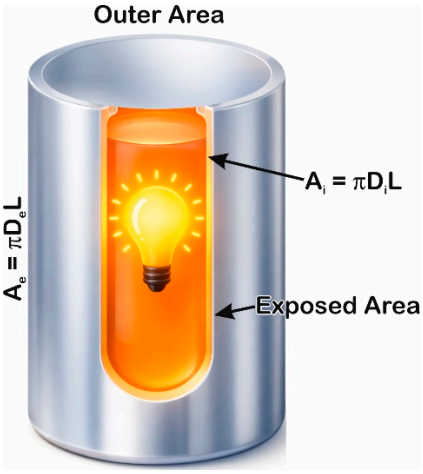

Figure 31. Photoreactor Exposed Area.

7. Conclusion and future perspectives

Many research works have been done till now and still working to improve the performance of photocatalysts, mostly TiO_2 and g-C_3N_4, for photoreduction of CO_2. However, there are still a lot of issues that need to be resolved for the practical application of the photocatalysts to efficiently use sunlight and CO_2 to produce hydrocarbon fuels. The suggestions that can be applied are below.

A significant challenge is producing a cost-effective synthesis approach that produces enough photocatalysts. Future studies should focus on creating novel synthesis methods that make use of inexpensive, ecologically friendly and non-toxic precursors to create recyclable photocatalyst materials.

Light absorption is the first step in photocatalysis and higher absorption causes higher electron-hole carriers production on the photocatalytic surface, which improves photocatalytic CO_2 reduction.

 doi:10.20944/preprints202604.1590.v1

Therefore, a key point in the process of producing solar fuels is improving visible light harvesting and/or increasing the intensity of irradiance, e.g. using solar concentrators.

The performance of a photocatalyst for the reduction of CO_2 also depends on the charge separation process. After the generation, the electron and hole must be successfully separated and transferred to the surface of the photocatalyst to begin the redox reaction cycle. If this process is not completed as quickly as possible, the charge carriers will recombine. Most of the published research used noble metals as a co-catalyst to boost charge separation efficiency, however, these metals are expensive and should match the band energy of the semiconductor.

More recently, different semiconductors have been coupled through properly engineered junctions to catch two birds with one stone. On one hand, the junction may function to improve the charge separation, on the other, depending on the band gap and band potentials, both the materials can be visible sensitive, improving at once also the light harvesting properties of the hybrid photocatalyst.

The ability of photocatalytic CO_2 reduction to generate a variety of products is typically acknowledged. Product selectivity is crucial for understanding the CO_2 photoreduction mechanism and optimising targeted products. Both the redox potential and the surface density of electrons have a significant impact on the end product. Therefore, by modifying the TiO_2 band structure, the selectivity of photocatalytic CO_2 reduction can be managed. Furthermore, developing a rigorous, dependable, and stable system for product detection is fundamental. This aspect also hinders direct comparison between published results. Therefore, it is suggested that future publications may report stored energy and the efficiency calculated as here proposed, through a very pragmatic definition, to allow a safe comparison of the results.

Lastly, other than the synthesis and modification of photocatalyst material, photocatalytic reactor design and understanding the reaction mechanism are other major areas CO_2 photoreduction to hydrocarbon fuels. The yield of CO_2 photoreduction is primarily influenced by the photocatalytic material, used photoreactor and the intensity of incident light. However, appropriate reactor design and greater comprehension of the reaction mechanism in a photoreactor are the only ways to enhance the performance of photocatalytic materials.

The overall yield of the products has been the focus of CO_2 photoreduction investigations to date. To have a better understanding of the mechanism on the TiO_2 surface detailed research still should be done. On a large scale, the mechanism, reaction routes and kinetic and thermodynamic studies of the CO_2 photoreduction process are still poorly understood.

More research will lead to a better knowledge of the process occurring on the surface of the photocatalyst, which will improve the utilisation of photocatalytic materials. A complete and sustainable research on photocatalytic CO_2 reduction to solar fuels and its potential as a long-term strategy to address greenhouse gas emissions and energy production will be provided by this kind of approach.

Author Contributions: Conceptualization, M.S., G.R. and I.R.; resources, M.S., G.R. and I.R; data curation, W.C., S.N.D. and S.T.; writing—original draft preparation, S.N.D. and S.T.; writing—review and editing, F.M., M.S., G.R. and I.R.; visualization, W.C.; supervision, F.M. and I.R.; project administration, M.S., G.R. and I.R.; funding acquisition, M.S., G.R. and I.R.. All authors have read and agreed to the published version of the manuscript.

Funding: The authors gratefully acknowledge the financial contribution of Fondazione Cariplo through the grant 2021-0855 – "SCORE - Solar Energy for Circular CO_2 Photoconversion and Chemicals Regeneration", funded in the frame of the Circular Economy call 2021. The authors kindly acknowledge MUR for funding the project "P20227LB45 - SCORE2 - Solar-driven COnveRsion of CO2 with HP-HT photorEactor" within PIANO NAZIONALE DI RIPRESA E RESILIENZA (PNRR) Missione 4 "Istruzione e Ricerca" - Componente C2 Investimento 1.1, "Fondo per il Programma Nazionale di Ricerca e Progetti di Rilevante Interesse Nazionale (PRIN)". I. Rossetti acknowledges Università degli Studi di Milano for support through the grant PSR 2021 - GSA - Linea 6 "One Health Action Hub: University Task Force for the resilience of territorial ecosystems". W. Cardoso, G. Ramis and I. Rossetti gratefully acknowledge the Italian Ministry of Environment and Energy

 doi:10.20944/preprints202604.1590.v1

Sustainability (MASE, formerly MITE) for funding the project "RSH2A_000018 - Stoccaggio e distribuzione di idrogeno attraverso una strategia power-to-gas/gas-to-power con cattura ed utilizzo completi del carbonio - Hydrogen storage and distribution through power-to-gas strategy, with full carbon capture and utilization-CUP: F57G25000180006" in the frame the European Union Next-GenerationEU, Piano Nazionale di Ripresa e Resilienza (PNRR) – Missione 2 "Rivoluzione verde e transizione ecologica", Componente 2 "Energia rinnovabile, idrogeno, rete e mobilità sostenibile", Investimento 3.5 "Ricerca e sviluppo sull'idrogeno" (bando A). This manuscript reflects only the authors' views and opinions, neither the European Union nor the European Commission can be considered responsible for them.

Data Availability Statement: No original data is available for this work.

Conflicts of Interest: The authors declare no conflicts of interest".

References

1. *https://www.iea.org/reports/co2-emissions-in-2023*. https://www.iea.org/reports/co2-emissions-in-2023 (accessed).
2. (2)*https://data.worldbank.org/indicator/EN.ATM.CO2E.KT?end=2014&start=1990*. https://data.worldbank.org/indicator/EN.ATM.CO2E.KT?end=2014&start=1990 (accessed).
3. *https://www.epa.gov/ghgemissions/global-greenhouse-gas-emissions-data*. https://www.epa.gov/ghgemissions/global-greenhouse-gas-emissions-data (accessed).
4. (4)*https://www.eia.gov/outlooks/ieo/pdf/IEO2021_ReleasePresentation.pdf*. . https://www.eia.gov/outlooks/ieo/pdf/IEO2021_ReleasePresentation.pdf. (accessed).
5. Shen, N.; Wang, Y.; Peng, H.; Hou, Z. Renewable Energy Green Innovation, Fossil Energy Consumption, and Air Pollution—Spatial Empirical Analysis Based on China. *Sustainability* **2020**, *12* (16). DOI: 10.3390/su12166397.
6. Ramos, J. L.; Pakuts, B.; Godoy, P.; Garcia-Franco, A.; Duque, E. Addressing the energy crisis: using microbes to make biofuels. *Microb Biotechnol* **2022**, *15* (4), 1026–1030. DOI: 10.1111/1751-7915.14050 From NLM Medline.
7. Cardoso, W.; Locateli, B.; Ribeiro, D. S.; Machado, T. A. P.; Cometti, E. A.; Conti, L. Engineering, Carbon Credits and Climate Change: Challenges and Opportunities. In *Smart Innovation, Systems and Technologies*, Vol. 497; 2026.
8. Usubharatana, P.; McMartin, D.; Veawab, A.; Tontiwachwuthikul, P. Photocatalytic Process for CO2 Emission Reduction from Industrial Flue Gas Streams. *Industrial & Engineering Chemistry Research* **2006**, *45* (8), 2558–2568. DOI: 10.1021/ie0505763.
9. Izumi, Y. Recent advances in the photocatalytic conversion of carbon dioxide to fuels with water and/or hydrogen using solar energy and beyond. *Coordination Chemistry Reviews* **2013**, *257* (1), 171–186. DOI: 10.1016/j.ccr.2012.04.018.
10. Shehzad, N.; Tahir, M.; Johari, K.; Murugesan, T.; Hussain, M. A critical review on TiO2 based photocatalytic CO2 reduction system: Strategies to improve efficiency. *Journal of CO2 Utilization* **2018**, *26*, 98–122. DOI: 10.1016/j.jcou.2018.04.026.
11. Šalipur, H.; Fronczak, M.; Prašnikar, A.; Kamal, K. M.; Mudrinić, T.; Hadnađev-Kostić, M.; Likozar, B.; Dostanić, J.; Lončarević, D. Metal doped TiO2 decorated carbon nanostructured materials as an emerging photocatalysts for solar fuels production. *Catalysis Today* **2024**, *436*. DOI: 10.1016/j.cattod.2024.114724.
12. Nogia, P.; Sidhu, G. K.; Mehrotra, R.; Mehrotra, S. Capturing atmospheric carbon: biological and nonbiological methods. *International Journal of Low-Carbon Technologies* **2016**, *11* (2), 266–274. DOI: 10.1093/ijlct/ctt077.
13. Alonso, A.; Moral-Vico, J.; Abo Markeb, A.; Busquets-Fite, M.; Komilis, D.; Puntes, V.; Sanchez, A.; Font, X. Critical review of existing nanomaterial adsorbents to capture carbon dioxide and methane. *Sci Total Environ* **2017**, *595*, 51–62. DOI: 10.1016/j.scitotenv.2017.03.229 From NLM PubMed-not-MEDLINE.
14. Chen, X.; Shen, S.; Guo, L.; Mao, S. S. Semiconductor-based photocatalytic hydrogen generation. *Chem Rev* **2010**, *110* (11), 6503–6570. DOI: 10.1021/cr1001645 From NLM PubMed-not-MEDLINE.

 doi:10.20944/preprints202604.1590.v1

15. Meryem, S. S.; Nasreen, S.; Siddique, M.; Khan, R. An overview of the reaction conditions for an efficient photoconversion of CO2. *Reviews in Chemical Engineering* **2018**, *34* (3), 409–425. DOI: 10.1515/revce-2016-0016.
16. Meylan, F. D.; Moreau, V.; Erkman, S. CO2 utilization in the perspective of industrial ecology, an overview. *Journal of CO2 Utilization* **2015**, *12*, 101–108. DOI: 10.1016/j.jcou.2015.05.003.
17. Wang, Z.; Hong, J.; Ng, S.-F.; Liu, W.; Huang, J.; Chen, P.; Ong, W.-J. Recent Progress of Perovskite Oxide in Emerging Photocatalysis Landscape: Water Splitting, CO₂ Reduction, and N₂ Fixation. *Acta Physico Chimica Sinica* **2020**, *0* (0), 2011033–2011030. DOI: 10.3866/pku.Whxb202011033.
18. Kamat, P. V. Manipulation of Charge Transfer Across Semiconductor Interface. A Criterion That Cannot Be Ignored in Photocatalyst Design. *J Phys Chem Lett* **2012**, *3* (5), 663–672. DOI: 10.1021/jz201629p From NLM PubMed-not-MEDLINE.
19. Li, K.; An, X.; Park, K. H.; Khraisheh, M.; Tang, J. A critical review of CO2 photoconversion: Catalysts and reactors. *Catalysis Today* **2014**, *224*, 3–12. DOI: 10.1016/j.cattod.2013.12.006.
20. Rossetti, I.; Bahadori, E.; Tripodi, A.; Villa, A.; Prati, L.; Ramis, G. Conceptual design and feasibility assessment of photoreactors for solar energy storage. *Solar Energy* **2018**, *172*, 225–231. DOI: 10.1016/j.solener.2018.02.056.
21. Ilenia Rossetti; Elnaz Bahadori; Antonio Tripodi; Ramis, G. Modelling of Photoreactors for Water Treatment *CHEMICAL ENGINEERING TRANSACTIONS* **2019**, *74*, 289–294. DOI: 10.3303/CET1974049.
22. Gianguido Ramis; Elnaz Bahadori; Rossetti, I. Photoreactors Design for Hydrogen Production. *CHEMICAL ENGINEERING TRANSACTIONS* **2019**, *74*, 481–486. DOI: 10.3303/CET1974081.
23. I. Rossetti; E. Bahadori; A. Tripodi; Ramis, G. Feasibility Assessment of Photoreactors for Water Treatment. In *DGMK - Challenges for Petrochemicals and Fuels: Integration of Value Chains and Energy Transition*, 2018.
24. Degerli, S. N.; Gramegna, A.; Tommasi, M.; Ramis, G.; Rossetti, I. Reactor and Plant Designs for the Solar Photosynthesis of Fuels. *Energies* **2024**, *17* (13). DOI: 10.3390/en17133112.
25. Wu, J.; Liu, J.; Xia, W.; Ren, Y.-Y.; Wang, F. Advances on Photocatalytic CO₂ Reduction Based on CdS and CdSe Nano-Semiconductors. *Acta Physico Chimica Sinica* **2020**, *0* (0), 2008043–2008040. DOI: 10.3866/pku.Whxb202008043.
26. Khan, A. A.; Tahir, M. Recent advancements in engineering approach towards design of photo-reactors for selective photocatalytic CO2 reduction to renewable fuels. *Journal of CO2 Utilization* **2019**, *29*, 205–239. DOI: 10.1016/j.jcou.2018.12.008.
27. Fan, W.; Zhang, Q.; Wang, Y. Semiconductor-based nanocomposites for photocatalytic H2 production and CO2 conversion. *Phys Chem Chem Phys* **2013**, *15* (8), 2632–2649. DOI: 10.1039/c2cp43524a From NLM PubMed-not-MEDLINE.
28. Li, Z.; Luo, W.; Zhang, M.; Feng, J.; Zou, Z. Photoelectrochemical cells for solar hydrogen production: current state of promising photoelectrodes, methods to improve their properties, and outlook. *Energy Environ. Sci.* **2013**, *6* (2), 347–370. DOI: 10.1039/c2ee22618a.
29. Kubacka, A.; Fernandez-Garcia, M.; Colon, G. Advanced nanoarchitectures for solar photocatalytic applications. *Chem Rev* **2012**, *112* (3), 1555–1614. DOI: 10.1021/cr100454n From NLM PubMed-not-MEDLINE.
30. Benson, E. E.; Kubiak, C. P.; Sathrum, A. J.; Smieja, J. M. Electrocatalytic and homogeneous approaches to conversion of CO2 to liquid fuels. *Chem Soc Rev* **2009**, *38* (1), 89–99. DOI: 10.1039/b804323j From NLM PubMed-not-MEDLINE.
31. Madi, M.; Tahir, M. Highly stable LaCoO3 perovskite supported g-C3N4 nanotextures with proficient charges migration for visible light CO2 photoreduction to CO and CH4. *Materials Science in Semiconductor Processing* **2022**, *142*. DOI: 10.1016/j.mssp.2022.106517.
32. Wang, J.; Liu, W.; Luo, G.; Li, Z.; Zhao, C.; Zhang, H.; Zhu, M.; Xu, Q.; Wang, X.; Zhao, C.; et al. Synergistic effect of well-defined dual sites boosting the oxygen reduction reaction. *Energy & Environmental Science* **2018**, *11* (12), 3375–3379. DOI: 10.1039/c8ee02656d.
33. Zhang, X.; Han, F.; Shi, B.; Farsinezhad, S.; Dechaine, G. P.; Shankar, K. Photocatalytic conversion of diluted CO2 into light hydrocarbons using periodically modulated multiwalled nanotube arrays. *Angew Chem Int Ed Engl* **2012**, *51* (51), 12732–12735. DOI: 10.1002/anie.201205619 From NLM PubMed-not-MEDLINE.

 doi:10.20944/preprints202604.1590.v1

34. Rossetti, I.; Villa, A.; Compagnoni, M.; Prati, L.; Ramis, G.; Pirola, C.; Bianchi, C. L.; Wang, W.; Wang, D. CO2 photoconversion to fuels under high pressure: effect of TiO2 phase and of unconventional reaction conditions. *Catalysis Science & Technology* **2015**, *5* (9), 4481–4487. DOI: 10.1039/c5cy00756a.
35. Bertuletti, M.; Fumagalli, A.; Gramegna, A.; Tommasi, M.; Ramis, G.; Rossetti, I. Hole Scavenger Role during CO2 Photoreduction: Toward a New Hybrid Homogeneous/Heterogeneous Process. *ACS Sustainable Chemistry & Engineering* **2026**. DOI: 10.1021/acssuschemeng.6c01242.
36. Park, H.; Park, Y.; Kim, W.; Choi, W. Surface modification of TiO2 photocatalyst for environmental applications. *Journal of Photochemistry and Photobiology C: Photochemistry Reviews* **2013**, *15*, 1–20. DOI: 10.1016/j.jphotochemrev.2012.10.001.
37. Kumar, S. G.; Devi, L. G. Review on modified TiO2 photocatalysis under UV/visible light: selected results and related mechanisms on interfacial charge carrier transfer dynamics. *J Phys Chem A* **2011**, *115* (46), 13211–13241. DOI: 10.1021/jp204364a From NLM PubMed-not-MEDLINE.
38. Daghrir, R.; Drogui, P.; Robert, D. Modified TiO2 For Environmental Photocatalytic Applications: A Review. *Industrial & Engineering Chemistry Research* **2013**, *52* (10), 3581–3599. DOI: 10.1021/ie303468t.
39. Pelaez, M.; Nolan, N. T.; Pillai, S. C.; Seery, M. K.; Falaras, P.; Kontos, A. G.; Dunlop, P. S. M.; Hamilton, J. W. J.; Byrne, J. A.; O'Shea, K.; et al. A review on the visible light active titanium dioxide photocatalysts for environmental applications. *Applied Catalysis B: Environmental* **2012**, *125*, 331–349. DOI: 10.1016/j.apcatb.2012.05.036.
40. Dozzi, M. V.; Selli, E. Doping TiO2 with p-block elements: Effects on photocatalytic activity. *Journal of Photochemistry and Photobiology C: Photochemistry Reviews* **2013**, *14*, 13–28. DOI: 10.1016/j.jphotochemrev.2012.09.002.
41. Zhang, H.; Chen, G.; Bahnemann, D. W. Photoelectrocatalytic materials for environmental applications. *Journal of Materials Chemistry* **2009**, *19* (29). DOI: 10.1039/b821991e.
42. Xu, Z.; Cui, Y.; Young, D. J.; Wang, J.; Li, H.-Y.; Bian, G.-Q.; Li, H.-X. Combination of Co2+-immobilized covalent triazine framework and TiO2 by covalent bonds to enhance photoreduction of CO2 to CO with H2O. *Journal of CO2 Utilization* **2021**, *49*. DOI: 10.1016/j.jcou.2021.101561.
43. Barrocas, B. T.; Ambrozova, N.; Koci, K. Photocatalytic Reduction of Carbon Dioxide on TiOHeterojunction Photocatalysts-A Review. *Materials (Basel)* **2022**, *15* (3). DOI: 10.3390/ma15030967 From NLM PubMed-not-MEDLINE.
44. Zhou, S.; Liu, Y.; Li, J.; Wang, Y.; Jiang, G.; Zhao, Z.; Wang, D.; Duan, A.; Liu, J.; Wei, Y. Facile in situ synthesis of graphitic carbon nitride (g-C3N4)-N-TiO2 heterojunction as an efficient photocatalyst for the selective photoreduction of CO2 to CO. *Applied Catalysis B: Environmental* **2014**, *158-159*, 20–29. DOI: 10.1016/j.apcatb.2014.03.037.
45. Dai, Y.-M.; Li, C.-Y.; Ting, W.-H.; Jehng, J.-M. Plasmon Ag/AgVO3/ TiO2-nanowires S-scheme heterojunction photocatalyst for CO2 reduction. *Journal of Environmental Chemical Engineering* **2022**, *10* (3). DOI: 10.1016/j.jece.2022.108045.
46. Wang, Y.; Wang, Q.; Zhan, X.; Wang, F.; Safdar, M.; He, J. Visible light driven type II heterostructures and their enhanced photocatalysis properties: a review. *Nanoscale* **2013**, *5* (18), 8326–8339. DOI: 10.1039/c3nr01577g From NLM PubMed-not-MEDLINE.
47. Selinsky, R. S.; Ding, Q.; Faber, M. S.; Wright, J. C.; Jin, S. Quantum dot nanoscale heterostructures for solar energy conversion. *Chem Soc Rev* **2013**, *42* (7), 2963–2985. DOI: 10.1039/c2cs35374a From NLM PubMed-not-MEDLINE.
48. Abdali, S. A.; Al-Temimei, F. A.; Al-Abbas, S. S. Computational design of D-π-A dyes for improved photovoltaic performance: a DFT approach. *Journal of Computational Electronics* **2024**, *23* (2), 209–223. DOI: 10.1007/s10825-024-02131-2.
49. Fang, S.; Rahaman, M.; Bharti, J.; Reisner, E.; Robert, M.; Ozin, G. A.; Hu, Y. H. Photocatalytic CO2 reduction. *Nature Reviews Methods Primers* **2023**, *3* (1). DOI: 10.1038/s43586-023-00243-w.
50. Kaneco, S.; Shimizu, Y.; Ohta, K.; Mizuno, T. Photocatalytic reduction of high pressure carbon dioxide using TiO2 powders with a positive hole scavenger. *Journal of Photochemistry and Photobiology A: Chemistry* **1998**, *115* (3), 223–226. DOI: 10.1016/s1010-6030(98)00274-3.

 doi:10.20944/preprints202604.1590.v1

51. Bahadori, E.; Tripodi, A.; Villa, A.; Pirola, C.; Prati, L.; Ramis, G.; Rossetti, I. High Pressure Photoreduction of CO2: Effect of Catalyst Formulation, Hole Scavenger Addition and Operating Conditions. *Catalysts* **2018**, *8* (10). DOI: 10.3390/catal8100430.
52. M. Tommasi; F. Conte; G. Ramis; I. Rossetti. Artificial Photosynthesis: The Role of Photocatalysis in the Energy Transition. In *The Role of Catalysis for the Energy-Transition, DGMK*, 2022; Vol. 2022, pp 134–151. DOI: https://dgmk.de/app/uploads/2022/11/DGMK_2022-3.pdf.
53. Tommasi, M.; Conte, F.; Alam, M. I.; Ramis, G.; Rossetti, I. Highly Efficient and Effective Process Design for High-Pressure CO2 Photoreduction over Supported Catalysts. *Energies* **2023**, *16* (13). DOI: 10.3390/en16134990.
54. Tommasi, M.; Gramegna, A.; Degerli, S. N.; Galli, F.; Rossetti, I. High-Pressure CO2 Photoreduction, Flame Spray Pyrolysis and Type-II Heterojunctions: A Promising Synergy. *Catalysts* **2025**, *15* (4). DOI: 10.3390/catal15040383.
55. Tang, J.; Durrant, J. R.; Klug, D. R. Mechanism of photocatalytic water splitting in TiO2. Reaction of water with photoholes, importance of charge carrier dynamics, and evidence for four-hole chemistry. *J Am Chem Soc* **2008**, *130* (42), 13885–13891. DOI: 10.1021/ja8034637 From NLM PubMed-not-MEDLINE.
56. Tang, J.; Cowan, A. J.; Durrant, J. R.; Klug, D. R. Mechanism of O2 Production from Water Splitting: Nature of Charge Carriers in Nitrogen Doped Nanocrystalline TiO2 Films and Factors Limiting O2 Production. *The Journal of Physical Chemistry C* **2011**, *115* (7), 3143–3150. DOI: 10.1021/jp1080093.
57. Liu, Z.; Yi, T.; Huang, C.; Choy, K.-L.; Liu, C. Thermodynamic and kinetics of hydrogen photoproduction enhancement by concentrated sunlight with CO2 photoreduction by heterojunction photocatalysts. *Energy and AI* **2021**, *6*. DOI: 10.1016/j.egyai.2021.100102.
58. Yoshino, S.; Takayama, T.; Yamaguchi, Y.; Iwase, A.; Kudo, A. COReduction Using Water as an Electron Donor over Heterogeneous Photocatalysts Aiming at Artificial Photosynthesis. *Acc Chem Res* **2022**, *55* (7), 966–977. DOI: 10.1021/acs.accounts.1c00676 From NLM Medline.
59. Conte, F.; Rossetti, I.; Ramis, G.; Vaulot, C.; Hajjar-Garreau, S.; Bennici, S. Low Metal Loading (Au, Ag, Pt, Pd) Photo-Catalysts Supported on TiOfor Renewable Processes. *Materials (Basel)* **2022**, *15* (8). DOI: 10.3390/ma15082915 From NLM PubMed-not-MEDLINE.
60. Conte, F.; García-López, E. I.; Marcì, G.; Bianchi, C. L. M.; Ramis, G.; Rossetti, I. Carbon Nitride-Based Catalysts for High Pressure CO2 Photoreduction. *Catalysts* **2022**, *12* (12). DOI: 10.3390/catal12121628.
61. Rossetti, I.; Conte, F.; Tripodi, A.; Ramis, G. Photocatalysis with Nanoparticles for Environmental Applications: Reactor Design Issues. In *Nanostructured Catalysts for Environmental Applications*, 2021; pp 241–271.
62. Rossetti, I. Flame-based synthesis of oxide nanoparticles for photocatalytic applications. In *Materials Science in Photocatalysis*, 2021; pp 63–82.
63. Conte, F.; Tripodi, A.; Rossetti, I.; Ramis, G. Feasibility Study of the Solar-Promoted Photoreduction of CO2 to Liquid Fuels with Direct or Indirect Use of Renewable Energy Sources. *Energies* **2021**, *14* (10). DOI: 10.3390/en14102804.
64. Bahadori, E.; Tripodi, A.; Villa, A.; Pirola, C.; Prati, L.; Ramis, G.; Dimitratos, N.; Wang, D.; Rossetti, I. High pressure CO2photoreduction using Au/TiO2: unravelling the effect of co-catalysts and of titania polymorphs. *Catalysis Science & Technology* **2019**, *9* (9), 2253–2265. DOI: 10.1039/c9cy00286c.
65. Compagnoni, M.; Villa, A.; Bahdori, E.; Morgan, D. J.; Prati, L.; Dimitratos, N.; Rossetti, I.; Ramis, G. Surface Probing by Spectroscopy on Titania-Supported Gold Nanoparticles for a Photoreductive Application. *Catalysts* **2018**, *8* (12). DOI: 10.3390/catal8120623.
66. Rossetti, I.; Villa, A.; Pirola, C.; Prati, L.; Ramis, G. A novel high-pressure photoreactor for CO2photoconversion to fuels. *RSC Adv.* **2014**, *4* (55), 28883–28885. DOI: 10.1039/c4ra03751k.
67. Conte, F.; Villa, A.; Prati, L.; Pirola, C.; Bennici, S.; Ramis, G.; Rossetti, I. Effect of Metal Cocatalysts and Operating Conditions on the Product Distribution and the Productivity of the COPhotoreduction. *Ind Eng Chem Res* **2022**, *61* (8), 2963–2972. DOI: 10.1021/acs.iecr.1c02514 From NLM PubMed-not-MEDLINE.
68. Galli, F.; Compagnoni, M.; Vitali, D.; Pirola, C.; Bianchi, C. L.; Villa, A.; Prati, L.; Rossetti, I. CO2 photoreduction at high pressure to both gas and liquid products over titanium dioxide. *Applied Catalysis B: Environmental* **2017**, *200*, 386–391. DOI: 10.1016/j.apcatb.2016.07.038.

 doi:10.20944/preprints202604.1590.v1

69. Chávez-Caiza, J.; Fernández-Catalá, J.; Navlani-García, M.; Lousada, C. M.; Berenguer-Murcia, Á.; Cazorla-Amorós, D. Unveiling the effect of sacrificial agent amount in the CO2 photoreduction performed in a flow reactor. *Journal of CO2 Utilization* **2024**, *83*, 102818. DOI: https://doi.org/10.1016/j.jcou.2024.102818.
70. Kitjanukit, N.; Neamsung, W.; Karawek, A.; Lertthanaphol, N.; Chongkol, N.; Hiramatsu, K.; Sekiguchi, T.; Pornsuwan, S.; Sakurai, T.; Jonglertjunya, W.; et al. Effects of alcohols as sacrificial reagents on a copper-doped sodium dititanate nanosheets/graphene oxide photocatalyst in COphotoreduction. *RSC Adv* **2024**, *14* (38), 27980–27989. DOI: 10.1039/d4ra04585h From NLM PubMed-not-MEDLINE.
71. Patulski, P.; Fernández-Catalá, J.; Berenguer-Murcia, Á.; Cazorla-Amorós, D. Mechanochemistry as an efficient method in Cu/P25 photocatalysts synthesis for CO2 photoreduction. *Journal of CO2 Utilization* **2025**, *94*. DOI: 10.1016/j.jcou.2025.103055.
72. Chávez-Caiza, J.; Fernández-Catalá, J.; Navlani-García, M.; Lousada, C. M.; Berenguer-Murcia, Á.; Cazorla-Amorós, D. Unveiling the effect of sacrificial agent amount in the CO2 photoreduction performed in a flow reactor. *Journal of CO2 Utilization* **2024**, *83*. DOI: 10.1016/j.jcou.2024.102818.
73. de Jesus Martins, N.; Gomes, I. C. H.; da Silva, G. T. S. T.; Torres, J. A.; Avansi, W.; Ribeiro, C.; Malagutti, A. R.; Mourão, H. A. J. L. Facile preparation of ZnO:g-C3N4 heterostructures and their application in amiloride photodegradation and CO2 photoreduction. *Journal of Alloys and Compounds* **2021**, *856*. DOI: 10.1016/j.jallcom.2020.156798.
74. Wang, D.; Miao, C.; Li, H.; Yu, B.; Wang, W.; Wang, Y.; Che, G.; Liu, C.; Hu, B. A directional built-in electric field assisted 2D/1D g-C3N4/CeO2 S-scheme heterojunction for efficient RhB degradation and highly-selective CO2 photoreduction. *Materials Research Bulletin* **2024**, *170*. DOI: 10.1016/j.materresbull.2023.112552.
75. Bratovčić, A.; Tomašić, V. Design and Development of Photocatalytic Systems for Reduction of CO2 into Valuable Chemicals and Fuels. *Processes* **2023**, *11* (5). DOI: 10.3390/pr11051433.
76. Liu, Z.; Li, J.; Chen, Z.; Li, M.; Wang, L.; Wu, S.; Zhang, J. Photocatalytic conversion of carbon dioxide on triethanolamine: Unheeded catalytic performance of sacrificial agent. *Applied Catalysis B: Environmental* **2023**, *326*. DOI: 10.1016/j.apcatb.2022.122338.
77. Olivo, A.; Ghedini, E.; Signoretto, M.; Compagnoni, M.; Rossetti, I. Liquid vs. Gas Phase CO2 Photoreduction Process: Which Is the Effect of the Reaction Medium? *Energies* **2017**, *10* (9). DOI: 10.3390/en10091394.
78. Ao, C. H.; Lee, S. C.; Yu, J. Z.; Xu, J. H. Photodegradation of formaldehyde by photocatalyst TiO2: effects on the presences of NO, SO2 and VOCs. *Applied Catalysis B: Environmental* **2004**, *54* (1), 41–50. DOI: 10.1016/j.apcatb.2004.06.004.
79. Nascimento, V. R. S.; Torres, J. A.; Iga, G. D.; dos Santos, A. L.; Egues, S. M.; Filho, J. B. G.; Ferreira, L. F. R.; Ribeiro, C. CO2 Photoreduction Product Selectivity with TiO2−Cu Nanocatalysts under Different Reaction Media. *ChemCatChem* **2024**, *16* (11). DOI: 10.1002/cctc.202301612.
80. Garvin, M.; Thompson, W. A.; Tan, J. Z. Y.; Kampouri, S.; Ireland, C. P.; Smit, B.; Brookfield, A.; Collison, D.; Negahdar, L.; Beale, A. M.; et al. Highly selective COphotoreduction to CO on MOF-derived TiO(2). *RSC Sustain* **2023**, *1* (3), 494–503. DOI: 10.1039/d2su00082b From NLM PubMed-not-MEDLINE.
81. Núñez, O.; Sattayamuk, D.; Saelee, T.; Yamashita, H.; Kuwahara, Y.; Mori, K.; Praserthdam, P.; Praserthdam, S. A closer look inside TiO2 (P25) photocatalytic CO2/HCO3− reduction with water. Methane rate and selectivity enhancements. *Chemical Engineering Journal* **2021**, *409*. DOI: 10.1016/j.cej.2020.128141.
82. Mgolombane, M.; Bankole, O. M.; Ferg, E. E.; Ogunlaja, A. S. Construction of Co-doped TiO2/rGO nanocomposites for high-performance photoreduction of CO2 with H2O: Comparison of theoretical binding energies and exploration of surface chemistry. *Materials Chemistry and Physics* **2021**, *268*. DOI: 10.1016/j.matchemphys.2021.124733.
83. Torres, J. A.; Nogueira, A. E.; da Silva, G. T. S. T.; Lopes, O. F.; Wang, Y.; He, T.; Ribeiro, C. Enhancing TiO2 activity for CO2 photoreduction through MgO decoration. *Journal of CO2 Utilization* **2020**, *35*, 106–114. DOI: 10.1016/j.jcou.2019.09.008.
84. Ješić, D.; Lašič Jurković, D.; Pohar, A.; Suhadolnik, L.; Likozar, B. Engineering photocatalytic and photoelectrocatalytic CO2 reduction reactions: Mechanisms, intrinsic kinetics, mass transfer resistances,

 doi:10.20944/preprints202604.1590.v1

reactors and multi-scale modelling simulations. *Chemical Engineering Journal* **2021**, *407*. DOI: 10.1016/j.cej.2020.126799.

85. Ma, Y.; Wang, S.; Duan, X. Recent advances in direct gas–solid-phase photocatalytic conversion of CO2 for porous photocatalysts under different CO2 atmospheres. *Chemical Engineering Journal* **2023**, *455*. DOI: 10.1016/j.cej.2022.140654.
86. Das, R.; Chakraborty, S.; Peter, S. C. Systematic Assessment of Solvent Selection in Photocatalytic CO2 Reduction. *ACS Energy Letters* **2021**, *6* (9), 3270–3274. DOI: 10.1021/acsenergylett.1c01522.
87. Lin, J.; Qin, B.; Zhao, G. Effect of solvents on photocatalytic reduction of CO2 mediated by cobalt complex. *Journal of Photochemistry and Photobiology A: Chemistry* **2018**, *354*, 181–186. DOI: 10.1016/j.jphotochem.2017.09.019.
88. Albo, J.; Qadir, M. I.; Samperi, M.; Fernandes, J. A.; de Pedro, I.; Dupont, J. Use of an optofluidic microreactor and Cu nanoparticles synthesized in ionic liquid and embedded in TiO2 for an efficient photoreduction of CO2 to methanol. *Chemical Engineering Journal* **2021**, *404*. DOI: 10.1016/j.cej.2020.126643.
89. Merino-Garcia, I.; García, G.; Hernández, I.; Albo, J. An optofluidic planar microreactor with photoactive Cu2O/Mo2C/TiO2 heterostructures for enhanced visible light-driven CO2 conversion to methanol. *Journal of CO2 Utilization* **2023**, *67*. DOI: 10.1016/j.jcou.2022.102340.
90. Hasanvandian, F.; Zehtab Salmasi, M.; Moradi, M.; Farshineh Saei, S.; Kakavandi, B.; Rahman Setayesh, S. Enhanced spatially coupling heterojunction assembled from CuCo2S4 yolk-shell hollow sphere capsulated by Bi-modified TiO2 for highly efficient CO2 photoreduction. *Chemical Engineering Journal* **2022**, *444*. DOI: 10.1016/j.cej.2022.136493.
91. Ismael, M. A review on graphitic carbon nitride (g-C3N4) based nanocomposites: Synthesis, categories, and their application in photocatalysis. *Journal of Alloys and Compounds* **2020**, *846*. DOI: 10.1016/j.jallcom.2020.156446.
92. Rosales, M.; Zoltan, T.; Yadarola, C.; Mosquera, E.; Gracia, F.; García, A. The influence of the morphology of 1D TiO2 nanostructures on photogeneration of reactive oxygen species and enhanced photocatalytic activity. *Journal of Molecular Liquids* **2019**, *281*, 59–69. DOI: 10.1016/j.molliq.2019.02.070.
93. Huang, C.-y.; Guo, R.-t.; Pan, W.-g.; Tang, J.-y.; Zhou, W.-g.; Liu, X.-y.; Qin, H.; Jia, P.-y. One-dimension TiO2 nanostructures with enhanced activity for CO2 photocatalytic reduction. *Applied Surface Science* **2019**, *464*, 534–543. DOI: 10.1016/j.apsusc.2018.09.114.
94. Camposeco, R.; Castillo, S.; Navarrete, J.; Gomez, R. Synthesis, characterization and photocatalytic activity of TiO2 nanostructures: Nanotubes, nanofibers, nanowires and nanoparticles. *Catalysis Today* **2016**, *266*, 90–101. DOI: 10.1016/j.cattod.2015.09.018.
95. Wu, M.-C.; Hsiao, K.-C.; Chang, Y.-H.; Chan, S.-H. Photocatalytic hydrogen evolution of palladium nanoparticles decorated black TiO 2 calcined in argon atmosphere. *Applied Surface Science* **2018**, *430*, 407–414. DOI: 10.1016/j.apsusc.2017.08.071.
96. Phromma, S.; Wutikhun, T.; Kasamechonchung, P.; Eksangsri, T.; Sapcharoenkun, C. Effect of Calcination Temperature on Photocatalytic Activity of Synthesized TiO2 Nanoparticles via Wet Ball Milling Sol-Gel Method. *Applied Sciences* **2020**, *10* (3). DOI: 10.3390/app10030993.
97. Wetchakun, N.; Incessungvorn, B.; Wetchakun, K.; Phanichphant, S. Influence of calcination temperature on anatase to rutile phase transformation in TiO2 nanoparticles synthesized by the modified sol–gel method. *Materials Letters* **2012**, *82*, 195–198. DOI: 10.1016/j.matlet.2012.05.092.
98. Morawski, A. W.; Kusiak-Nejman, E.; Wanag, A.; Narkiewicz, U.; Edelmannová, M.; Reli, M.; Kočí, K. Influence of the calcination of TiO2-reduced graphite hybrid for the photocatalytic reduction of carbon dioxide. *Catalysis Today* **2021**, *380*, 32–40. DOI: 10.1016/j.cattod.2021.05.017.
99. Chen, M.; Wu, J.; Lu, C.; Luo, X.; Huang, Y.; Jin, B.; Gao, H.; Zhang, X.; Argyle, M.; Liang, Z. Photoreduction of CO2 in the presence of CH4 over g-C3N4 modified with TiO2 nanoparticles at room temperature. *Green Energy & Environment* **2021**, *6* (6), 938–951. DOI: 10.1016/j.gee.2020.07.001.
100. https://www.efsa.europa.eu/it/news/titanium-dioxide-e171-no-longer-considered-safe-when-used-food-additive. (accessed).
101. Oi, L. E.; Choo, M.-Y.; Lee, H. V.; Ong, H. C.; Hamid, S. B. A.; Juan, J. C. Recent advances of titanium dioxide (TiO2) for green organic synthesis. *RSC Advances* **2016**, *6* (110), 108741–108754. DOI: 10.1039/c6ra22894a.

 doi:10.20944/preprints202604.1590.v1

102. Hossen, M. A.; Solayman, H. M.; Leong, K. H.; Sim, L. C.; Yaacof, N.; Abd Aziz, A.; Wu, L.; Monir, M. U. Recent progress in TiO2-Based photocatalysts for conversion of CO2 to hydrocarbon fuels: A systematic review. *Results in Engineering* **2022**, *16*. DOI: 10.1016/j.rineng.2022.100795.
103. Kang, X.; Liu, S.; Dai, Z.; He, Y.; Song, X.; Tan, Z. Titanium Dioxide: From Engineering to Applications. *Catalysts* **2019**, *9* (2). DOI: 10.3390/catal9020191.
104. Malato-Rodríguez, S. Solar Detoxification and Disinfection. In *Encyclopedia of Energy*, 2004; pp 587–596.
105. Tan, H. L.; Abdi, F. F.; Ng, Y. H. Heterogeneous photocatalysts: an overview of classic and modern approaches for optical, electronic, and charge dynamics evaluation. *Chem Soc Rev* **2019**, *48* (5), 1255–1271. DOI: 10.1039/c8cs00882e From NLM PubMed-not-MEDLINE.
106. Ran, J.; Jaroniec, M.; Qiao, S. Z. Cocatalysts in Semiconductor-based Photocatalytic COReduction: Achievements, Challenges, and Opportunities. *Adv Mater* **2018**, *30* (7). DOI: 10.1002/adma.201704649 From NLM PubMed-not-MEDLINE.
107. Byrne, C.; Subramanian, G.; Pillai, S. C. Recent advances in photocatalysis for environmental applications. *Journal of Environmental Chemical Engineering* **2018**, *6* (3), 3531–3555. DOI: 10.1016/j.jece.2017.07.080.
108. Yamada, Y.; Kanemitsu, Y. Determination of electron and hole lifetimes of rutile and anatase TiO2 single crystals. *Applied Physics Letters* **2012**, *101* (13). DOI: 10.1063/1.4754831.
109. Liang, X.; Yu, S.; Meng, B.; Wang, X.; Yang, C.; Shi, C.; Ding, J. Advanced TiO2-Based Photoelectrocatalysis: Material Modifications, Charge Dynamics, and Environmental–Energy Applications. *Catalysts* **2025**, *15* (6). DOI: 10.3390/catal15060542.
110. Li, Z.; Wang, S.; Wu, J.; Zhou, W. Recent progress in defective TiO2 photocatalysts for energy and environmental applications. *Renewable and Sustainable Energy Reviews* **2022**, *156*. DOI: 10.1016/j.rser.2021.111980.
111. Rega, R.; Fioravanti, A.; Hejazi, S. M. H.; Shahrezaei, M.; Kment, S.; Maddalena, P.; Naldoni, A.; Lettieri, S. Charge carrier recombination processes, intragap defect states, and photoluminescence mechanisms in stoichiometric and reduced TiObrookite nanorods: an interpretation scheme through in situ photoluminescence excitation spectroscopy in controlled environment. *Nanoscale* **2024**, *16* (23), 11296–11309. DOI: 10.1039/d4nr00593g From NLM PubMed-not-MEDLINE.
112. Bahadori, E.; Ramis, G.; Rossetti, I. Matching nanotechnologies with reactor scale-up and industrial exploitation. In *Nanomaterials for the Detection and Removal of Wastewater Pollutants*, 2020; pp 407–442.
113. Tseng, I. H.; Wu, J. C. S.; Chou, H.-Y. Effects of sol–gel procedures on the photocatalysis of Cu/TiO2 in CO2 photoreduction. *Journal of Catalysis* **2004**, *221* (2), 432–440. DOI: 10.1016/j.jcat.2003.09.002.
114. Rosario, A. V.; Pereira, E. C. The role of Pt addition on the photocatalytic activity of TiO2 nanoparticles: The limit between doping and metallization. *Applied Catalysis B: Environmental* **2014**, *144*, 840–845. DOI: 10.1016/j.apcatb.2013.07.029.
115. Debeila, M. A.; Raphulu, M. C.; Mokoena, E.; Avalos, M.; Petranovskii, V.; Coville, N. J.; Scurrell, M. S. The influence of gold on the optical properties of sol–gel derived titania. *Materials Science and Engineering: A* **2005**, *396* (1-2), 70–76. DOI: 10.1016/j.msea.2004.12.046.
116. Tasbihi, M.; Kočí, K.; Edelmannová, M.; Troppová, I.; Reli, M.; Schomäcker, R. Pt/TiO2 photocatalysts deposited on commercial support for photocatalytic reduction of CO2. *Journal of Photochemistry and Photobiology A: Chemistry* **2018**, *366*, 72–80. DOI: 10.1016/j.jphotochem.2018.04.012.
117. Liu, Z.; Jia, B.; Zhang, Y.; Haneda, M. Engineering the Metal–Support Interaction on Pt/TiO2 Catalyst to Boost the H2-SCR of NOx. *Industrial & Engineering Chemistry Research* **2020**, *59* (31), 13916–13922. DOI: 10.1021/acs.iecr.0c01792.
118. Kavitha, R.; Kumar, S. G. Review on bimetallic-deposited TiO2: preparation methods, charge carrier transfer pathways and photocatalytic applications. *Chemical Papers* **2019**, *74* (3), 717–756. DOI: 10.1007/s11696-019-00995-4.
119. Zielińska-Jurek, A.; Banadaki, A. D. Progress, Challenge, and Perspective of Bimetallic TiO2-Based Photocatalysts. *Journal of Nanomaterials* **2014**, *2014* (1). DOI: 10.1155/2014/208920.
120. Wang, R.; Wang, C.; Xing, Y.; Zhang, X. Solution Plasma for Surface Design of Advanced Photocatalysts. *Catalysts* **2023**, *13* (7). DOI: 10.3390/catal13071124.

 doi:10.20944/preprints202604.1590.v1

121. An, H. R.; Park, S. Y.; Kim, H.; Lee, C. Y.; Choi, S.; Lee, S. C.; Seo, S.; Park, E. C.; Oh, Y. K.; Song, C. G.; et al. Advanced nanoporous TiO2 photocatalysts by hydrogen plasma for efficient solar-light photocatalytic application. *Sci Rep* **2016**, *6*, 29683. DOI: 10.1038/srep29683 From NLM PubMed-not-MEDLINE.
122. Yu, F.; Wang, C.; Li, Y.; Ma, H.; Wang, R.; Liu, Y.; Suzuki, N.; Terashima, C.; Ohtani, B.; Ochiai, T.; et al. Enhanced Solar Photothermal Catalysis over Solution Plasma Activated TiO(2). *Adv Sci (Weinh)* **2020**, *7* (16), 2000204. DOI: 10.1002/advs.202000204 From NLM PubMed-not-MEDLINE.
123. Zhang, P.; Li, N.; Li, L.; Yu, Y.; Tuerhong, R.; Su, X.; Zhang, B.; Han, L.; Han, Y. g-C(3)N(4)-Based Photocatalytic Materials for Converting COInto Energy: A Review. *Chemphyschem* **2024**, *25* (17), e202400075. DOI: 10.1002/cphc.202400075 From NLM PubMed-not-MEDLINE.
124. Wang, X.; Maeda, K.; Thomas, A.; Takanabe, K.; Xin, G.; Carlsson, J. M.; Domen, K.; Antonietti, M. A metal-free polymeric photocatalyst for hydrogen production from water under visible light. *Nat Mater* **2009**, *8* (1), 76–80. DOI: 10.1038/nmat2317 From NLM PubMed-not-MEDLINE.
125. Alwin, E.; Koci, K.; Wojcieszak, R.; Zielinski, M.; Edelmannova, M.; Pietrowski, M. Influence of High Temperature Synthesis on the Structure of Graphitic Carbon Nitride and Its Hydrogen Generation Ability. *Materials (Basel)* **2020**, *13* (12). DOI: 10.3390/ma13122756 From NLM PubMed-not-MEDLINE.
126. Zhou, Z.; Zhang, Y.; Shen, Y.; Liu, S.; Zhang, Y. Molecular engineering of polymeric carbon nitride: advancing applications from photocatalysis to biosensing and more. *Chem Soc Rev* **2018**, *47* (7), 2298–2321. DOI: 10.1039/c7cs00840f From NLM Medline.
127. Tommasi, M.; Abbasi, E.; Alam, M. I.; Marinotto, D.; Rossetti, I.; Ramis, G. Improving CO2 Photoconversion by Layered Materials: Boosted Optoelectronic Performance and Catalytic Activity of g-C3N4 by Ultrasound Exfoliation. *ChemCatChem* **2025**, *18* (1). DOI: 10.1002/cctc.202402142.
128. Zeng, D.; Wang, X.; Kuai, C.; Jiang, Z.; Guo, Y. CO2 chemisorption and activation on carbon nitride with less amino groups boost CO2 photoreduction. *Catalysis Science & Technology* **2024**, *14* (4), 1052–1061. DOI: 10.1039/d3cy01585h.
129. Fu, Y. S.; Li, J.; Li, J. Metal/Semiconductor Nanocomposites for Photocatalysis: Fundamentals, Structures, Applications and Properties. *Nanomaterials (Basel)* **2019**, *9* (3). DOI: 10.3390/nano9030359 From NLM PubMed-not-MEDLINE.
130. Kamat, P. V. Meeting the Clean Energy Demand: Nanostructure Architectures for Solar Energy Conversion. *The Journal of Physical Chemistry C* **2007**, *111* (7), 2834–2860. DOI: 10.1021/jp066952u.
131. Fujishima, A.; Zhang, X.; Tryk, D. TiO2 photocatalysis and related surface phenomena. *Surface Science Reports* **2008**, *63* (12), 515–582. DOI: 10.1016/j.surfrep.2008.10.001.
132. Sahoo, S. K.; Acharya, L.; Biswal, L.; Priyadarshini, P.; Parida, K. Recent advancements in graphitic carbon nitride based direct Z- and S-scheme heterostructures for photocatalytic H2O2 production. *Inorganic Chemistry Frontiers* **2024**, *11* (16), 4914–4973. DOI: 10.1039/d4qi00950a.
133. Panthi, G.; Park, M. Graphitic Carbon Nitride/Zinc Oxide-Based Z-Scheme and S-Scheme Heterojunction Photocatalysts for the Photodegradation of Organic Pollutants. *Int J Mol Sci* **2023**, *24* (19). DOI: 10.3390/ijms241915021 From NLM Medline.
134. Al Jitan, S.; Palmisano, G.; Garlisi, C. Synthesis and Surface Modification of TiO2-Based Photocatalysts for the Conversion of CO2. *Catalysts* **2020**, *10* (2). DOI: 10.3390/catal10020227.
135. Nematollahi, R.; Ghotbi, C.; Khorasheh, F.; Larimi, A. Ni-Bi co-doped TiO2 as highly visible light response nano-photocatalyst for CO2 photo-reduction in a batch photo-reactor. *Journal of CO2 Utilization* **2020**, *41*. DOI: 10.1016/j.jcou.2020.101289.
136. Reñones, P.; Collado, L.; Iglesias-Juez, A.; Oropeza, F. E.; Fresno, F.; de la Peña O'Shea, V. A. Silver–Gold Bimetal-Loaded TiO2 Photocatalysts for CO2 Reduction. *Industrial & Engineering Chemistry Research* **2020**, *59* (20), 9440–9450. DOI: 10.1021/acs.iecr.0c01034.
137. Zhan, Z.; Wang, H.; Huang, Q.; Li, S.; Yi, X.; Tang, Q.; Wang, J.; Tan, B. Grafting Hypercrosslinked Polymers on TiOSurface for Anchoring Ultrafine Pd Nanoparticles: Dramatically Enhanced Efficiency and Selectivity toward Photocatalytic Reduction of COto CH(4). *Small* **2022**, *18* (1), e2105083. DOI: 10.1002/smll.202105083 From NLM PubMed-not-MEDLINE.

 doi:10.20944/preprints202604.1590.v1

138. Liu, J.; Wang, Y.; Chen, S.; Ye, H.; Xie, Y. Synergy between metal sites and oxygen vacancy for CO2 photoreduction: Activity and stability enhancement. *Separation and Purification Technology* **2024**, *335*. DOI: 10.1016/j.seppur.2023.126161.
139. Durga Devi, A.; Pushpavanam, S.; Singh, N.; Verma, J.; Kaur, M. P.; Roy, S. C. Enhanced methane yield by photoreduction of CO2 at moderate temperature and pressure using Pt coated, graphene oxide wrapped TiO2 nanotubes. *Results in Engineering* **2022**, *14*. DOI: 10.1016/j.rineng.2022.100441.
140. Larimi, A.; Rahimi, M.; Khorasheh, F. Carbonaceous supports decorated with Pt–TiO2 nanoparticles using electrostatic self-assembly method as a highly visible-light active photocatalyst for CO2 photoreduction. *Renewable Energy* **2020**, *145*, 1862–1869. DOI: 10.1016/j.renene.2019.07.105.
141. Lin, L.-Y.; Kavadiya, S.; He, X.; Wang, W.-N.; Karakocak, B. B.; Lin, Y.-C.; Berezin, M. Y.; Biswas, P. Engineering stable Pt nanoparticles and oxygen vacancies on defective TiO2 via introducing strong electronic metal-support interaction for efficient CO2 photoreduction. *Chemical Engineering Journal* **2020**, *389*. DOI: 10.1016/j.cej.2019.123450.
142. Yadav, M.; Basheer, H. S.; Ágfalvi, Á.; Ábrahámné, K. B.; Kiss, J.; Halasi, G.; Sápi, A.; Kukovecz, Á.; Kónya, Z. Noble metals-deposited TiO2 photocatalysts for photoreduction of CO2: Exploration of surface chemistry and a reflection on the importance of wavelength dependence. *Applied Catalysis A: General* **2023**, *668*. DOI: 10.1016/j.apcata.2023.119434.
143. Khatun, F.; Abd Aziz, A.; Sim, L. C.; Monir, M. U. Plasmonic enhanced Au decorated TiO2 nanotube arrays as a visible light active catalyst towards photocatalytic CO2 conversion to CH4. *Journal of Environmental Chemical Engineering* **2019**, *7* (6). DOI: 10.1016/j.jece.2019.103233.
144. Ban, C.; Wang, Y.; Ma, J.; Feng, Y.; Wang, X.; Qin, S.; Jing, S.; Duan, Y.; Zhang, M.; Tao, X.; et al. Metal–oxygen hybridization in Agcluster/TiO2 for selective CO2 photoreduction to CH4. *Chemical Engineering Journal* **2024**, *488*. DOI: 10.1016/j.cej.2024.150845.
145. Wang, X.; Xuan, X.; Wang, Y.; Li, X.; Huang, H.; Zhang, X.; Du, X. Nano-Au-modified TiO2 grown on dendritic porous silica particles for enhanced CO2 photoreduction. *Microporous and Mesoporous Materials* **2021**, *310*. DOI: 10.1016/j.micromeso.2020.110635.
146. Zeng, P.; Liu, H.; Jia, H.; Cai, J.; Deng, X.; Peng, T. In-situ synthesis of single-atom CoN clusters-decorated TiO2 for highly efficient charge separation and CO2 photoreduction. *Applied Catalysis B: Environmental* **2024**, *340*. DOI: 10.1016/j.apcatb.2023.123268.
147. Tang, Q.; Xiong, P.; Wang, H.; Wu, Z. Boosted COphotoreduction performance on Ru-Ti(3)CN MXene-TiOphotocatalyst synthesized by non-HF Lewis acidic etching method. *J Colloid Interface Sci* **2022**, *619*, 179–187. DOI: 10.1016/j.jcis.2022.03.137 From NLM PubMed-not-MEDLINE.
148. Fang, F.; Liu, Y.; Sun, X.; Fu, C.; Prakash Bhoi, Y.; Xiong, W.; Huang, W. TiO2 Facet-dependent reconstruction and photocatalysis of CuOx/TiO2 photocatalysts in CO2 photoreduction. *Applied Surface Science* **2021**, *564*. DOI: 10.1016/j.apsusc.2021.150407.
149. Goto, H.; Masegi, H.; Sadale, S. B.; Noda, K. Intricate behaviors of gas phase CO2 photoreduction in high vacuum using Cu2O-loaded TiO2 nanotube arrays. *Journal of CO2 Utilization* **2022**, *59*. DOI: 10.1016/j.jcou.2022.101964.
150. Torres, J. A.; da Cruz, J. C.; Nogueira, A. E.; da Silva, G. T. S. T.; de Oliveira, J. A.; Ribeiro, C. Role of Cu0-TiO2 interaction in catalyst stability in CO2 photoreduction process. *Journal of Environmental Chemical Engineering* **2022**, *10* (2). DOI: 10.1016/j.jece.2022.107291.
151. Wang, T.; Sun, F.; Liu, S.; Zhuang, G.; Li, B. Dioxygen-enhanced CO2 photoreduction on TiO2 supported Cu single-atom sites. *Applied Catalysis B: Environmental* **2023**, *325*. DOI: 10.1016/j.apcatb.2022.122339.
152. Ibarra-Rodriguez, L. I.; Pantoja-Espinoza, J. C.; Luévano-Hipólito, E.; Garay-Rodríguez, L. F.; López-Ortiz, A.; Torres-Martínez, L. M.; Collins-Martínez, V. H. Formic acid and hydrogen generation from the photocatalytic reduction of CO2 on visible light activated N-TiO2/CeO2/CuO composites. *Journal of Photochemistry and Photobiology* **2022**, *11*. DOI: 10.1016/j.jpap.2022.100125.
153. Yang, G.; Xiong, J.; Lu, M.; Wang, W.; Li, W.; Wen, Z.; Li, S.; Li, W.; Chen, R.; Cheng, G. Co-embedding oxygen vacancy and copper particles into titanium-based oxides (TiO(2), BaTiO(3), and SrTiO(3)) nanoassembly for enhanced COphotoreduction through surface/interface synergy. *J Colloid Interface Sci* **2022**, *624*, 348–361. DOI: 10.1016/j.jcis.2022.05.092 From NLM PubMed-not-MEDLINE.

 doi:10.20944/preprints202604.1590.v1

154. Montalvo, D.; Corro, G.; Bañuelos, F.; Olivares-Xometl, O.; Arellanes, P.; Pal, U. Selective alcohols production through CO2 photoreduction using Co3O4 /TiO2 photocatalyst exploiting synergetic interactions between Ti3+, Co2+ and Co3+. *Applied Catalysis B: Environmental* **2023**, *330*. DOI: 10.1016/j.apcatb.2023.122652.
155. Bai, L.; Li, W.; Chu, X.; Yin, H.; Qu, Y.; Kozlova, E.; Yang, Z.-D.; Jing, L. Effects of nanosized Au on the interface of zinc phthalocyanine/TiO2 for CO2 photoreduction. *Chinese Chemical Letters* **2025**, *36* (2). DOI: 10.1016/j.cclet.2024.109931.
156. Fereidooni, M.; Núñez, O.; Márquez, V.; Paz, C. V.; Salazar Villanueva, M.; Zin Tun, M.; Kanjanaboos, P.; Praserthdam, S.; Praserthdam, P. Effect of substrate conductivity on charge transfer and CO2 photoreduction in water vapor over silica-modified TiO2 films. *Applied Surface Science* **2023**, *611*. DOI: 10.1016/j.apsusc.2022.155595.
157. Sorokina, L.; Savitskiy, A.; Shtyka, O.; Maniecki, T.; Szynkowska-Jozwik, M.; Trifonov, A.; Pershina, E.; Mikhaylov, I.; Dubkov, S.; Gromov, D. Formation of Cu-Rh alloy nanoislands on TiO2 for photoreduction of carbon dioxide. *Journal of Alloys and Compounds* **2022**, *904*. DOI: 10.1016/j.jallcom.2022.164012.
158. Li, R.; Luan, Q.; Dong, C.; Dong, W.; Tang, W.; Wang, G.; Lu, Y. Light-facilitated structure reconstruction on self-optimized photocatalyst TiO2@BiOCl for selectively efficient conversion of CO2 to CH4. *Applied Catalysis B: Environmental* **2021**, *286*. DOI: 10.1016/j.apcatb.2020.119832.
159. Fan, W. K.; Tahir, M.; Alias, H. Visible light promoted low temperature photothermal CO2 methanation over morphologically engineered Ni/TiO2 NWs catalyst. *Materials Today: Proceedings* **2024**, *97*, 9–16. DOI: 10.1016/j.matpr.2023.05.665.
160. Pan, H.; Wang, X.; Xiong, Z.; Sun, M.; Murugananthan, M.; Zhang, Y. Enhanced photocatalytic COreduction with defective TiOnanotubes modified by single-atom binary metal components. *Environ Res* **2021**, *198*, 111176. DOI: 10.1016/j.envres.2021.111176 From NLM Medline.
161. Jin, L.; Shaaban, E.; Bamonte, S.; Cintron, D.; Shuster, S.; Zhang, L.; Li, G.; He, J. Surface Basicity of Metal@TiOto Enhance Photocatalytic Efficiency for COReduction. *ACS Appl Mater Interfaces* **2021**, *13* (32), 38595–38603. DOI: 10.1021/acsami.1c09119 From NLM PubMed-not-MEDLINE.
162. Zhou, Y.; Zhang, Q.; Shi, X.; Song, Q.; Zhou, C.; Jiang, D. Photocatalytic reduction of COinto CHover Ru-doped TiO(2): Synergy of Ru and oxygen vacancies. *J Colloid Interface Sci* **2022**, *608* (Pt 3), 2809–2819. DOI: 10.1016/j.jcis.2021.11.011 From NLM PubMed-not-MEDLINE.
163. Moradi, M.; Khorasheh, F.; Larimi, A. Pt nanoparticles decorated Bi-doped TiO2 as an efficient photocatalyst for CO2 photo-reduction into CH4. *Solar Energy* **2020**, *211*, 100–110. DOI: 10.1016/j.solener.2020.09.054.
164. Lo, A.-Y.; Wang, C.-C.; Huang, J.; Chung, Y.-C.; Chang, Y.-C. Defect-synergetic effect enhanced CO2 photoreduction efficiency of TiO2 nanostructures with Fe dopants. *Journal of Environmental Chemical Engineering* **2024**, *12* (2). DOI: 10.1016/j.jece.2024.112351.
165. Fernández-Catalá, J.; Navlani-García, M.; Berenguer-Murcia, Á.; Cazorla-Amorós, D. Exploring CuxO-doped TiO2 modified with carbon nanotubes for CO2 photoreduction in a 2D-flow reactor. *Journal of CO2 Utilization* **2021**, *54*. DOI: 10.1016/j.jcou.2021.101796.
166. Lo, A.-Y.; Chung, Y.-C.; Xie, P.-J.; Delbari, H.; Yang, Z.-H.; Taghipour, F. Effect of Ag-doping strategies on the Lewis acid/base behavior of mesoporous TiO2 photocatalyst and its performance in CO2 photoreduction. *Applied Materials Today* **2023**, *32*. DOI: 10.1016/j.apmt.2023.101811.
167. Wu, X.; Ren, S.; Hao, W.; Yuan, K.; Guo, H.; Li, Y.; Huang, H.; Xie, R.; Zhong, K.; Yan, W.; et al. Modulating charge separation of Ce–TiO2 aerogel supported on chitosan derived ordered porous carbonaceous frameworks for promoting CO2 photoreduction activity. *Ceramics International* **2024**, *50* (17), 31519–31531. DOI: 10.1016/j.ceramint.2024.05.459.
168. Kang, S.; Hwang, J. rGO-wrapped Ag-doped TiO2 nanofibers for photocatalytic CO2 reduction under visible light. *Journal of Cleaner Production* **2022**, *374*. DOI: 10.1016/j.jclepro.2022.134022.
169. Xu, S. Y.; Shi, W.; Huang, J. R.; Yao, S.; Wang, C.; Lu, T. B.; Zhang, Z. M. Single-cluster Functionalized TiONanotube Array for Boosting Water Oxidation and COPhotoreduction to CH(3)OH. *Angew Chem Int Ed Engl* **2024**, *63* (28), e202406223. DOI: 10.1002/anie.202406223 From NLM PubMed-not-MEDLINE.

 doi:10.20944/preprints202604.1590.v1

170. Singh, S.; Kumar, R.; Pant, K. K.; Kumar, S.; Joshi, D.; Biswas, P. Mechanistic exploration in controlling the product selectivity via metals in TiO2 for photocatalytic carbon dioxide reduction. *Applied Catalysis B: Environment and Energy* **2024**, *352*. DOI: 10.1016/j.apcatb.2024.124054.
171. Li, D.; Li, Q.; Zhou, Y.; Zhang, Q.; Ye, Q.; Yang, R.; Jiang, D. Shaping and Doping Metal-Organic Framework-Derived TiOto Steer the Selectivity of Photocatalytic COReduction toward CH(4). *Inorg Chem* **2024**, *63* (33), 15398–15408. DOI: 10.1021/acs.inorgchem.4c02407 From NLM PubMed-not-MEDLINE.
172. Li, L.; Dai, X.; Lu, M.; Guo, C.; Wabaidur, S. M.; Wu, X.-L.; Lou, Z.; Zhong, Y.; Hu, Y. Electron-enriched single-Pd-sites on g-C3N4 nanosheets achieved by in-situ anchoring twinned Pd nanoparticles for efficient CO2 photoreduction. *Advanced Powder Materials* **2024**, *3* (2). DOI: 10.1016/j.apmate.2024.100170.
173. Kim, B.; Kwon, D.; Baeg, J. O.; Austeria P, M.; Gu, G. H.; Lee, J. H.; Jeong, J.; Kim, W.; Choi, W. Dual-Atom-Site Sn-Cu/C3N4 Photocatalyst Selectively Produces Formaldehyde from CO2 Reduction. *Advanced Functional Materials* **2023**, *33* (19). DOI: 10.1002/adfm.202212453.
174. Li, X.; Zhang, J.; Wang, Z.; Fu, J.; Li, S.; Dai, K.; Liu, M. Interfacial C-S Bonds of g-CN/BiBrSS-Scheme Heterojunction for Enhanced Photocatalytic COReduction. *Chemistry* **2023**, *29* (4), e202202669. DOI: 10.1002/chem.202202669 From NLM PubMed-not-MEDLINE.
175. Tang, R.; Wang, H.; Dong, X.; Zhang, S.; Zhang, L.; Dong, F. A ball milling method for highly dispersed Ni atoms on g-C(3)Nto boost COphotoreduction. *J Colloid Interface Sci* **2023**, *630* (Pt B), 290–300. DOI: 10.1016/j.jcis.2022.10.110 From NLM PubMed-not-MEDLINE.
176. Miao, S.; Huang, M.; Chen, C.; Hu, W.; Wang, S.; Li, B. Photoinduced deposition of AuCu cocatalyst and polyaniline conducting layer on graphitic-C3N4 for enhanced CO2 photoreduction. *Colloids and Surfaces A: Physicochemical and Engineering Aspects* **2023**, *670*. DOI: 10.1016/j.colsurfa.2023.131584.
177. Chen, C.; Jin, J.; Chen, S.; Wang, T.; Xiao, J.; Peng, T. In-situ growth of ultrafine ZnO on g-C3N4 layer for highly active and selective CO2 photoreduction to CH4 under visible light. *Materials Research Bulletin* **2021**, *137*. DOI: 10.1016/j.materresbull.2020.111177.
178. Hu, K.; Li, Z.; Bai, L.; Yang, F.; Chu, X.; Bian, J.; Zhang, Z.; Xu, H.; Jing, L. Synergetic Subnano Ni- and Mn-Oxo Clusters Anchored by Chitosan Oligomers on 2D g-C3N4 Boost Photocatalytic CO2 Reduction. *Solar RRL* **2020**, *5* (6). DOI: 10.1002/solr.202000472.
179. Zhu, Z.; Chen, C. Y.; Wu, R. J. Hydrocarbon production by addition of Cu-ZnO on g-C3N4 for CO2 conversion. *Journal of the Chinese Chemical Society* **2020**, *67* (9), 1654–1660. DOI: 10.1002/jccs.202000173.
180. Jiang, L.; Wang, K.; Wu, X.; Zhang, G. Highly Enhanced Full Solar Spectrum-Driven Photocatalytic CO2 Reduction Performance in Cu2–xS/g-C3N4 Composite: Efficient Charge Transfer and Mechanism Insight. *Solar RRL* **2020**, *5* (2). DOI: 10.1002/solr.202000326.
181. Ma, X.; Hu, C.; Bian, Z. Hybrid photocatalytic systems comprising a manganese complex anchored on g-C3N4 for efficient visible-light photoreduction of CO2. *Inorganic Chemistry Communications* **2020**, *117*. DOI: 10.1016/j.inoche.2020.107951.
182. Wang, Y.; Qu, Y.; Qu, B.; Bai, L.; Liu, Y.; Yang, Z. D.; Zhang, W.; Jing, L.; Fu, H. Construction of Six-Oxygen-Coordinated Single Ni Sites on g-CNwith Boron-Oxo Species for Photocatalytic Water-Activation-Induced COReduction. *Adv Mater* **2021**, *33* (48), e2105482. DOI: 10.1002/adma.202105482 From NLM PubMed-not-MEDLINE.
183. Li, N.; Li, X.; Pan, R.; Cheng, M.; Guan, J.; Zhou, J.; Liu, M.; Tang, J.; Jing, D. Efficient Photocatalytic CO2 Reformation of Methane on Ru/La-g-C3N4 by Promoting Charge Transfer and CO2 Activation**. *ChemPhotoChem* **2021**, *5* (8), 748–757. DOI: 10.1002/cptc.202100020.
184. Qiu, S.; Shao, H.; He, C.; Song, X.; Fan, J.; Xue, Y.; Li, G.; Xiao, S. Tuning CO2 photoreduction: CoN/KPCN catalysts for High CH4 selectivity through an efficient microwave molten salt heating synthesis. *Applied Catalysis B: Environment and Energy* **2024**, *344*. DOI: 10.1016/j.apcatb.2023.123615.
185. Raza, A.; Haidry, A. A.; Yao, Z.; Saleem, M. F.; Alothman, A. A.; Mohammad, S. Synergistic effect of CuO and Sr doped g-C3N4 for CO2 photoreduction into hydrocarbon fuels. *Chemical Engineering Journal* **2024**, *480*. DOI: 10.1016/j.cej.2023.148162.
186. Tang, J.-y.; Pan, W.-g.; He, Y.-l.; Zhao, T.-s.; Wang, Q.-s.; Guo, R.-t. Function-oriented bifunctional Mg & MoP modified polymeric carbon nitride for selective photoreduction CO2 to CH4. *Chemical Engineering Journal* **2024**, *481*. DOI: 10.1016/j.cej.2023.148382.

 doi:10.20944/preprints202604.1590.v1

187. Heng, Q.; Wang, B.; Fan, X.; Chen, W.; Li, X.; Mao, L.; Shangguan, W. Enhanced photoreduction activity of CO2 to CO over Ag-loaded mesoporous g-C3N4 (MCN) by promoting charge separation and CO2 adsorption. *Journal of Alloys and Compounds* **2022**, *920*. DOI: 10.1016/j.jallcom.2022.165945.
188. Cheng, L.; Yin, H.; Cai, C.; Fan, J.; Xiang, Q. Single Ni Atoms Anchored on Porous Few-Layer g-CNfor Photocatalytic COReduction: The Role of Edge Confinement. *Small* **2020**, *16* (28), e2002411. DOI: 10.1002/smll.202002411 From NLM PubMed-not-MEDLINE.
189. Hu, S.; Qiao, P.; Liang, X.; Ba, G.; Zu, X.; Hu, H.; Ye, J.; Wang, D. Single-atom Pt–N4 active sites anchored on porous C3N4 nanosheet for boosting the photocatalytic CO2 reduction with nearly 100% CO selectivity. *Applied Catalysis B: Environment and Energy* **2024**, *346*. DOI: 10.1016/j.apcatb.2024.123737.
190. Adekoya, D.; Tahir, M.; Amin, N. A. S. Recent trends in photocatalytic materials for reduction of carbon dioxide to methanol. *Renewable and Sustainable Energy Reviews* **2019**, *116*. DOI: 10.1016/j.rser.2019.109389.
191. Foghani, M. H.; Tavakoli, O.; Parnian, M. J.; Zarghami, R. Enhanced visible light photocatalytic CO2 reduction over direct Z-scheme heterojunction Cu/P co-doped g-C3N4@TiO2 photocatalyst. *Chemical Papers* **2022**, *76* (6), 3459–3469. DOI: 10.1007/s11696-022-02109-z.
192. Nor, N. U. M.; Amin, N. A. S. Glucose precursor carbon-doped TiO2 heterojunctions for enhanced efficiency in photocatalytic reduction of carbon dioxide to methanol. *Journal of CO2 Utilization* **2019**, *33*, 372–383. DOI: 10.1016/j.jcou.2019.07.002.
193. Ban, C.; Wang, Y.; Ma, J.; Feng, Y.; Ding, J.; Duan, Y.; Liu, X.; Zhang, B.; Tang, J.; Tao, X.; et al. Constructing C-doped TiO2/β-Bi2O3 hybrids Z-scheme heterojunction for enhanced CO2 photoreduction. *Separation and Purification Technology* **2023**, *326*. DOI: 10.1016/j.seppur.2023.124745.
194. Bjelajac, A.; Kopač, D.; Fecant, A.; Tavernier, E.; Petrović, R.; Likozar, B.; Janaćković, D. Micro-kinetic modelling of photocatalytic CO2 reduction over undoped and N-doped TiO2. *Catalysis Science & Technology* **2020**, *10* (6), 1688–1698. DOI: 10.1039/c9cy02443c.
195. Zhang, N.; Li, J.; Sun, X.; Ma, J.; Li, S. One-pot synthesis of C/N co-doped TiO2 with rich oxygen vacancy for efficient photoreduction CO2-to-CO in pure water. *Journal of Environmental Chemical Engineering* **2024**, *12* (4). DOI: 10.1016/j.jece.2024.113212.
196. Wu, D.; Guo, J.; Wang, H.; Zhang, X.; Yang, Y.; Yang, C.; Gao, Z.; Wang, Z.; Jiang, K. Green synthesis of boron and nitrogen co-doped TiOwith rich B-N motifs as Lewis acid-base couples for the effective artificial COphotoreduction under simulated sunlight. *J Colloid Interface Sci* **2021**, *585*, 95–107. DOI: 10.1016/j.jcis.2020.11.075 From NLM PubMed-not-MEDLINE.
197. Wen, M.; Benabdesselam, M.; Beauger, C. CO2 photoreduction to methanol over Nb and N co-doped TiO2 aerogel deposited CuxO. *Journal of CO2 Utilization* **2024**, *81*. DOI: 10.1016/j.jcou.2024.102719.
198. Ahmadi, M.; Alavi, S. M.; Larimi, A. Effective CO2 photoreduction to methane over Bi2MoO6/ Ni, N co-doped TiO2 nano-photocatalyst. *International Journal of Hydrogen Energy* **2024**, *56*, 1309–1323. DOI: 10.1016/j.ijhydene.2023.12.291.
199. Huang, Y.; Li, K.; Zhou, J.; Guan, J.; Zhu, F.; Wang, K.; Liu, M.; Chen, W.; Li, N. Nitrogen-stabilized oxygen vacancies in TiO2 for site-selective loading of Pt and CoOx cocatalysts toward enhanced photoreduction of CO2 to CH4. *Chemical Engineering Journal* **2022**, *439*. DOI: 10.1016/j.cej.2022.135744.
200. Shi, W.; Zhang, R.; Wang, J.-C.; Li, W.; Guo, X.; Guo, J.; Li, R.; Hou, Y.; Zhang, W.; Gao, H.-L. One-pot hydrothermal preparation of Ni and I co-doped brookite-anatase TiO2 nanoparticles with remarkably enhanced photoreduction activity of CO2 to CH4. *Journal of Catalysis* **2024**, *429*. DOI: 10.1016/j.jcat.2023.115235.
201. Lee, D.-E.; Kim, D. J.; Moru, S.; Kim, M. G.; Jo, W.-K.; Tonda, S. Highly-configured TiO2 hollow spheres adorned with N-doped carbon dots as a high-performance photocatalyst for solar-induced CO2 reduction to methane. *Applied Surface Science* **2021**, *563*. DOI: 10.1016/j.apsusc.2021.150292.
202. Zhao, D.; Dang, C.; Xuan, Y.; Zhu, Q. Hydrophobic Ni@N-Doped TiO2 Nanosheet Arrays-Carbon Paper Photocatalyst for CO2 Photoreduction at Tri-Phase Interfaces. *Advanced Sustainable Systems* **2023**, *7* (4). DOI: 10.1002/adsu.202200450.
203. Kong, Y.; Pan, J.; Li, Y.; Zhang, Y.; Lin, W. Effect of hydrogen sources toward the CO2 photoreduction on boron decorated crystalline carbon nitride. *Applied Surface Science* **2024**, *669*. DOI: 10.1016/j.apsusc.2024.160426.

 doi:10.20944/preprints202604.1590.v1

204. Liu, Z.; Liang, J.; Song, Q.; Li, Y.; Zhang, Z.; Zhou, M.; Wei, W.; Xu, H.; Lee, C.-S.; Li, H.; et al. Construction atomic-level N-P charge transfer channel for boosted CO2 photoreduction. *Applied Catalysis B: Environmental* **2023**, *328*. DOI: 10.1016/j.apcatb.2023.122472.
205. Qaraah, F. A.; Mahyoub, S. A.; Drmosh, Q. A.; Qaraah, A.; Xin, F. One-step fabrication of unique 3D/2D S, O-doped g-C3N4 S-scheme isotype heterojunction for boosting CO2 photoreduction. *Materials Today Sustainability* **2023**, *23*. DOI: 10.1016/j.mtsust.2023.100437.
206. Hammoud, L.; Marchal, C.; Colbeau-Justin, C.; Toufaily, J.; Hamieh, T.; Caps, V.; Keller, V. Tuning CH4 Productivity from Visible Light-Driven Gas-Phase CO2 Photocatalytic Reduction on Doped g-C3N4/TiO2 Heterojunctions. *Energy Technology* **2023**, *11* (10). DOI: 10.1002/ente.202201363.
207. Hussien, M. K.; Sabbah, A.; Qorbani, M.; Putikam, R.; Kholimatussadiah, S.; Tzou, D. M.; Elsayed, M. H.; Lu, Y. J.; Wang, Y. Y.; Lee, X. H.; et al. Constructing B horizontal line N horizontal line P Bonds in Ultrathin Holey g-C(3)Nfor Regulating the Local Chemical Environment in Photocatalytic COReduction to CO. *Small* **2024**, *20* (35), e2400724. DOI: 10.1002/smll.202400724 From NLM Publisher.
208. Thamaraiselvan, C.; Wang, J.; James, D. K.; Narkhede, P.; Singh, S. P.; Jassby, D.; Tour, J. M.; Arnusch, C. J. Laser-induced graphene and carbon nanotubes as conductive carbon-based materials in environmental technology. *Materials Today* **2020**, *34*, 115–131. DOI: 10.1016/j.mattod.2019.08.014.
209. Ali, S.; Razzaq, A.; In, S.-I. Development of graphene based photocatalysts for CO2 reduction to C1 chemicals: A brief overview. *Catalysis Today* **2019**, *335*, 39–54. DOI: 10.1016/j.cattod.2018.12.003.
210. Wang, S.; Xu, M.; Peng, T.; Zhang, C.; Li, T.; Hussain, I.; Wang, J.; Tan, B. Porous hypercrosslinked polymer-TiO(2)-graphene composite photocatalysts for visible-light-driven COconversion. *Nat Commun* **2019**, *10* (1), 676. DOI: 10.1038/s41467-019-08651-x From NLM PubMed-not-MEDLINE.
211. Yang, Y.; Liu, M.; Han, S.; Xi, H.; Xu, C.; Yuan, R.; Long, J.; Li, Z. Double-sided modification of TiO2 spherical shell by graphene sheets with enhanced photocatalytic activity for CO2 reduction. *Applied Surface Science* **2021**, *537*. DOI: 10.1016/j.apsusc.2020.147991.
212. Olowoyo, J. O.; Kumar, M.; Singh, B.; Oninla, V. O.; Babalola, J. O.; Valdés, H.; Vorontsov, A. V.; Kumar, U. Self-assembled reduced graphene oxide-TiO2 nanocomposites: Synthesis, DFTB+ calculations, and enhanced photocatalytic reduction of CO2 to methanol. *Carbon* **2019**, *147*, 385–397. DOI: 10.1016/j.carbon.2019.03.019.
213. Khatun, F.; Aziz, A. A.; Sim, L. C. Preparation of Reduced Graphene Oxide (RGO) Modified Titanium Dioxide Nanotube (TNTs) as Visible Light Effective Catalyst for the Conversion of CO2 to CH4. *IOP Conference Series: Materials Science and Engineering* **2020**, *736* (4). DOI: 10.1088/1757-899x/736/4/042002.
214. Zhang, J.; Xu, J.; Tao, F. Interface Modification of TiO2 Nanotubes by Biomass-Derived Carbon Quantum Dots for Enhanced Photocatalytic Reduction of CO2. *ACS Applied Energy Materials* **2021**, *4* (11), 13120–13131. DOI: 10.1021/acsaem.1c02760.
215. Liu, S.; Jiang, T.; Fan, M.; Tan, G.; Cui, S.; Shen, X. Nanostructure rod-like TiO2-reduced graphene oxide composite aerogels for highly-efficient visible-light photocatalytic CO2 reduction. *Journal of Alloys and Compounds* **2021**, *861*. DOI: 10.1016/j.jallcom.2021.158598.
216. Yuan, B.; Qian, H.; Luo, Z.; Zhu, R.; Luan, W. A green synthetic approach for C/Ag@ urchin-like TiO2 nanocomposites showing a highly molar ratio CH4/CO for CO2 photoreduction. *Materials Letters* **2023**, *349*. DOI: 10.1016/j.matlet.2023.134758.
217. Morawski, A. W.; Ćmielewska, K.; Kusiak-Nejman, E.; Staciwa, P.; Kapica-Kozar, J.; Ekiert, E.; Pełech, I.; Narkiewicz, U. The influence of the addition of carbon spheres on photoactivity of TiO2 and ZnO in CO2 reduction process. *Journal of CO2 Utilization* **2023**, *75*. DOI: 10.1016/j.jcou.2023.102553.
218. Goutham, R.; Badri Narayan, R.; Srikanth, B.; Gopinath, K. P. Supporting Materials for Immobilisation of Nano-photocatalysts. In *Nanophotocatalysis and Environmental Applications*, Environmental Chemistry for a Sustainable World, 2019; pp 49–82.
219. Tasbihi, M.; Fresno, F.; Simon, U.; Villar-García, I. J.; Pérez-Dieste, V.; Escudero, C.; de la Peña O'Shea, V. A. On the selectivity of CO2 photoreduction towards CH4 using Pt/TiO2 catalysts supported on mesoporous silica. *Applied Catalysis B: Environmental* **2018**, *239*, 68–76. DOI: 10.1016/j.apcatb.2018.08.003.

 doi:10.20944/preprints202604.1590.v1

220. Ku, Y.; Lee, P.-C.; Luong, G. K. T. Photocatalytic reduction of gaseous carbon dioxide over NiO/TiO2 under UV light illumination. *Journal of the Taiwan Institute of Chemical Engineers* **2021**, *125*, 291–296. DOI: 10.1016/j.jtice.2021.06.036.
221. Lo, A.-Y.; Chung, Y.-C.; Koventhan, C.; Teng, I. J. Effect of the Ti content and pore size of mesoporous catalysts on CO2 photoreduction. *Journal of Photochemistry and Photobiology A: Chemistry* **2024**, *453*. DOI: 10.1016/j.jphotochem.2024.115631.
222. Zanardo, D.; Forghieri, G.; Tieuli, S.; Ghedini, E.; Menegazzo, F.; Di Michele, A.; Cruciani, G.; Signoretto, M. Effects of SiO2-based scaffolds in TiO2 photocatalyzed CO2 reduction. *Catalysis Today* **2022**, *387*, 54–60. DOI: 10.1016/j.cattod.2021.08.003.
223. Paulista, L. O.; Ferreira, A. F. P.; Rodrigues, A. E.; Martins, R. J. E.; Boaventura, R. A. R.; Vilar, V. J. P.; Silva, T. F. C. V. Solar thermo-photocatalytic methanation using a bifunctional RuO2:TiO2/Z13X photocatalyst/adsorbent material for efficient CO2 capture and conversion. *Journal of Environmental Chemical Engineering* **2024**, *12* (3). DOI: 10.1016/j.jece.2024.112418.
224. Rodríguez, V.; Camarillo, R.; Martínez, F.; Jiménez, C.; Rincón, J. High-pressure synthesis of rGO/TiO2 and rGO/TiO2/Cu catalysts for efficient CO2 reduction under solar light. *The Journal of Supercritical Fluids* **2021**, *174*. DOI: 10.1016/j.supflu.2021.105265.
225. Wei, Y.; Li, X.; Liu, Q.; Zhang, Y.; Zhang, K.; Huo, P.; Yan, Y. Leaf-Vein structure like g-C3N4/P-MWNTs donor-accepter hybrid catalyst for efficient CO2 photoreduction. *Carbon* **2022**, *188*, 59–69. DOI: 10.1016/j.carbon.2021.11.053.
226. Gu, H.; Liang, F.; Wang, X.; Wu, S.; Lv, G.; Zhang, H.; Zhang, S.; Lu, L.; Dong, Z. N-doped rutile TiO2 nanorod@g-C3N4 core/shell S-scheme heterojunctions for boosting CO2 photoreduction activity. *Catalysis Science & Technology* **2023**, *13* (3), 898–909. DOI: 10.1039/d2cy01839j.
227. Li, X.; Sun, B.; Wu, Q.; Fan, H.; Liu, X.; Cao, J.; Yang, L.; Liu, H.; Wei, M. 2D–1D-2D multi-interfacial-electron transfer scheme enhanced g-C3N4/MWNTs/rGO hybrid composite for accelerating CO2 photoreduction. *Journal of Alloys and Compounds* **2023**, *940*. DOI: 10.1016/j.jallcom.2023.168796.
228. Jo, M.; Choi, S.; Jo, J. H.; Kim, S. Y.; Kim, P. S.; Kim, C. H.; Son, H. J.; Pac, C.; Kang, S. O. Utility of Squaraine Dyes for Dye-Sensitized Photocatalysis on Water or Carbon Dioxide Reduction. *ACS Omega* **2019**, *4* (10), 14272–14283. DOI: 10.1021/acsomega.9b01914 From NLM PubMed-not-MEDLINE.
229. Rao, H.; Lim, C. H.; Bonin, J.; Miyake, G. M.; Robert, M. Visible-Light-Driven Conversion of COto CHwith an Organic Sensitizer and an Iron Porphyrin Catalyst. *J Am Chem Soc* **2018**, *140* (51), 17830–17834. DOI: 10.1021/jacs.8b09740 From NLM PubMed-not-MEDLINE.
230. Chen, Q.; Wang, H.; Wang, C.; Guan, R.; Duan, R.; Fang, Y.; Hu, X. Activation of molecular oxygen in selectively photocatalytic organic conversion upon defective TiO2 nanosheets with boosted separation of charge carriers. *Applied Catalysis B: Environmental* **2020**, *262*. DOI: 10.1016/j.apcatb.2019.118258.
231. Seeharaj, P.; Kongmun, P.; Paiplod, P.; Prakobmit, S.; Sriwong, C.; Kim-Lohsoontorn, P.; Vittayakorn, N. Ultrasonically-assisted surface modified TiO(2)/rGO/CeOheterojunction photocatalysts for conversion of COto methanol and ethanol. *Ultrason Sonochem* **2019**, *58*, 104657. DOI: 10.1016/j.ultsonch.2019.104657 From NLM PubMed-not-MEDLINE.
232. Ge, Y.; Zhang, C.; Yu, Z.; Wang, D. ZnIn2S4/TiO2 photocatalyst for CO2 photoreduction: Advancing sustainable energy conversion to renewable solar fuels. *Journal of Industrial and Engineering Chemistry* **2024**, *132*, 335–345. DOI: 10.1016/j.jiec.2023.11.027.
233. Xie, K. L.; Liao, Y. Q.; Hu, J. J.; Lu, K. Q.; Wen, H. R. Rationally Designed S-Scheme CeO(2)/g-C(3)NHeterojunction for Promoting Visible Light Driven COPhotoreduction into Syngas. *ChemSusChem* **2024**, *17* (23), e202400969. DOI: 10.1002/cssc.202400969 From NLM PubMed-not-MEDLINE.
234. Tang, Z.; Wang, C.; He, W.; Wei, Y.; Zhao, Z.; Liu, J. The Z-scheme g-C3N4/3DOM-WO3 photocatalysts with enhanced activity for CO2 photoreduction into CO. *Chinese Chemical Letters* **2022**, *33* (2), 939–942. DOI: 10.1016/j.cclet.2021.07.020.
235. Li, X.; Guan, J.; Jiang, H.; Song, X.; Huo, P.; Wang, H. rGO modified R-CeO2/g-C3N4 multi-interface contact S-scheme photocatalyst for efficient CO2 photoreduction. *Applied Surface Science* **2021**, *563*. DOI: 10.1016/j.apsusc.2021.150042.

 doi:10.20944/preprints202604.1590.v1

236. Bafaqeer, A.; Tahir, M.; Amin, N. A. S.; Ummer, A. C.; Thabit, H. A.; Dhamodharan, D.; Ahmed, S.; Kumar, N. Performance analysis of rGO-bridged g-C3N4/ZnV2O6 S-scheme heterojunction for CO2 photoreduction with H2O in an externally reflected photoreactor. *Journal of Alloys and Compounds* **2023**, *968*. DOI: 10.1016/j.jallcom.2023.171833.
237. Wang, L.; Qiu, J.; Wu, N.; Yu, X.; An, X. TiO(2)/CsPbBrS-scheme heterojunctions with highly improved COphotoreduction activity through facet-induced Fermi level modulation. *J Colloid Interface Sci* **2023**, *629* (Pt A), 206–214. DOI: 10.1016/j.jcis.2022.08.120 From NLM PubMed-not-MEDLINE.
238. Gao, Y.; Sun, L.; Bian, J.; Zhang, Z.; Li, Z.; Jing, L. Accelerated charge transfer of g-C3N4/BiVO4 Z-scheme 2D heterojunctions by controllably introducing phosphate bridges and Ag nanocluster co-catalysts for selective CO2 photoreduction to CO. *Applied Surface Science* **2023**, *610*. DOI: 10.1016/j.apsusc.2022.155360.
239. Wang, H.; Li, H.; Chen, Z.; Li, J.; Li, X.; Huo, P.; Wang, Q. TiO2 modified g-C3N4 with enhanced photocatalytic CO2 reduction performance. *Solid State Sciences* **2020**, *100*. DOI: 10.1016/j.solidstatesciences.2019.106099.
240. Zhang, F.; Li, Y.-H.; Qi, M.-Y.; Yamada, Y. M. A.; Anpo, M.; Tang, Z.-R.; Xu, Y.-J. Photothermal catalytic CO2 reduction over nanomaterials. *Chem Catalysis* **2021**, *1* (2), 272–297. DOI: 10.1016/j.checat.2021.01.003.
241. Banitalebi Dehkordi, A.; Ziarati, A.; Ghasemi, J. B.; Badiei, A. Preparation of hierarchical g-C3N4@TiO2 hollow spheres for enhanced visible-light induced catalytic CO2 reduction. *Solar Energy* **2020**, *205*, 465–473. DOI: 10.1016/j.solener.2020.05.071.
242. Li, Z.; Xiong, J.; Huang, Y.; Huang, Y.; Waterhouse, G. I. N.; Wang, Z.; Mao, Y.; Liang, Z.; Luo, X. Synergy mechanism of confined effect and Z-scheme electron transfer in core–shell structure photocatalyst for boosting photoreduction CO2 activity. *Chemical Engineering Journal* **2024**, *486*. DOI: 10.1016/j.cej.2024.150304.
243. Tahir, M.; Tahir, B.; Kumar, N.; Al Marzooqi, M.; Siraj, M.; Fatehmulla, A. In-situ synthesis of V2AlC@V2O5/TiO2 immobilized over honeycomb support with vanadium oxide electron transfer mediator for stimulating selective CO2 photoreduction through bi-reforming in a monolith reactor. *Fuel* **2024**, *370*. DOI: 10.1016/j.fuel.2024.131816.
244. Jiao, Y.; Chen, Y.; Han, W.; Liang, S.; Li, W.; Tian, G. Multi-channel charge transfer of hierarchical TiOnanosheets encapsulated MIL-125(Ti) hollow nanodisks sensitized by ZnSe for efficient COphotoreduction. *J Colloid Interface Sci* **2022**, *627*, 492–502. DOI: 10.1016/j.jcis.2022.07.038 From NLM PubMed-not-MEDLINE.
245. Kumar, D. P.; Do, K. H.; Rangappa, A. P.; Lee, J.; Wang, J.; Boppella, R.; Gopannagari, M.; Reddy, K. A. J.; Reddy, D. A.; Kim, T. K. Highly stable and durable ZnIn(2)Snanosheets wrapped oxygen deficient blue TiO(2)(B) catalyst for selective COphotoreduction into CO and CH(4). *J Colloid Interface Sci* **2023**, *651*, 264–272. DOI: 10.1016/j.jcis.2023.07.197 From NLM PubMed-not-MEDLINE.
246. Collado, L.; Gomez-Mendoza, M.; García-Tecedor, M.; Oropeza, F. E.; Reynal, A.; Durrant, J. R.; Serrano, D. P.; de la Peña O'Shea, V. A. Towards the improvement of methane production in CO2 photoreduction using Bi2WO6/TiO2 heterostructures. *Applied Catalysis B: Environmental* **2023**, *324*. DOI: 10.1016/j.apcatb.2022.122206.
247. Ruan, C.; Wang, C.; Chen, Y.; Wang, Z.; Wang, K.; Zhou, Y.; Zhang, S.; Chen, G.; Zheng, X.; Meng, S.; et al. Hollow heterojunction with dual-vacancy engineering to boost photocatalytic performance for photoreduction of CO2 coupled with selective oxidation of benzyl alcohol to benzaldehyde. *Separation and Purification Technology* **2024**, *351*. DOI: 10.1016/j.seppur.2024.127929.
248. Song, X.; Wang, X.; Dong, W.; Qu, Q.; Wang, H.; Yang, F. Solar light-responsive Ag/CdS/TNTs (TiO2 nanotubes) photocatalysts for enhanced CO2 photoreduction and hydrogen evolution. *Inorganic Chemistry Communications* **2022**, *146*. DOI: 10.1016/j.inoche.2022.110228.
249. Raza, A.; Shen, H.; Haidry, A. A.; Shahzad, M. K.; Sun, L. Facile in-situ fabrication of TiO2-Cu2ZnSnS4 hybrid nanocomposites and their photoreduction of CO2 to CO/CH4 generation. *Applied Surface Science* **2020**, *529*. DOI: 10.1016/j.apsusc.2020.147005.
250. Khan, H.; Pawar, R. C.; Charles, H.; Sunyong Lee, C. Cu-doped TiO2 nanofibers coated with 1T MoSe2 nanosheets providing a conductive pathway for the electron separation in CO2 photoreduction. *Applied Surface Science* **2023**, *636*. DOI: 10.1016/j.apsusc.2023.157832.

 doi:10.20944/preprints202604.1590.v1

251. Jin, J.; Chen, S.; Wang, J.; Chen, C.; Peng, T. One-pot hydrothermal preparation of PbO-decorated brookite/anatase TiO2 composites with remarkably enhanced CO2 photoreduction activity. *Applied Catalysis B: Environmental* **2020**, *263*. DOI: 10.1016/j.apcatb.2019.118353.
252. Cheng, S.; Sun, Z.; Lim, K. H.; Liu, K.; Wibowo, A. A.; Du, T.; Liu, L.; Nguyen, H. T.; Li, G. K.; Yin, Z.; et al. Defective heterojunctions in CO2 photoreduction: Enabling ultrafast interfacial charge transfer and selective methanation. *Applied Catalysis B: Environmental* **2024**, *343*. DOI: 10.1016/j.apcatb.2023.123583.
253. Pan, J.; Xiao, G.; Niu, J.; Fu, Y.; Cao, J.; Wang, J.; Zheng, Y.; Zhu, M.; Li, C. The photocatalytic hydrogen evolution and photoreduction CO2 selective enhancement of Co3O4/Ti3+-TiO2/NiO hollow core-shell dual pn junction. *Journal of Cleaner Production* **2022**, *380*. DOI: 10.1016/j.jclepro.2022.135037.
254. Ru, Y.; Chen, Y.; Yu, X.; Zhang, Q.; Yin, Y.; Tian, G. Enhanced charge separation of Cu-BTC@CuSe@TiO2 hollow octahedrons for efficient CO2 photoreduction with superior CO selectivity. *Separation and Purification Technology* **2024**, *349*. DOI: 10.1016/j.seppur.2024.127784.
255. Bi, W.; Zhang, L.; Jiang, H.; Li, C.; Hu, Y. Construction of CuInS2/C/TiO2 hierarchical tandem heterostructures with optimized CO2 photoreduction under visible light. *Chemical Engineering Journal* **2022**, *433*. DOI: 10.1016/j.cej.2021.133679.
256. Dong, Z.; Zhang, Z.; Jiang, Y.; Chu, Y.; Xu, J. Embedding CsPbBr3 perovskite quantum dots into mesoporous TiO2 beads as an S-scheme heterojunction for CO2 photoreduction. *Chemical Engineering Journal* **2022**, *433*. DOI: 10.1016/j.cej.2021.133762.
257. An, X.; Bian, J.; Zhu, K.; Liu, R.; Liu, H.; Qu, J. Facet-dependent activity of TiO2/covalent organic framework S-scheme heterostructures for CO2 photoreduction. *Chemical Engineering Journal* **2022**, *442*. DOI: 10.1016/j.cej.2022.135279.
258. Wang, J.; Yu, Y.; Cui, J.; Li, X.; Zhang, Y.; Wang, C.; Yu, X.; Ye, J. Defective g-C3N4/covalent organic framework van der Waals heterojunction toward highly efficient S-scheme CO2 photoreduction. *Applied Catalysis B: Environmental* **2022**, *301*. DOI: 10.1016/j.apcatb.2021.120814.
259. Firoozabadi, S. R.; Khosravi-Nikou, M. R.; Shariati, A. CO2 photoreduction using TiO2 nanoflower /UiO-66 composite under UV light irradiation. *Journal of Environmental Chemical Engineering* **2023**, *11* (5). DOI: 10.1016/j.jece.2023.110978.
260. Das, R.; Das, K.; Churipard, S. R.; Peter, S. C. Activating oxygen deficient TiOin the visible region by Bi(2)MoOfor COphotoreduction to methanol. *Chem Commun (Camb)* **2022**, *58* (46), 6638–6641. DOI: 10.1039/d2cc00490a From NLM PubMed-not-MEDLINE.
261. Zeng, S.; Vahidzadeh, E.; VanEssen, C. G.; Kar, P.; Kisslinger, R.; Goswami, A.; Zhang, Y.; Mahdi, N.; Riddell, S.; Kobryn, A. E.; et al. Optical control of selectivity of high rate CO2 photoreduction via interband- or hot electron Z-scheme reaction pathways in Au-TiO2 plasmonic photonic crystal photocatalyst. *Applied Catalysis B: Environmental* **2020**, *267*. DOI: 10.1016/j.apcatb.2020.118644.
262. Yang, J.; Wang, J.; Zhao, W.; Wang, G.; Wang, K.; Wu, X.; Li, J. 0D/1D Cu2-S/TiO2 S-scheme heterojunction with enhanced photocatalytic CO2 reduction performance via surface plasmon resonance induced photothermal effects. *Applied Surface Science* **2023**, *613*. DOI: 10.1016/j.apsusc.2022.156083.
263. Ahmadi, M.; Alavi, S. M.; Larimi, A. UV–vis light responsive Bi2WO6 nanosheet/TiO2 nanobelt heterojunction photo-catalyst for CO2 reduction. *Catalysis Communications* **2023**, *179*. DOI: 10.1016/j.catcom.2023.106681.
264. Wang, Y.; Zhang, C.; Zeng, Y.; Cai, W.; Wan, S.; Li, Z.; Zhang, S.; Zhong, Q. Ag and MOFs-derived hollow Co(3)Odecorated in the 3D g-C(3)Nfor creating dual transferring channels of electrons and holes to boost COphotoreduction performance. *J Colloid Interface Sci* **2022**, *609*, 901–909. DOI: 10.1016/j.jcis.2021.11.153 From NLM PubMed-not-MEDLINE.
265. Liu, W.; Wang, Q.; Liu, Z.; Ding, G. Bridging between NiAl-LDH and g-C(3)Nby using carbon quantum dots for highly enhanced photoreduction of COinto CO. *J Colloid Interface Sci* **2022**, *622*, 21–30. DOI: 10.1016/j.jcis.2022.04.102 From NLM PubMed-not-MEDLINE.
266. Zhou, J.; Gao, B.; Wu, D.; Tian, C.; Ran, H.; Chen, W.; Huang, Q.; Zhang, W.; Qi, F.; Zhang, N.; et al. Enhanced Photocatalytic Activity of Lead-Free Cs2TeBr6/g-C3N4 Heterojunction Photocatalyst and Its Mechanism. *Advanced Functional Materials* **2023**, *34* (3). DOI: 10.1002/adfm.202308411.

 doi:10.20944/preprints202604.1590.v1

267. Xu, Y.; Hou, W.; Huang, K.; Guo, H.; Wang, Z.; Lian, C.; Zhang, J.; Wu, D.; Lei, Z.; Liu, Z.; et al. Engineering Built-In Electric Field Microenvironment of CQDs/g-C(3)NHeterojunction for Efficient Photocatalytic COReduction. *Adv Sci (Weinh)* **2024**, *11* (28), e2403607. DOI: 10.1002/advs.202403607 From NLM PubMed-not-MEDLINE.
268. Sayed, M.; Zhu, B.; Kuang, P.; Liu, X.; Cheng, B.; Ghamdi, A. A. A.; Wageh, S.; Zhang, L.; Yu, J. EPR Investigation on Electron Transfer of 2D/3D g-C3N4/ZnO S-Scheme Heterojunction for Enhanced CO2 Photoreduction. *Advanced Sustainable Systems* **2021**, *6* (1). DOI: 10.1002/adsu.202100264.
269. Liu, C.; Zhang, Y.; Li, X.; Wang, W.; Huang, H.; Gao, C.; Xu, S.; Hu, W.; Zhang, Y. Facet Coupling Design for Bi4TaO8Cl/g-C3N4 via Electrostatic Self-Assembly to Enhance Photocatalytic Activity. *ChemPhotoChem* **2021**, *6* (2). DOI: 10.1002/cptc.202100184.
270. Pollak, N.; Huang, P.; Bell, H.; Li, G.; Caputo, C. A. Tunable Photocatalytic Production of Syngas Using Co@C3N4 and Black Phosphorus. *ChemPhotoChem* **2021**, *5* (7), 674–679. DOI: 10.1002/cptc.202100054.
271. Fang, R.; Yang, Z.; Guo, M.; Wang, Z.; Qiu, J.; Ran, J.; Xue, C. g-C3N4@CPP/BiOClBr-OV biomimetic fractal heterojunction synergistically enhance carrier dynamics for boosted CO2 photoreduction activity. *Applied Surface Science* **2024**, *656*. DOI: 10.1016/j.apsusc.2024.159712.
272. Wang, Z. L.; Liu, R. L.; Zhang, J. F.; Dai, K. S-scheme Porous g-C N/A MoO Heterojunction Composite for CO Photoreduction. *Chinese Journal of Structural Chemistry* **2022**, *41* (6), 2206015–2206022. DOI: 10.14102/j.cnki.0254-5861.2022-0108.
273. Ma, W.; Zhu, Y.; Wang, X. Au nanoparticles modified HNTs/g-C3N4/CdS composite for highly efficient CO2 photoreduction and tetracycline degradation. *Journal of Alloys and Compounds* **2023**, *935*. DOI: 10.1016/j.jallcom.2022.168129.
274. Li, L.; Ma, D.; Xu, Q.; Huang, S. Constructing hierarchical ZnIn2S4/g-C3N4 S-scheme heterojunction for boosted CO2 photoreduction performance. *Chemical Engineering Journal* **2022**, *437*. DOI: 10.1016/j.cej.2022.135153.
275. Li, Y.; Yin, Q.; Zeng, Y.; Liu, Z. Hollow spherical biomass derived-carbon dotted with SnS2/g-C3N4 Z-scheme heterojunction for efficient CO2 photoreduction into CO. *Chemical Engineering Journal* **2022**, *438*. DOI: 10.1016/j.cej.2022.135652.
276. Li, J.; He, C.; Xu, N.; Wu, K.; Huang, Z.; Zhao, X.; Nan, J.; Xiao, X. Interfacial bonding of hydroxyl-modified g-C3N4 and Bi2O2CO3 toward boosted CO2 photoreduction: Insights into the key role of OH groups. *Chemical Engineering Journal* **2023**, *452*. DOI: 10.1016/j.cej.2022.139191.
277. Kong, X.; Fan, J.; Feng, B.; Li, J.; Yang, G.; Xue, C. Carbon dots-triggered the fabrication of miniature g-C3N4/CDs/WO3 S-scheme heterojunction for efficient CO2 photoreduction. *Chemical Engineering Journal* **2023**, *476*. DOI: 10.1016/j.cej.2023.146774.
278. Wang, K.; Feng, X.; Shangguan, Y.; Wu, X.; Chen, H. Selective CO2 photoreduction to CH4 mediated by dimension-matched 2D/2D Bi3NbO7/g-C3N4 S-scheme heterojunction. *Chinese Journal of Catalysis* **2022**, *43* (2), 246–254. DOI: 10.1016/s1872-2067(21)63819-6.
279. Wang, Y.; Ban, C.; Feng, Y.; Ma, J.; Ding, J.; Wang, X.; Ruan, L.; Duan, Y.; Brik, M. G.; Gan, L.; et al. Unveiling the synergistic role of nitrogen vacancies and Z-scheme heterojunction in g-C3N4/β-Bi2O3 hybrids for enhanced CO2 photoreduction. *Nano Energy* **2024**, *124*. DOI: 10.1016/j.nanoen.2024.109494.
280. Alshamkhani, M. T.; Putri, L. K.; Lahijani, P.; Lee, K. T.; Mohamed, A. R. A metal-free electrochemically exfoliated graphene/graphitic carbon nitride nanocomposite for CO2 photoreduction to methane under visible light irradiation. *Journal of Environmental Chemical Engineering* **2023**, *11* (1). DOI: 10.1016/j.jece.2022.109086.
281. Charles, H.; Chengula, P. J.; Pawar, R. C.; Khan, H.; Kim, S.; Lee, C. S. Synergistic effect of surface modification and effective interfacial charge transfer over faceted g-C3N4/ZnSe heterojunction to enhance CO2 photoreduction activity. *Journal of Water Process Engineering* **2023**, *56*. DOI: 10.1016/j.jwpe.2023.104307.
282. Chen, X.; Pan, W. G.; Hong, L. F.; Hu, X.; Wang, J.; Bi, Z. X.; Guo, R. T. TiC-modified g-CN/MoSeS-Scheme Heterojunction with Full-Spectrum Response for COPhotoreduction to CO and CH(4). *ChemSusChem* **2023**, *16* (15), e202300179. DOI: 10.1002/cssc.202300179 From NLM PubMed-not-MEDLINE.

283. Shi, Q.; Huang, J.; Yang, Y.; Wu, J.; Shen, J.; Liu, X.; Sun, A.; Liu, Z. In-situ construction of urchin-like hierarchical g-C3N4/NiAl-LDH hybrid for efficient photoreduction of CO2. *Materials Letters* **2020**, *268*. DOI: 10.1016/j.matlet.2020.127560.
284. Song, Q.; Hu, J.; Zhou, Y.; Ye, Q.; Shi, X.; Li, D.; Jiang, D. Carbon vacancy-mediated exciton dissociation in Ti(3)C(2)T(x)/g-C(3)NSchottky junctions for efficient photoreduction of CO(2). *J Colloid Interface Sci* **2022**, *623*, 487–499. DOI: 10.1016/j.jcis.2022.05.064 From NLM PubMed-not-MEDLINE.
285. Guo, H.; Ding, J.; Wan, S.; Wang, Y.; Zhong, Q. Highly efficient CH3OH production over Zn0.2Cd0.8S decorated g-C3N4 heterostructures for the photoreduction of CO2. *Applied Surface Science* **2020**, *528*. DOI: 10.1016/j.apsusc.2020.146943.
286. Wang, K.; Peng, L.; Shao, X.; Cheng, Q.; Wang, J.; Li, K.; Wang, H. Nb–O–C Charge Transfer Bridge in 2D/2D Nb2O5/g-C3N4 S-Scheme Heterojunction for Boosting Solar-Driven CO2 Reduction: In Situ Illuminated X-Ray Photoelectron Spectroscopy Investigation and Mechanism Insight. *Solar RRL* **2022**, *6* (9). DOI: 10.1002/solr.202200434.
287. Zhao, X.; Li, J.; Kong, X.; Li, C.; Lin, B.; Dong, F.; Yang, G.; Shao, G.; Xue, C. Carbon Dots Mediated In Situ Confined Growth of Bi Clusters on g-CNNanomeshes for Boosting Plasma-Assisted Photoreduction of CO(2). *Small* **2022**, *18* (46), e2204154. DOI: 10.1002/smll.202204154 From NLM PubMed-not-MEDLINE.
288. He, W.; Wei, Y.; Xiong, J.; Tang, Z.; Wang, Y.; Wang, X.; Xu, H.; Zhang, X.; Yu, X.; Zhao, Z.; et al. Variable valence Mo5+/Mo6+ ionic bridge in hollow spherical g-C3N4/Bi2MoO6 catalysts for promoting selective visible light-driven CO2 photoreduction into CO. *Journal of Energy Chemistry* **2023**, *80*, 361–372. DOI: 10.1016/j.jechem.2023.01.028.
289. Nguyen, T. B.; Dinh Thi, T. H.; Pham Minh, D.; Bui Minh, H.; Nguyen Thi, N. Q.; Nguyen Dinh, B. Photoreduction of COto CHover Efficient Z-Scheme gamma-Fe(2)O(3)/g-C(3)NComposites. *J Anal Methods Chem* **2022**, *2022*, 1358437. DOI: 10.1155/2022/1358437 From NLM PubMed-not-MEDLINE.
290. Chen, Q.; Lan, X.; Ma, Y.; Lu, P.; Yuan, Z.; Shi, J. Boosting CsPbBr3-Driven Superior and Long-Term Photocatalytic CO2 Reduction under Pure Water Medium: Synergy Effects of Multifunctional Melamine Foam and Graphitic Carbon Nitride (g-C3N4). *Solar RRL* **2021**, *5* (7). DOI: 10.1002/solr.202100186.
291. Xu, M.; Zhao, X.; Jiang, H.; Chen, S.; Huo, P. MOFs-derived C-In2O3/g-C3N4 heterojunction for enhanced photoreduction CO2. *Journal of Environmental Chemical Engineering* **2021**, *9* (6). DOI: 10.1016/j.jece.2021.106469.
292. Zhu, X.; Deng, H.; Cheng, G. Facile construction of g-C3N4-W18O49 heterojunction with improved charge transfer for solar-driven CO2 photoreduction. *Inorganic Chemistry Communications* **2021**, *132*. DOI: 10.1016/j.inoche.2021.108814.
293. Xu, Y.; Jin, X.; Ge, T.; Xie, H.; Sun, R.; Su, F.; Li, X.; Ye, L. Realizing efficient CO2 photoreduction in Bi3O4Cl: Constructing van der Waals heterostructure with g-C3N4. *Chemical Engineering Journal* **2021**, *409*. DOI: 10.1016/j.cej.2020.128178.
294. Cai, J.; Wang, H.; Li, H.; Li, K. High-performance photocatalytic reduction of CO2 to CO by defective g-C3N4/CeO2 under sacrificial agent-free conditions. *Journal of Rare Earths* **2025**, *43* (9), 1882–1891. DOI: 10.1016/j.jre.2024.07.031.